Research Article
NAFLD and Alcohol-Related Liver Diseases

JOURNAL
OF HEPATOLOGY

Intestinal B cells license metabolic T-cell activation in NASH microbiota/antigen-independently and contribute to fibrosis by IgA-FcR signalling

Elena Kotsiliti[1,†], **Valentina Leone**[1,2,3,43,†], Svenja Schuehle[1,41,#], Olivier Govaere[4,#], Hai Li[5], Monika J. Wolf[31,§], Helena Horvatic[6], Sandra Bierwirth[7,8], Jana Hundertmark[9], Donato Inverso[10,11], Laimdota Zizmare[12], Avital Sarusi-Portuguez[13], Revant Gupta[14,15], Tracy O'Connor[1,42], Anastasios D. Giannou[16,17], Ahmad Mustafa Shiri[16], Yehuda Schlesinger[13], Maria Garcia Beccaria[1], Charlotte Rennert[17], Dominik Pfister[1], Rupert Öllinger[3], Iana Gadjalova[18], Pierluigi Ramadori[1], Mohammad Rahbari[1], Nuh Rahbari[19], Marc E. Healy[21], Mirian Fernández-Vaquero[1], Neda Yahoo[1], Jakob Janzen[1], Indrabahadur Singh[1,39], Chaofan Fan[1], Xinyuan Liu[20,21], Monika Rau[22], Martin Feuchtenberger[23], Eva Schwaneck[24], Sebastian J. Wallace[25], Simon Cockell[40], John Wilson-Kanamori[25], Prakash Ramachandran[25], Celia Kho[6], Timothy J. Kendall[25,26], Anne-Laure Leblond[31], Selina J. Keppler[18], Piotr Bielecki[27], Katja Steiger[28,29], Maike Hofmann[14], Karsten Rippe[30], Horst Zitzelsberger[2], Achim Weber[31], Nisar Malek[32], Tom Luedde[33], Mihael Vucur[33], Hellmut G. Augustin[10,11], Richard Flavell[27], Oren Parnas[11], Roland Rad[3,18], Olivier Pabst[34], Neil C. Henderson[25,26], Samuel Huber[16], Andrew Macpherson[5], Percy Knolle[35], Manfred Claassen[14,15,32], Andreas Geier[22], Christoph Trautwein[12], Kristian Unger[2], Eran Elinav[36,37], Ari Waisman[20,21], Zeinab Abdullah[6], Dirk Haller[7,8], Frank Tacke[9], Quentin M. Anstee[4,38], Mathias Heikenwalder[1,44,*]

Journal of Hepatology **2023**. vol. 79 | 296–313

Background & Aims: The progression of non-alcoholic steatohepatitis (NASH) to fibrosis and hepatocellular carcinoma (HCC) is aggravated by auto-aggressive T cells. The gut-liver axis contributes to NASH, but the mechanisms involved and the consequences for NASH-induced fibrosis and liver cancer remain unknown. We investigated the role of gastrointestinal B cells in the development of NASH, fibrosis and NASH-induced HCC.

Methods: C57BL/6J wild-type (WT), B cell-deficient and different immunoglobulin-deficient or transgenic mice were fed distinct NASH-inducing diets or standard chow for 6 or 12 months, whereafter NASH, fibrosis, and NASH-induced HCC were assessed and analysed. Specific pathogen-free/germ-free WT and μMT mice (containing B cells only in the gastrointestinal tract) were fed a choline-deficient high-fat diet, and treated with an anti-CD20 antibody, whereafter NASH and fibrosis were assessed. Tissue biopsy samples from patients with simple steatosis, NASH and cirrhosis were analysed to correlate the secretion of immunoglobulins to clinicopathological features. Flow cytometry, immunohistochemistry and single-cell RNA-sequencing analysis were performed in liver and gastrointestinal tissue to characterise immune cells in mice and humans.

Results: Activated intestinal B cells were increased in mouse and human NASH samples and licensed metabolic T-cell activation to induce NASH independently of antigen specificity and gut microbiota. Genetic or therapeutic depletion of systemic or gastrointestinal B cells prevented or reverted NASH and liver fibrosis. IgA secretion was necessary for fibrosis induction by activating CD11b+CCR2+F4/80+CD11c-FCGR1+ hepatic myeloid cells through an IgA-FcR signalling axis. Similarly, patients with NASH had increased numbers of activated intestinal B cells; additionally, we observed a positive correlation between IgA levels and activated FcRg+ hepatic myeloid cells, as well the extent of liver fibrosis.

Conclusions: Intestinal B cells and the IgA-FcR signalling axis represent potential therapeutic targets for the treatment of NASH.

Keywords: NAFLD; NAFL; NASH; HCC; fibrosis; B cells; gut-liver axis.
Received 2 February 2023; received in revised form 5 April 2023; accepted 11 April 2023; available online 22 May 2023
* Corresponding author. Address: Department Chronic Inflammation and Cancer, German Cancer Research Center (DKFZ), Im Neuenheimer Feld 242, Heidelberg, 69120, Germany; Tel.: +49 6221 42-3890.
E-mail addresses: m.heikenwaelder@dkfz.de, Mathias.Heikenwaelder@med.uni-tuebingen.de (M. Heikenwalder).
§ Current address: Roche Pharmaceutical Research and Early Development Oncology, Roche Innovation Center Munich, Penzberg, Germany
† These authors contributed equally: Elena Kotsiliti & Valentina Leone
# These authors contributed equally: Svenja Schuehle & Olivier Govaere
https://doi.org/10.1016/j.jhep.2023.04.037

Introduction

The worldwide increase in obesity is driving an epidemic of non-alcoholic fatty liver disease (NAFLD), a progressive disease strongly associated with metabolic syndrome and characterised by excessive hepatic lipid accumulation, hepatocyte damage, and aberrant metabolism.[1,2] NAFLD is subdivided into simple steatosis and non-alcoholic steatohepatitis (NASH), an inflammatory, auto-aggressive[3,4] disease aggravated by T cells causing necro-inflammation.[5] Fibrosis, which can develop concomitantly with NASH, may progress to cirrhosis, increasing the risk of liver failure or liver cancer, the latter being the third most common cause of cancer-related death worldwide.[6] Hepatocellular carcinoma (HCC), the most frequent form of primary liver cancer,[7] is highly linked to the pathological background of NAFLD.[2] Fibrosis is a critical factor for predicting disease outcome as it correlates with the increased risk of HCC mortality in patients with NASH[8,9]. It has also been reported that in a subset of patients, NASH-driven HCC occurs in the absence of severe fibrosis/cirrhosis.[2,10] Consequently, there is a considerable healthcare cost burden owing to NASH, including HCC surveillance.[11–13]

The gut-liver axis is a critical component in NAFLD pathogenesis.[14] Animal studies have demonstrated a direct role of altered intestinal microbiota in steatosis,[15] NASH(16), fibrosis[17] and liver cancer.[18] In addition, sterile inflammation, mediated by damage-associated molecular patterns and metabolite-associated molecular patterns,[19,20] is considered an important driver of liver injury in NASH. Moreover, macrophages play a crucial role in liver injury and fibrosis in NASH, with monocyte-derived macrophages (MoMFs) exhibiting a proinflammatory phenotype that can directly activate hepatic stellate cells.[21]

Serum IgA, secreted by plasma cells in secondary lymphoid organs, has been shown to be elevated in patients with NAFLD,[22,23] and was an independent predictor of advanced fibrosis.[22] Chronic inflammation and fibrosis in humans and mice with NAFLD were accompanied by liver-resident immunoglobulin A (IgA)-producing programmed death-ligand 1-positive cells suppressing efficient anti-liver cancer immune responses.[24] In a mouse model of NASH, it was shown that intrahepatic B cells, activated by gut-derived microbial factors, contributed to hepatic inflammation and fibrosis,[25] while another mouse study demonstrated that intrahepatic regulatory B cells were involved in disease pathogenesis.[26] Moreover, further studies have shown a role of IgA in liver diseases, such as alcohol-related liver disease and NAFLD/NASH[27]. However, the exact role and origin of B cells in NASH, and the involvement of B cells in T-cell activation and fibrosis initiation and/or development, remain unclear. Herein, we report that intestinal $CD20^+$ B cells and immunoglobulin secretion are involved in the pathogenesis of NASH in mice and humans and that peripheric IgA^+ and MoMFs-FcRγ signalling contribute to NASH-induced liver fibrosis.

Material and methods

Details on the materials and methods are provided in the supplementary information and the supplementary CTAT table.

Results

B cells are required for NASH and NASH-driven HCC in mice

To investigate the role of systemic B cells in NASH, C57BL/6J wild-type (WT) littermates and B cell-deficient ($JH^{-/-}$) mice[28] were fed a NASH-inducing choline-deficient high-fat diet (CD-HFD) for 6 or 12 months. As previously described, WT CD-HFD mice developed NASH (after approx. 6 months – 100% penetrance) and HCC (approx. 30% incidence at 12 months post-diet-start), recapitulating several clinical features of human disease.[29] $JH^{-/-}$ CD-HFD mice gained significantly more weight than normal chow-fed (ND) controls at around 9 months of age, reaching the same body weight as WT CD-HFD mice at 12 months post-diet-start (Fig. S1B). $JH^{-/-}$ CD-HFD mice lacked liver steatosis and had a low NAFLD activity score (NAS) after 6 months (Fig. 1A,B and Fig. S1A) and 12 months on diet (Fig. S1G,H). High serum alanine aminotransferase (ALT) values, typically seen in WT CD-HFD mice, were low in $JH^{-/-}$ CD-HFD serum at 6 (Fig. 1C and Fig. S1A) and 12 months (Fig. S1G). Serum cholesterol and hepatic triglyceride levels were lower in $JH^{-/-}$ than in WT CD-HFD mice at both time points (Fig. S1A,G), with a substantial decrease in hepatic large lipid droplets (Fig. 1D). Intraperitoneal glucose tolerance test revealed normal insulin response in $JH^{-/-}$ CD-HFD mice, contrary to WT CD-HFD mice (Fig. S1C). Flow cytometry analyses showed significantly fewer $CD3^+$ and $CD8^+$ T cells in $JH^{-/-}$ CD-HFD livers than in WT (Fig. S1E) and confirmed the absence of $CD19^+$ B cells (Fig. S1F). A similar reduction in $CD3^+$ cells was observed by immunohistochemistry (IHC) analysis of $JH^{-/-}$ CD-HFD liver sections (Fig. S1D). Hepatic $CD8^+$ $CD62L^-$ activated T cells TNF and IFNγ-producing $CD8^+$ cells were decreased (Figs. 1E-G) similarly to myeloid cells, as seen by staining for $F4/80^+$ cells and MHC-II^+ aggregates (Fig. S1D). $P62^+$, cleaved Caspase 3^+ cells, and $PD1^+$ cells were increased in WT CD-HFD livers compared to WT ND but remained significantly lower in $JH^{-/-}$ CD-HFD livers (Fig. S1D).[3,30]

To evaluate the importance of B cells in NASH, we therapeutically depleted B cells using anti-CD20 monoclonal antibodies (αCD20 mAb) in WT mice with NASH fed a CD-HFD for 4 months (Fig. 1H). Before treatment, we confirmed NASH 4 months post diet-start in mice from the identical mouse cohort (Fig. S1J,K). B-cell depletion was performed for 6 weeks on CD-HFD mice, and depletion efficacy was evaluated in the liver, small intestine (Peyer's patches removed) (Fig. 1I,J), the spleen, and blood (Fig. S1N,O). In agreement with the genetic model, WT CD-HFD αCD20 mAb-treated mice lacked NASH (Figs. 1K,L and Fig. S1I), and ALT serum levels were significantly reduced compared to controls (isotype control-treated or untreated WT CD-HFD mice) (Fig. 1M and Fig. S1I). WT CD-HFD αCD20 mAb-treated mice showed lower body weight at the endpoint (Fig. S1L) and a strong reduction of hepatic large lipid droplets (Fig. 1N). Accordingly, hepatic triglycerides and serum cholesterol were decreased (Fig. 1O and Fig. S1I). Intraperitoneal glucose tolerance test revealed impaired insulin responses in the αCD20 mAb-treated mice, similar to WT CD-HFD (Fig. S1M). B-cell depletion reduced the accumulation of hepatic $CD3^+$, $CD8^+$ (Fig. S1P,Q), $CD8^+$ $CD62L^-$, $CD8^+$ TNF^+

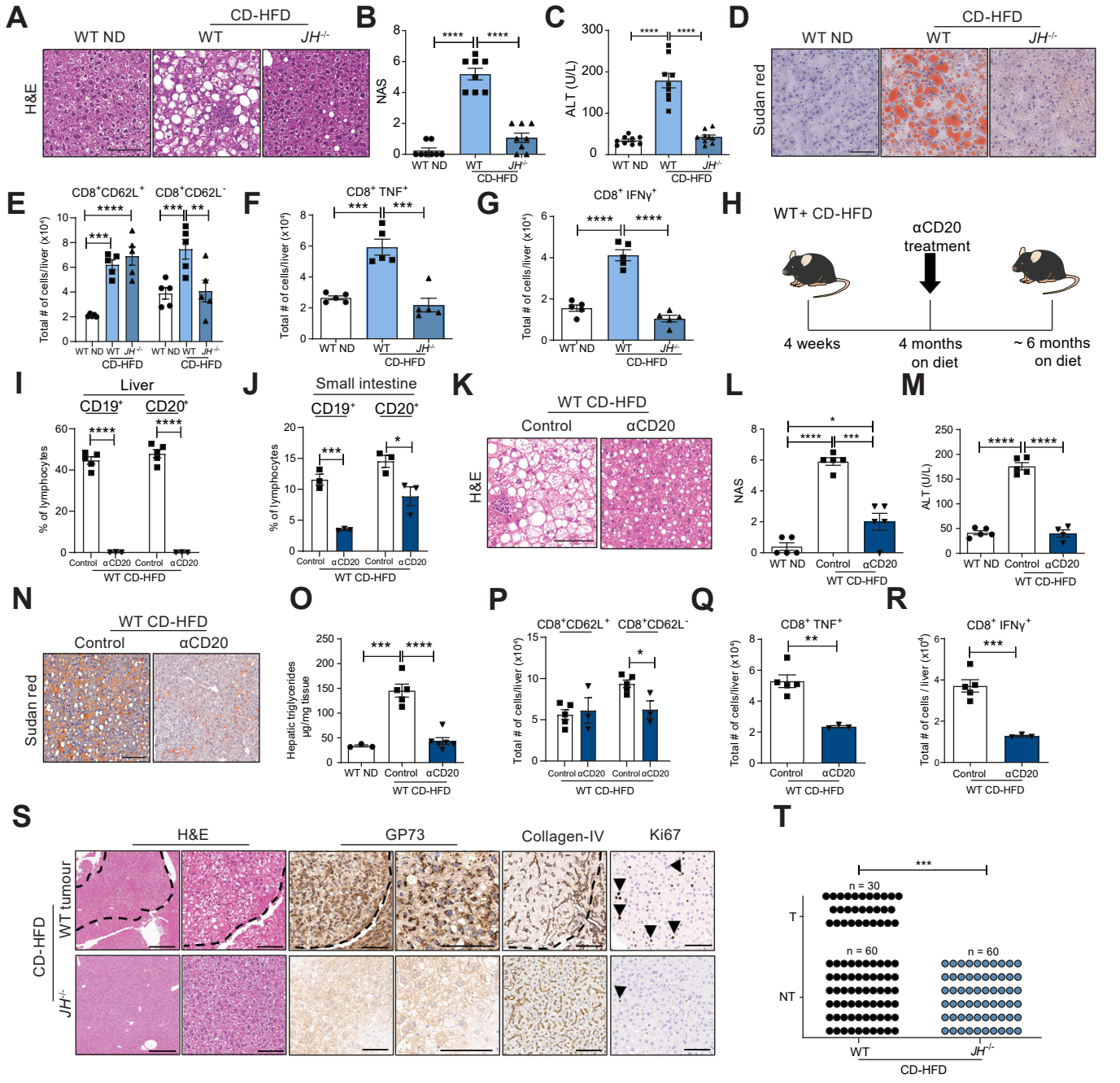

Fig. 1. B cells support NASH and subsequent HCC development. (A) Representative H&E staining of liver sections derived from WT ND, CD-HFD and *JH*$^{-/-}$ CD-HFD male mice fed for 6 months. (B) NAFLD score evaluation (n = 8). (C) Serum ALT levels (n = 9). (D) Representative Sudan red analysis of liver sections of male mice fed for 6 months. (E-G) Quantifications of the total number of cells (absolute number) of liver flow cytometry analyses of male mice (n = 5) fed for 6 months (numbers indicate %) of (E) hepatic CD8$^+$CD62L$^+$ and CD8$^+$CD62L$^-$ T cells, (F) CD8$^+$TNF$^+$ cells, (G) CD8$^+$IFNγ$^+$ cells, derived from livers of the respective genotypes/groups fed for 6 months. (H) Treatment scheme for the WT CD-HFD male mice treated with B-cell depletion antibody anti-CD20 (αCD20). (I) Quantifications of flow cytometry analyses of liver CD19$^+$ and CD20$^+$ cells and (J) lamina propria small intestine CD19$^+$ and CD20$^+$ cells, comparing control and WT CD-HFD αCD20-treated male mice (n ≥3). All mice were fed for 6 months. (K) Representative H&E staining of liver sections. (L) NAS evaluation of mice (n = 5). (M) Serum ALT levels in male mice (n = 5). (N) Representative Sudan red staining of liver sections of control and WT CD-HFD αCD20-treated male mice. (O) Analysis of hepatic triglycerides in male mice (n ≥3). (P–S) Quantification of flow cytometry analyses comparing control-treated and WT CD-HFD αCD20-treated male mice (n ≥3) of (P) hepatic CD8$^+$CD62L$^+$ and CD8$^+$CD62L$^-$ cells; quantification of (Q) hepatic CD8$^+$TNF$^+$ cells and (R) CD8$^+$IFNγ$^+$ cells. (S) Representative H&E staining and IHC staining of GP73, collagen IV and Ki67 for WT CD-HFD tumours and for not-affected livers of *JH*$^{-/-}$ CD-HFD; from 12 months fed CD-HFD mice. Scale bars represent H&E: 500 µm (left) and 100 µm (right); GP73: 100 µm; collagen IV: 100 µm; Ki67: 100 µm (positive hepatocytes depicted by arrowheads). (T) Graph summarizing non-tumour (NT) and tumour (T), of WT and *JH*$^{-/-}$ mice fed with CD-HFD for 12 months (numbers of mice are indicated, as symbols depict individual mice), data were analysed by Fisher's exact test. All data are presented as mean ± SEM. Statistical analyses were performed using unpaired *t* test. Displayed scale bars represent 100 µm.

and CD8$^+$ IFNγ^+ cells (Fig. 1P-R). IHC confirmed the efficient depletion of B220$^+$ cells and revealed decreased F4/80$^+$ cells and MHC-II$^+$ cell aggregates in WT CD-HFD αCD20 mAb livers (Fig. S1Q).

Metabolomic analysis revealed an altered metabolic hepatic profile of CD-HFD-treated mice in the absence of B cells (*e.g.*, triglycerides), both genetically and therapeutically. Hepatic deregulation of several lipid and cholesterol metabolism genes,

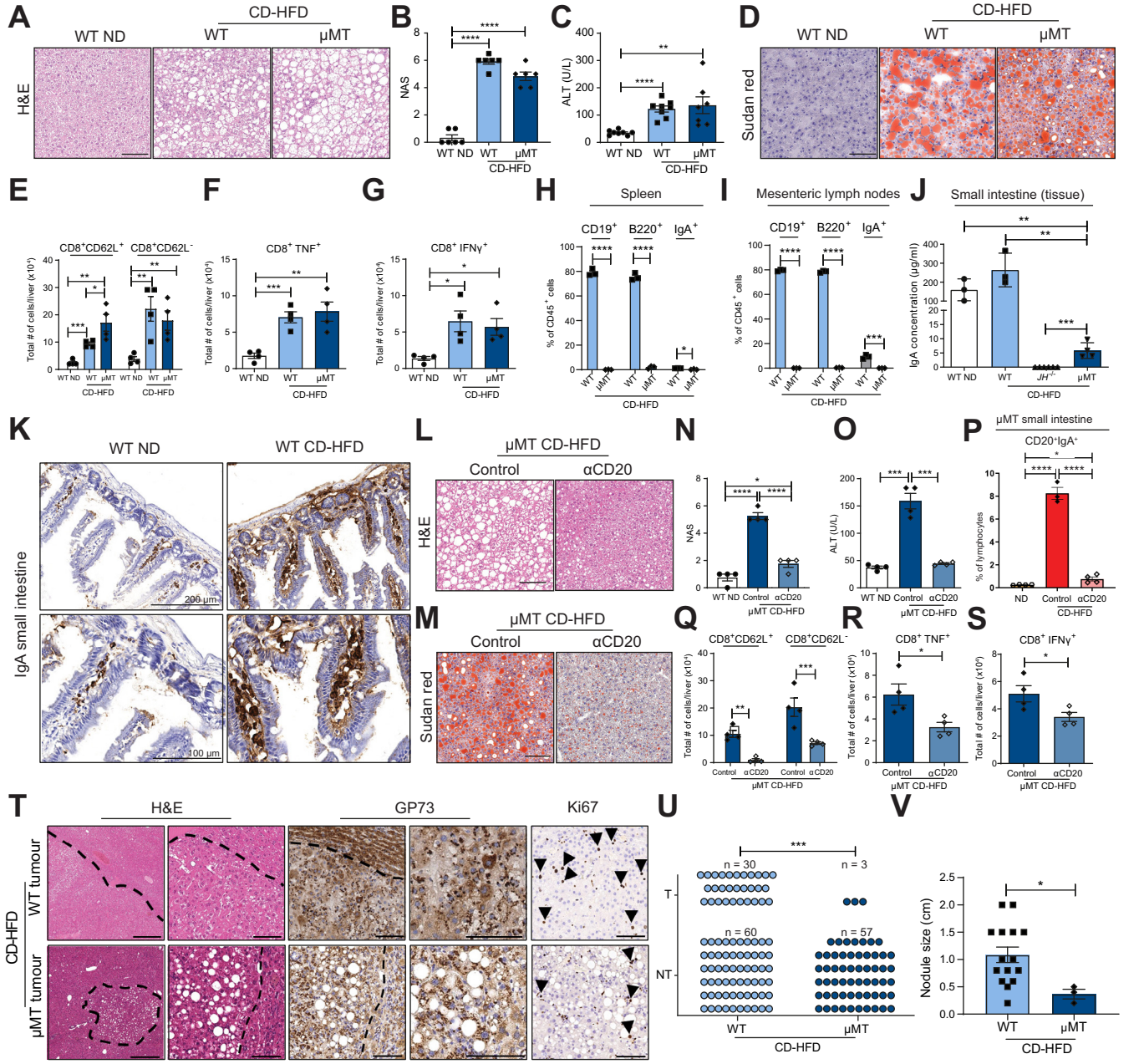

Fig. 2. Intestinal B cells suffice to cause NASH. (A) Representative H&E staining of liver sections of WT ND, WT and *μMT* CD-HFD male mice fed for 6 months. (B) NAS male mice (n = 6). (C) Serum ALT levels in male mice (n ≥6). (D) Representative Sudan red staining of liver sections. (E) Absolute quantifications of flow cytometry of hepatic CD8$^+$CD62L$^+$ and CD8$^+$CD62L$^-$ T cells, (F) for CD8$^+$TNF$^+$ cells and (G) CD8$^+$IFNγ^+ cells (n = 4). (H) Percentages of splenic CD19$^+$, B220$^+$ and IgA$^+$ cells in male mice (n = 3), evaluated by flow cytometry. (I) Percentages of CD19$^+$, B220$^+$ and IgA$^+$ cells from mesenteric lymph nodes of male mice (n = 3), evaluated by flow cytometry. (J) IgA levels of small intestinal tissues in male mice (n ≥3), measured by ELISA. (K) Representative IgA staining of small intestine sections of 6-month-old male mice (upper row: scale bar 200 μm, bottom row scale bar: 100 μm). (L) Representative H&E staining of liver sections of 6-month-old *μMT* CD-HFD and μMT CD-HFD αCD20-treated male mice. (M) Representative Sudan red staining of liver sections of male mice. (N) NAS evaluation of male mice (n = 4). (O) ALT levels in male mice (n = 4). (P) Flow cytometric analysis quantifications of lamina propria CD20$^+$IgA$^+$ cells. (Q) Absolute quantifications of hepatic CD8$^+$CD62L$^+$ and CD8$^+$CD62L$^-$ cells (n = 4). (R) Hepatic CD8$^+$TNF$^+$ and (S) CD8$^+$IFNγ^+ cells, comparing WT ND, *μMT* CD-HFD and *μMT* CD-HFD αCD20-treated male mice (n = 4). (T) Representative H&E and IHC staining of GP73 and Ki67 in WT and *μMT* CD-HFD tumours (12 months under diet). Scale bars H/E: 500 μm (left) and 100 μm (right); GP73: 100 μm; Ki67: 100 μm (positive hepatocytes depicted by arrowheads). (U) Graph summarizing non-tumour (NT) and tumour (T) of WT and *μMT* mice fed with CD-HFD for 12 months (n ≥60). Symbols depict individual mice. Data were analysed by Fisher's exact test. (V) Quantification of nodule size in 12-month WT and μMT CD-HFD mice (n ≥3). All data are presented as mean ± SEM. Statistical analyses were performed using unpaired *t* test. The scale bars represent 100 μm.

usually found in NASH livers,[3,20,29] was prevented in *JH*$^{-/-}$ CD-HFD mice (Fig. S1R). In addition, proton nuclear magnetic resonance (^{1}H-NMR) spectroscopy analyses identified altered liver lipids correlating with the absence of B cells (Fig. S1S).

Of 60 *JH*$^{-/-}$ CD-HFD mice at 12 months post-diet start, none displayed liver cancer, unlike WT CD-HFD mice, which developed HCC at an incidence of 30%[20,29] (Fig. 1S,T). Together, our data indicate a key role of systemic B-cell responses in the development and maintenance of NASH and NASH-driven HCC.

Small intestine B-cell responses are sufficient to induce NASH in mice

To investigate and further corroborate the role of intestinal B cells in NASH and liver fibrosis, we utilized a second B cell-deficient mouse model (*μMT* mice), lacking expression of membrane-bound immunoglobulin M (IgM) on B cells. μMT mice selectively develop IgA^{+} B cells without IgM or IgD heavy chain expression by using alpha rather than the mu constant region chain[31] and only develop in the gastrointestinal tract. CD-HFD *μMT* mice gained significantly more weight than controls (Fig. S2B) and developed comparable NASH levels as in WT CD-HFD at 6 (Fig. 2A, 2B and Fig. S2A) and 12 months post-diet start (Figs. S2O, S2P). Serum ALT and cholesterol levels of *μMT* CD-HFD mice were similar to WT CD-HFD at 6 and 12 months (Figs 2C and Fig. S2A,O). Accumulated hepatic lipid droplets and increased hepatic triglycerides were observed in *μMT* CD-HFD mice for both time points (Fig 2D and Fig. S2A,O). An increase in activated intrahepatic CD8^{+} T cells with elevated TNF^{+} and IFNγ^{+} expression, as well as an impaired insulin response, were observed in *μMT* CD-HFD mice (Fig. 2C,E-G). Due to their lack of follicular B cells (Fig. 2H,I and Fig. S2F), μMT CD-HFD spleens lacked structured architecture (*e.g.*, germinal centres) (Fig. S2D). Flow cytometry analysis of small intestines from *μMT* CD-HFD mice identified IgA^{+} B cells, contrary to *JH*$^{-/-}$ CD-HFD mice (Fig. S1G). WT CD-HFD mice exhibited increased IgA levels in the ileum of the small intestine compared with ND control mice; IgA was present at low levels in the small intestine of *μMT* CD-HFD mice but was absent in CD-HFD *JH*$^{-/-}$ mice (Fig. 2J,K). An abundance of IgA^{+}-coated bacteria in *μMT* faeces indicates a local secretion of IgA into the intestinal tract (Fig. S2K). Increased IgM and IgG2b found in the small intestine of WT-CD-HFD mice (Fig. S2H) were undetectable in both *JH*$^{-/-}$ and *μMT* mice. IHC analysis demonstrated a lack of intrahepatic B cells in *μMT* CD-HFD mice (Fig. S2L) and an increase in F4/80^{+} cells and MHC-II^{+} aggregates compared to ND mice (Fig. S2L), contrary to *JH*$^{-/-}$ CD-HFD mice. P62^{+} and cleaved caspase 3^{+} cells were increased in *μMT* CD-HFD mice, as in WT CD-HFD mice (Fig. S2L). Moreover, transcriptional analyses of *μMT* CD-HFD livers demonstrated altered expression of several genes involved in lipid and cholesterol metabolism (Fig. S2N).

To investigate whether the susceptibility of *μMT* mice to liver inflammation was due to B cells in the intestine, we depleted the latter following feeding with CD-HFD for 4 months in mice with established NASH (Fig. S2Q,R). αCD20-antibody treatment reversed NASH in *μMT* CD-HFD mice (Figs. 2L,N and Fig. S2S), which displayed slightly lower body weight at endpoint than the control-IgG-treated mice (Fig. S2T). Serum ALT and cholesterol levels were significantly reduced (Fig. 2O and Fig. S2S), large lipid droplets were strongly decreased (Fig. 2M), and hepatic triglycerides and serum cholesterol were significantly reduced in αCD20 antibody-treated mice (Fig. S2S). Flow cytometry analysis of small intestines from CD-HFD μMT mice revealed a significant increase in CD20^{+} IgA^{+} B cells compared with *μMT* ND-fed mice, highlighting the NASH-induced gastrointestinal B-cell accumulation, which was reduced by αCD20-antibody treatment (Fig. 2P and Fig. S2U). In addition, flow cytometry analysis revealed a strong decrease of hepatic CD3^{+}, CD8^{+} (Fig. S2W), CD8^{+} CD62L^{-}, and CD8^{+} TNF^{+} and CD8^{+} IFNγ^{+} cells in αCD20-treated *μMT* CD-HFD-fed mice (Fig. 2Q-2S). This observation was corroborated by IHC (Fig. S2V), which also revealed a reduction in F4/80^{+} cells and MHC-II^{+} aggregates in αCD20-treated *μMT* CD-HFD mice compared to controls.

Notably, of 60 μMT mice fed a CD-HFD for 12 months, only three mice displayed liver tumours (not HCC; incidence of ≤5%) contrary to WT CD-HFD mice, as also described in Fig. 1S (same control cohort) and with smaller nodule size than in WT (Fig. 2T-2V). Thus, we conclude that intestinal B cells suffice for the development of diet-induced NASH, yet tumour incidence is strongly reduced.

Intestinal B cells interact with CD8^{+} T cells

We performed a multi-parameter flow cytometry analysis of the small intestine with Peyer's patches removed to identify distinct gut B-cell populations correlated with NASH. In line with our previous data, increased B cells were found in WT CD-HFD compared with ND mice. Notably, B cells (approx. 10% of CD45^{+} cells) downregulated CD19^{+} but retained CD20^{+} expression in small intestines of *μMT* CD-HFD mice (Figs. 3A, 3B). In addition, more IgM^{high}IgD^{high} and IgM^{low}IgD^{high} B cells were identified in WT CD-HFD compared to ND mice. As expected, μMT CD-HFD mice lacked B cells expressing IgM and/or IgD (Fig. 3C). More CD20^{+}MHC-II^{+} and CD20^{+}IgA^{+} B cells were found in WT CD-HFD compared to ND mice, whereas the latter were not increased in μM CD-HFD mice (Fig. 3D,E).

CD20^{+}IgA^{+}MHC-II^{+} cells were significantly elevated in WT CD-HFD small intestines (Fig. 3F), suggesting a potentially enhanced activation of these cells. CD20^{+}IgA^{+}CXCR4^{+} cells were also elevated in WT CD-HFD small intestines but were not detectable in *μMT* CD-HFD mice (Fig. 3G,H and Fig. S3A), indicating that B cells in small intestines of *μMT* mice most likely were not plasma blasts or plasma cells, since CXCR4 expression promotes the survival of long-term plasma cells.[32] Flow cytometry revealed more IgA^{+} and IgA^{+}B220^{-}CD20^{-} cells in WT CD-HFD small intestines, whereas, in *μMT* CD-HFD mice, this population remained at the same levels as in WT ND mice (Fig. 3I and Fig. S3B). IgA^{+}B220^{-}CD20^{-}CXCR4^{+} were significantly increased in WT CD-HFD but significantly less in *μMT* CD-HFD mice (Fig. 3J and Fig. S3C).

Cytometric t-distributed stochastic neighbour embedding (t-SNE) flow cytometry data analysis revealed a B-cell population diversity among the three investigated groups (Fig. 3K). We previously identified CD8^{+} T cells as important mediators of NASH and NASH-HCC(3, 4). Therefore, we investigated the

possible influence of intestinal B cells on this cell population. Flow cytometry analysis identified more $CD8^+$ T cells in *μMT* CD-HFD small intestines compared to WT CD-HFD and ND controls (Fig. S3F), and increased $CD8^+$ $CD44^+$ and $CD8^+$ $PD1^+$ cells were identified in WT and *μMT* CD-HFD small intestines (Fig. S3D, S3E). Moreover, cytometric t-SNE analysis showed diversity in the clustering of the $CD8^+$, $CD44^+$ and $PD1^+$ T-cell populations between the three groups (Fig. 3L).

3D high resolution of B–T-cell interactions in small intestines of WT ND and CD-HFD mice revealed $B220^+$ B cells co-localized with $CD8^+$ T cells. We observed significantly more interacting cell clusters (yellow) in WT CD-HFD intestines compared with ND controls (Fig. 3M and 3Q). Elevated $B220^+$ and $CD8^+$ cell interactions were also observed inside the villi of WT CD-HFD mice, suggesting a migratory phenotype of these cells (Fig. S3I, S3J). STRING[33] pathway enrichment and ImmuNET[34]bib34 analysis of functional relationship networks from RNA-sequencing data retrieved from $CD20^+$ and $B220^+$ sorted cells from WT ND, WT CD-HFD and μMT CD-HFD small intestines revealed enhanced expression of genes related to antigen presentation and BCR signalling, IgA production and B-cell activation and differentiation, and lipid metabolism (Figs. 3O, 3P and Fig. S3K,L), in both WT and *μMT* CD-HFD mice compared to ND controls.

To investigate whether intestinal B and T cells migrate from the gut to the liver during NASH, Kaede transgenic mice,[35] which constitutively express a photoconvertible fluorescent protein in all cells, were fed two different NASH diets, CD-HFD and western diet (WD) with trans-fat,[36] for 6 months. At 6 months, the gastrointestinal tissue of Kaede mice was photo-converted to label cells from green to red, enabling direct tracing of cells from the gastrointestinal tract to other tissues (Fig. 3R). Flow cytometry analyses of liver tissue revealed intestinal B cells migrating to the liver with fewer $B220^+$ $CD19^+$ $MHC\text{-}II^+$ B cells in the NASH-affected livers (red cells) compared to ND controls (Fig. 3S). Notably, liver $CD3^+$ cells migrating from the gut (red cells) were significantly increased compared with ND controls (Fig. 3S), suggesting that more T cells migrate from the gut to the liver during NASH.

We next aimed to assess if intestinal B cells derived from NASH-affected mice promote $CD8^+$ T-cell activation. To evaluate this, we co-cultured intestinal B cells from ND or CD-HFD mice with splenic $CD44^+$ $CD8^+$ T cells from ND mice and triggered TCR activation using anti-CD3/CD28 antibodies. $CD8^+$ T cells cultured with B cells from CD-HFD intestines exhibited significantly higher levels of the activation markers CD25 and CD69 than those cultured with B cells from ND mice after 24 h, which increased at 48 h. Likewise, these cells showed higher expression of the hallmarks of auto-aggressive T cells, namely CXCR6, PD1 and CTLA4, compared to T cells cultured with ND-derived B cells (Fig. 3T).

To investigate whether B cell-induced auto-aggression requires TCR-MHC-I or cell-cell interactions, we blocked MHC-I or LFA-1 and ICAM-1. Indeed, blockade of ICAM-1 or LFA-1 but not MHC-I abrogated B cell-induced T-cell activation *ex vivo* (Fig. 3T). To address whether observed B cell-induced T-cell activation is antigen-dependent, we used OT1 T cells harbouring transgenic TCR that recognizes only ovalbumin-derived antigens. OT1 T cells were activated by B cells derived from the gastrointestinal tract of NASH mice, supporting the notion of an antigen-independent metabolic activation (Fig. 3M). Collectively, these results indicate that in NASH conditions, intestinal B cells induce $CD8^+$ T-cell hyper-activation via ICAM-1 and LFA-1 but not TCR:MHC-I, indicating an antigen-independent activation mechanism.

These data suggest an altered metabolic and activated B-cell profile in the small intestine of NASH-affected mice. In addition, our data suggest that B cells from NASH-affected intestines cluster with $CD8^+$ T cells through direct cell-cell interaction, independent of an antigen but necessitating B-T cell interactions, which are stabilized via co-stimulatory molecules LFA-1 and ICAM1. Finally, our data indicate that intestinal B and T cells can efficiently migrate from the gut of NASH-affected mice to the liver.

IgA is sufficient to induce NASH in mice

To determine whether immunoglobulin secretion was required for NASH development, mice exhibiting normal B-cell development but lacking secreted immunoglobulin (*IgMi* mice[37,38]) were fed a CD-HFD for 6 months. We first tested whether these mice could develop normal immune responses, *e.g.* in a mouse model of multiple sclerosis. We found that the *IgMi* mice developed neurological impairment at a severity equivalent to WT when subjected to experimental allergic autoimmune encephalomyelitis (Fig. S4A), and *IgMi* T cells produced the same level of IL-2 as WT T cells when exposed to myelin oligodendrocyte glycoprotein peptide[39] (Fig. S4B). Thus, adaptive immune responses in these mice are largely intact. Despite similar development of obesity compared to WT CD-HFD mice, *IgMi* mice lacked signs of NASH upon CD-HFD (Fig 4A-C and Fig. S4C). Serum ALT and cholesterol, hepatic lipid deposition and hepatic triglycerides were significantly reduced in *IgMi* CD-HFD mice (Figs 4D,E and Fig. S4C). The number of $B220^+$ and $CD19^+$ cells remained unaltered (Fig. 4I and Fig. S4D), whereas $CD3^+$, $CD8^+$ $F4/80^{+,}$ and $MHC\text{-}II^+$ cells were significantly lower in IgMi CD-HFD livers (Fig. S4D, S4E). Moreover, $P62^+$ and cleaved caspase 3^+ cells were reduced in *IgMi* CD-HFD compared to WT CD-HFD mice (Fig. S4D). In addition, significantly fewer $CD8^+$, $CD8^+CD62L^+$, $CD8^+CD62L^-$ cells and $CD8^+TNF^+$ and $CD8^+IFN\gamma^+$ cells were observed in *IgMi* CD-HFD mice (Fig. 4F-H). Notably, flow cytometry analysis of the small intestine revealed the same increase in $CD20^+$, $CD20^+MHC\text{-}II^+$ and $CD8^+$ cells in IgMi and WT CD-HFD mice compared to controls, with *IgMi* mice demonstrating deficient levels of $CD20^+IgA^+$ cells,[37,38] as expected (Fig. 4L). Importantly, 3D high-resolution of immune cell interactions of B and T cells in the small intestine of WT ND, WT CD-HFD and *IgMi* CD-HFD mice (yellow) revealed a lack of interaction between $B220^+$ and $CD8^+$ cells in *IgMi* mice (Fig. 4J,K). The elevated $B220^+$ and $CD8^+$ interactions observed inside the villi of the WT CD-HFD intestines - when compared with ND controls - were not observed in the *IgMi* CD-HFD intestines (Fig. S4F). Astoundingly, IgMi mice displayed a reduction of phosphorylated SYK (a tyrosine-protein kinase mediating immune-cell activation pathways, such as BCR signalling) in immune cells of the small intestine, contrary to WT or *μMT* mice on CD-HFD (Fig. S4G).

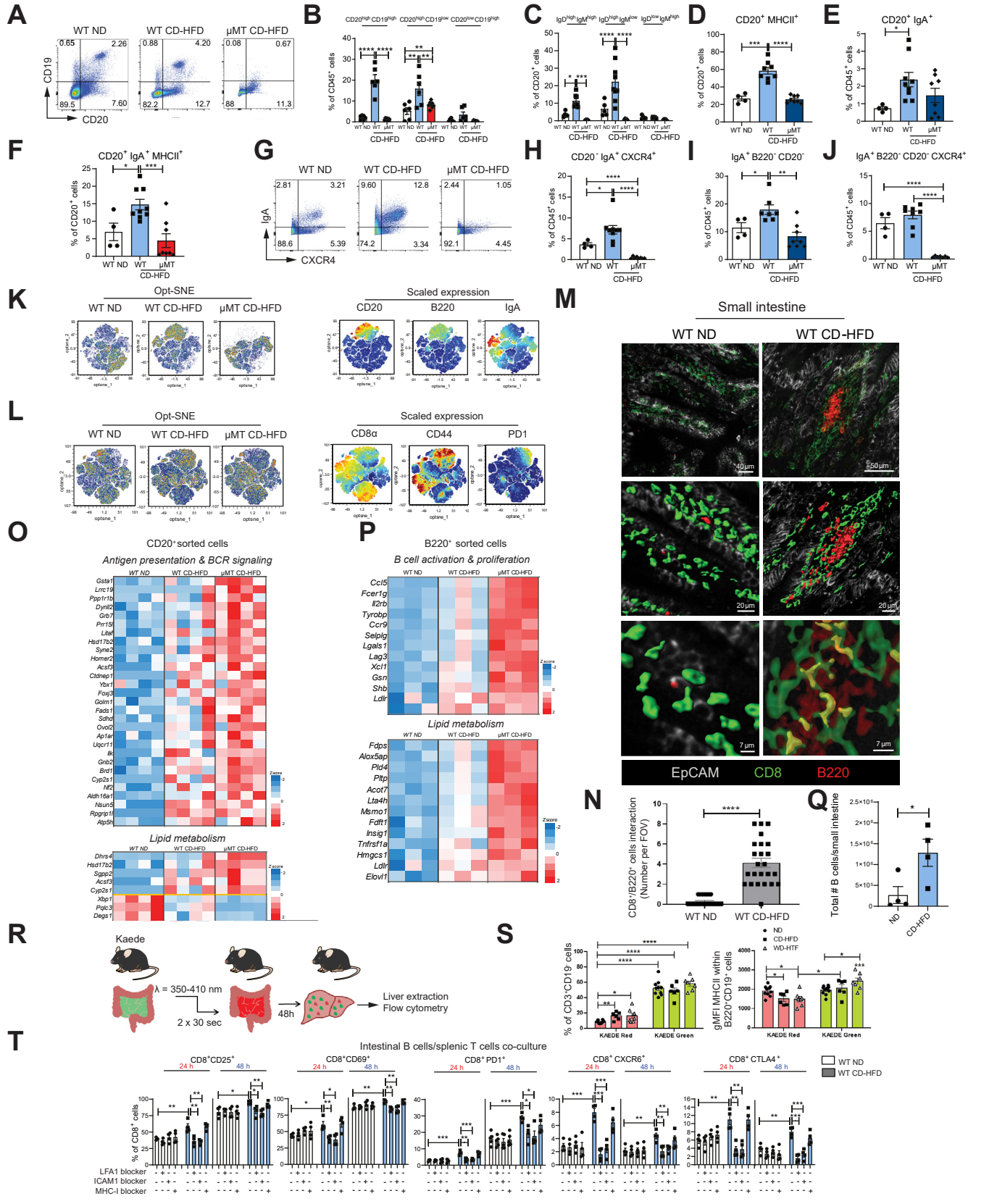

Fig. 3. B cells get metabolically activated and form clusters with T cells in the lamina propria of NASH-bearing mice. All data represent the small intestine. (A-J) Representative pseudocolor plots and quantifications of flow cytometric analyses comparing small intestine lamina propria from WT ND, WT CD-HFD and *μMT* CD-HFD male mice (≥4): (B) percentages of $CD20^+CD19^+$, $CD20^+CD19^-$, $CD20^-CD19^-$ cells, (C) IgD^+IgM^+, IgD^+IgM^-, IgD^-IgM^+ cells, (D) $CD20^+$MHC-II^+ cells, (E) $CD20^+IgA^+$ cells, (F) $CD20^+IgA^+$MHC-II^+ cells, (G) representative pseudocolor plots for IgA^+ and $CXCR4^+$ cells, (H) percentages of $CD20^-IgA^+CXCR4^+$ cells, (I) $IgA^+B220^-CD20^-$ cells, and (J) $IgA^+B220^-CD20^-CXCR4^+$ cells. (K) Automated optimized parameters for T-distributed stochastic neighbour embedding (opt-SNE) graphs from flow cytometric analysis of male mice (n = 9) displaying B cells. On the left, opt-SNE plots indicate scaled expression of CD20, B220 and IgA. (L) Opt-SNE graphs from flow

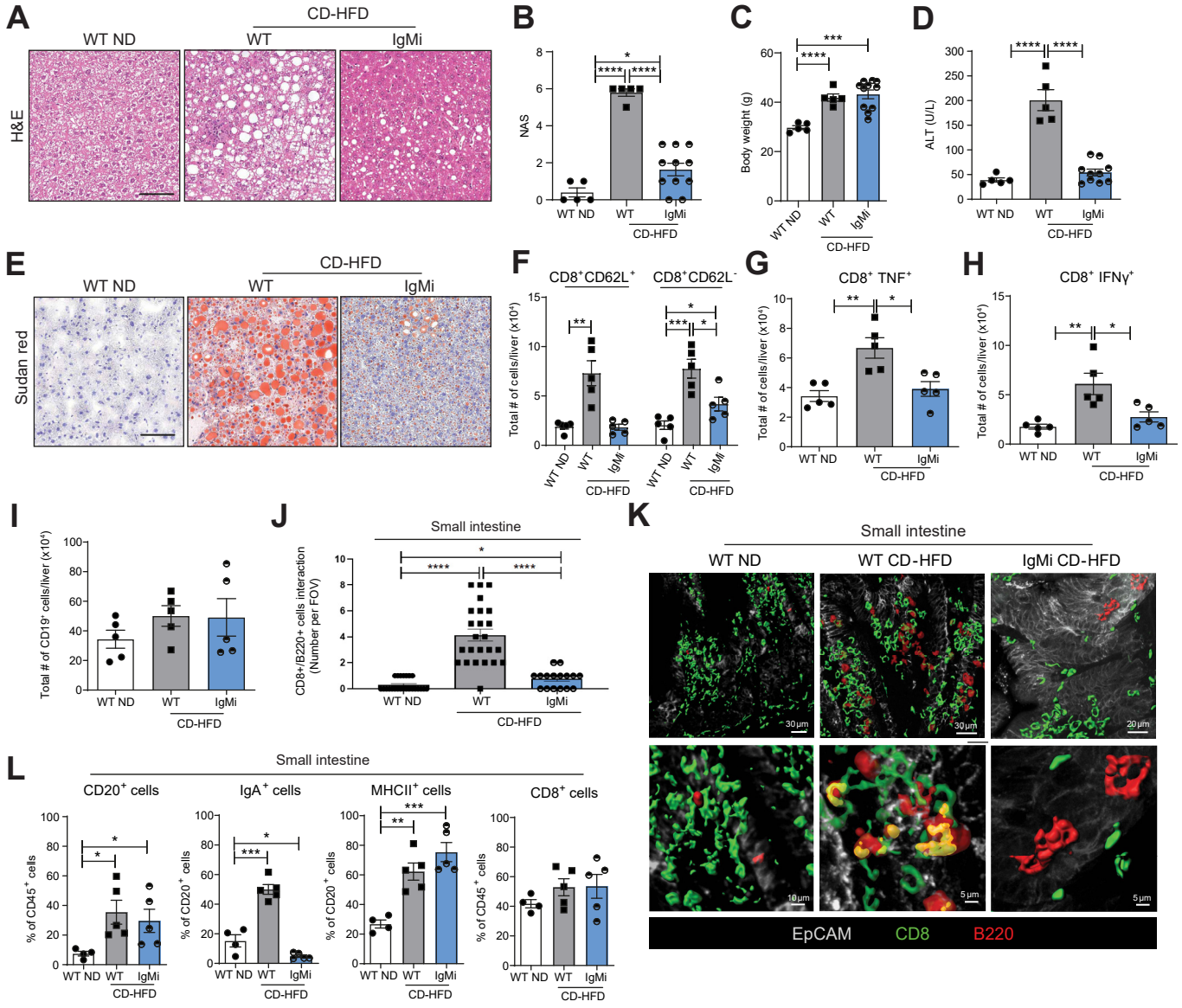

Fig. 4. Immunoglobulin secretion by B cells is essential for NASH development. (A) Representative H&E staining of liver sections from WT ND, WT CD-HFD and *IgMi* CD-HFD mice fed for 6 months. (B) NAS and (C) body weight measurement of male mice at 6 months post-diet-start (n ≥5). (D) Serological ALT male mice (n ≥5). (E) Representative Sudan red of liver sections. (F–I) Quantification of flow cytometry for (F) hepatic total CD8+CD62L+ and CD8+CD62L-cells, (G) total CD8+TNF+ cells, (H) total CD8+IFNγ+ cells, (I) total CD19+ cells, in male mice (n ≥4). (J) Quantification of hepatic clusters of B220+/CD8+ interacting cells in male mice (n = 3 for WT controls, n = 2 for IgMi CD-HFD mice, with n = 8 FOV each mouse). (K) Representative high-resolution confocal microscopy and 3D reconstruction images of small intestine lamina propria staining for B220+ cells and CD8+ cells (yellow areas indicate cell-cell contact between B220+ and CD8+ cells). (L) Quantification of flow cytometric analyses of small intestine CD20+, IgA+ cells, MHC-II+ cells, of CD8+ cells. All data are presented as mean ± SEM. Statistical analyses were performed using unpaired *t* test. Scale bars represent 100 µm, or as indicated.

cytometric analysis of male mice (n = 9) displaying T cells and scaled expression of CD8α, CD44 and PD1. (M) Representative high-resolution confocal microscopy and 3D reconstruction images of small intestine lamina propria staining for B220$^+$ and CD8$^+$ cells (yellow areas indicate a point of contact among B220$^+$ and CD8$^+$ cells), and (N) quantification of clusters of B220+/CD8+ interacting cells, (number cells interactions per field of view, FOV), in WT ND and WT CD-HFD (n = 3, with n = 8 FOV each mouse). (O, P) Heatmaps of immune system-related genes and metabolic process-related genes significantly different in small intestine lamina propria FACS-sorted (O) CD20$^+$ cells or (P) B220$^+$ cells isolated from WT and *µMT* CD-HFD *vs.* WT ND, indicated as z-scaled values. (Q) Flow cytometry quantification of total living B cells isolated from small intestine derived from male mice (6 months of diet) (n = 4). (R) Descriptive scheme for the flow cytometry performed with a transgenic mouse model of Kaede mice, bearing the photoconvertible fluorescence Kaede protein, which changes from green to red upon exposure to violet light: immune cells stained in red indicate migration into the liver from the small intestine; instead, cells stained in green are migrating immune cells from any other organ. (S) On the left, flow cytometric analysis indicates frequencies of liver CD3$^+$CD19$^-$ cells (n ≥5). On the right, geometrical MFI from flow cytometry analysis of Kaede red or green liver B220$^+$CD19$^+$ cells in ND, CD-HFD and WD-HTC mice (n ≥5). (T) Percentages of flow cytometry analysis of splenic CD8+CD69+, CD8+CD25+, CD8+PD1+, CD8+CXCR6+ and CD8+CTL4+ cells from CD44+CD8+ cells; splenic T cells isolated from a healthy mouse were stimulated with Dynabeads (anti-CD3/CD28) and were co-cultured for 24 or 48 h with intestinal B cells isolated from WT ND or WT CD-HFD. Additional treatments included Dynabeads plus LFA-1 blocker, or ICAM-1 blocker, or MHC-I blocker (n = 4). All data are presented as mean ± SEM. Statistical analyses were performed using unpaired *t* test.

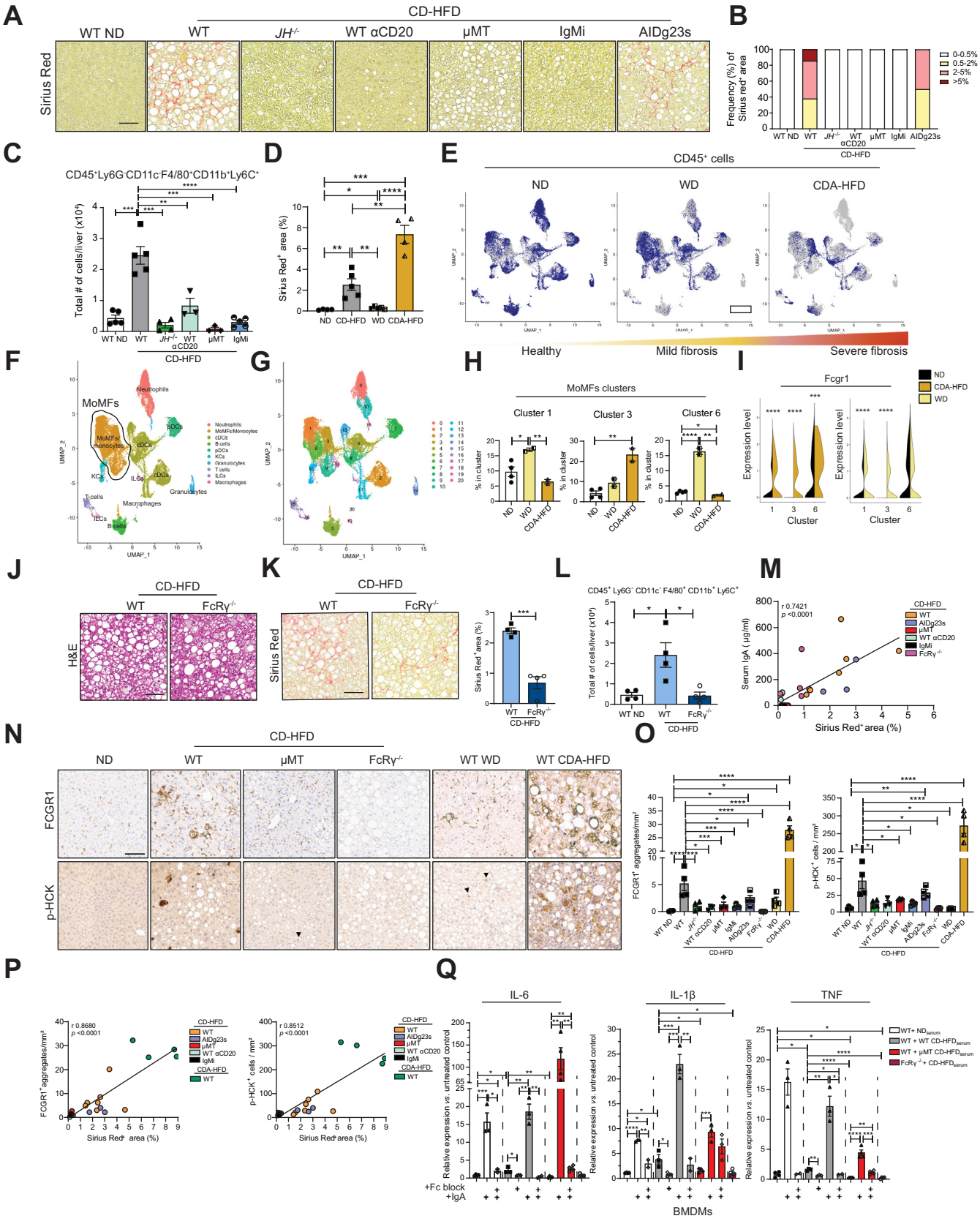

Fig. 5. FcR signalling activated in macrophages through IgA drives hepatic fibrosis in NASH. (A) Sirius red staining representative images from livers of WT ND and WT, *JH*$^{-/-}$, WT αCD20-treated, *μMT*, *IgMi*, *AIDg23s* mice (all under CD-HFD for 6 months). (B) Percentages of fibrosis incidence divided among the different degrees of fibrosis (mild 0.5-2%; moderate 2-5%; severe >5%) in above-mentioned mouse groups. (C) Quantifications of liver flow cytometric analyses of total CD45^{+}Ly6G^{-}Cd11c^{-}F4/80^{+}CD11b^{+}Ly6C^{+} cells from WT ND and WT, *JH*$^{-/-}$, WT αCD20-treated, *μMT*, *IgMi* mice under CD-HFD (n ≥3). (D) Sirius red quantification of

Overall, these observations suggest that secretion of IgA and IgM is important to support T-cell activation by metabolically activated B cells, with a crucial role in NASH induction. Intestinal membrane-bound IgA might affect the intensity and quality of B–T-cell interactions in the small intestine of NASH-affected mice.

NASH-induced fibrosis depends on IgA and Fc receptor signalling

NASH levels were the same in both WT and *μMT* CD-HFD mice, but tumour incidence was significantly lower in *μMT* mice (see Fig. 2). Therefore, we investigated fibrosis development in these mice as the latter could precede tumour development. In addition, we used another mouse strain termed *AIDg23s*[40] that exhibits reduced somatic hypermutation. From Sirius red, collagen IV and PDGFRβ staining on liver sections (Figs. 5A,B and Fig. S5A-C), transcriptional analyses of profibrogenic genes derived from livers of distinct mouse models (Fig. S5G) and serum hydroxyproline levels (Fig. S5H), fibrosis was solely found in WT and *AIDg23s* CD-HFD mice, but not in *JH*$^{-/-}$, *μMT*, *IgMi*, *IgA*$^{-/-}$[41] (lacking secreted IgA), *AID*$^{-/-}$[42] (lacking class switching) CD-HFD mice or in WT CD-HFD mice therapeutically treated with αCD20 antibody.

Having established a positive correlation between the presence of B cells and an intact immunoglobulin secretion function into the periphery (*e.g.*, IgA) with fibrosis (Fig. 5M and Fig. S5E,F), we sought to identify the hepatic immune cell compartment associated with NASH-related fibrosis (*e.g.*, in WT CD-HFD). Screening of several hepatic myeloid populations by flow cytometry identified CD45^{+}Ly6G^{-}CD11c^{-}F4/80^{+}CD11b^{+}Ly6C^{+} cells, classified as MoMFs,[21] in increased levels in the WT fibrotic NASH-affected mice (Fig. 5C). To determine whether MoMFs and NASH-induced fibrosis also correlate in other NASH models, we performed single-cell RNA-sequencing (scRNA-Seq) analyses of hepatic immune cell populations in also in WD and choline-deficient amino acid-specific high-fat diet (CDA-HFD)[43] models. The different NASH diets investigated represented a distinct spectrum of liver fibrosis severity (Figs. 5D and Fig. S5C). ScRNA-Seq analyses identified, among other immune cell populations, MoMFs to be associated in number and character with the degree of fibrosis (Fig. 5E,F and Fig. S5T). The MoMFs clusters 1, 3 and 6 were significantly increased in WD or CDA-HFD in the context of NASH-triggered fibrosis (Fig. 5G,H and Fig. S5U). The observed shift in the MoMF clusters depended on the diet mirroring the different degrees of fibrosis between the two diets (Fig. S5S). Notably, MoMFs – but not other immune cell populations – strongly upregulated FcR-genes and genes involved in FcR signalling activation in all NASH diets, including increased transcription of *Fcgr1,* and *Fos* genes, especially in MoMFs derived from the severe fibrotic mouse group CDA-HFD (Fig. 5I and Fig. S5U). This observation was corroborated by protein expression by FCGR1 IHC on liver sections (Fig. 5N, 5O).

FcγR activation induces macrophage phagocytosis.[44] During infection, these processes are controlled by IgA molecules surrounding infectious antigens. These complexes are recognized mainly by FcαR (CD89) in human macrophages[45] and by FcγRI (FCGR1), FcγRIIIa (FCGR3) and FcεRI (FCER1G) in mice, all having in common the intramembrane portion of FcγR for downstream signalling activation.[46] The degree of fibrosis correlated with serological IgA levels in the NASH models analysed, suggesting a link between immunoglobulin levels and Fc receptor activation. To functionally evaluate whether the absence of FcγR expression, which inhibits functional FCGR1, FCGR3 and FCER1G activity, could reduce macrophage activation and fibrosis in NASH, *FcRγ*$^{-/-}$ mice were fed a CD-HFD for 6 months. Although these mice developed full-blown NASH, steatosis, liver damage (Figs. 5J and Fig. S5I, S5J), and a similar liver inflammatory profile compared to WT controls (Fig. S5K,L), *FcRγ*$^{-/-}$ mice displayed strongly reduced fibrosis (Fig. 5K) that correlated positively with reduced serum IgA levels and the number of hepatic MoMFs (Figs. 5L and Fig. S5M). As expected, *FcRγ*$^{-/-}$ mice lacked FCRG1 expression and FcR-downstream signalling, as determined by reduced phosphorylated HCK, a downstream mediator of FcR signalling, compared to mice with fibrosis (Figs. 5N-5P).

To determine whether the observed *in vivo* phenotype in *FcRγ*$^{-/-}$ mice fed a CD-HFD relied primarily on the lack of FcRg-signalling rather than altered myeloid-cell trafficking, we evaluated the migration capability of *FcRγ*$^{+/+}$ and *FcRγ*$^{-/-}$ myeloid cells *in vivo* and *in vitro*. Bone marrow-derived macrophages (BMDMs) from *FcRγ*$^{-/-}$ and control mice, previously injected with carbon tetrachloride short-term, were analysed for their migration capacity (Fig. S5P). A CCL2 gradient induced similar transmigration efficacy of *FcRγ*$^{+/+}$ and *FcRγ*$^{-/-}$ BMDMs, as investigated by transmigration assays and subsequent flow cytometry (Fig. S5Q). In the livers of carbon tetrachloride-treated mice, hepatic MoMFs were similarly increased in both

livers from 4-month WT ND, WT CD-HFD, WT WD-HTF or CDA-HFD (n ≥4). (E) CD45^{+} cells from livers of 4-month ND, WD-HTF and CDA-HFD (all WT) fed mice were sorted and 10X single-cell RNA-seq experiments were performed (n ≥2); Representative UMAP plots visualizing single-cell RNA-sequenced CD45^{+} cells from livers of 4-month ND, WD-HTF and CDA-HFD, indicating individual cell spatial positions in blue colour among the three groups. (F) UMAP plot visualizing immune cell populations FACS-sorted by CD45^{+}. The identified immune cells population displayed are MoMFs/monocytes, KCs, DCs, neutrophils, T cells, B cells, plasma B cells, diving cells, NKT cells, and ILCs. (G) UMAP plot visualizing cell clusters of single-cell RNA-sequenced CD45^{+} cells of all mouse groups (legend reporting the number of cells in parentheses). (H) Abundance plots showing relative percentages of MoMF clusters majorly differentiated under diet-experimental conditions[1,3,6] of 4-month ND, WD-HTF and CDA-HFD mice (n ≥2). (I) Double-violin plots showing the mRNA expression of *Fcgr1* in most relevant MoMF clusters, comparing CDA-HFD or WD against ND mice (n ≥2). (J) Representative H&E staining of liver sections of 6-month WT and *FcRγ*$^{-/-}$ male mice fed with CD-HFD. (K) Representative Sirius red staining and quantification of liver sections of 6-month WT and *FcRγ*$^{-/-}$ male mice fed with CD-HFD (n = 4). (L) Quantifications of liver flow cytometric analyses of total CD45^{+}Ly6G^{-}Cd11c^{-}F4/80^{+}CD11b^{+}Ly6C^{+} cells in WT and *FcRγ*$^{-/-}$ male mice fed with CD-HFD (n = 4). (M) Correlation plot indicating serological IgA and Sirius red positivity in CD-HFD male mice (n ≥3). (N) Representative IHC images of FCGR1 staining of liver sections and (O) quantifications of FCGR1^{+} aggregates per mm^{2} (n ≥3) and phospho-HCK (per mm^{2}) (n ≥3). (P) Correlation plots indicating FCGR1^{+} aggregates per mm^{2} and Sirius red positivity, and p-HCK^{+} cells per mm^{2} and Sirius red positivity (n ≥3). (Q) Relative mRNA expression levels measured through qRT-PCR of major profibrogenic genes from 12-weeks in WT or *FcRγ*$^{-/-}$ BMDMs, after stimulation with serum of WT ND, WT CD-HFD or μMT CD-HFD (6-months under diet) (n ≥2), with or without the addition of IgA alone or in combination with Fc-blocker. Complement proteins were deactivated with a serum pre-treatment of 30 min at 56 °C. All data are presented as mean ± SEM. Statistical analyses were performed using unpaired *t* test or Pearson correlation's test. The scale bar represents 100 μm.

A

Exp. mouse group	B cells & immunoglobulins	NASH	Hepatic fibrosis	B-T cells gut interaction	HCC
WT CD-HFD	LP & SLOs, B cells, IgA, IgM, IgG	Yes	Yes	Yes	Yes (~30%)
JH$^{-/-}$ CD-HFD	No	No	No	-	No
μMT CD-HFD	only LP IgA B cells	Yes	No	-	low incidence (5%)
αCD20 WT CD-HFD	only long-lived plasma cells	No	No	-	-
IgA$^{-/-}$ CD-HFD	low afinity IgM	Yes	No	-	-
AID$^{-/-}$ CD-HFD	low afinity IgM	Yes	No	-	-
AIDg23s CD-HFD	low affinity IgM & IgA	Yes	Yes	-	-
IgMi CD-HFD	No secreted IgM & IgA, only IgG	No	No	No	-
FcRγ$^{-/-}$ CD-HFD	B cells and immunoglobulin secretion not affected	Yes	No	-	-
Germ Free (GF) CD-HFD	B cells and immunoglobulin secretion not affected	Yes	Yes	Yes	-
αCD20 GF WT CD-HFD	only long-lived plasma cells	No	No	-	-

- = Not tested

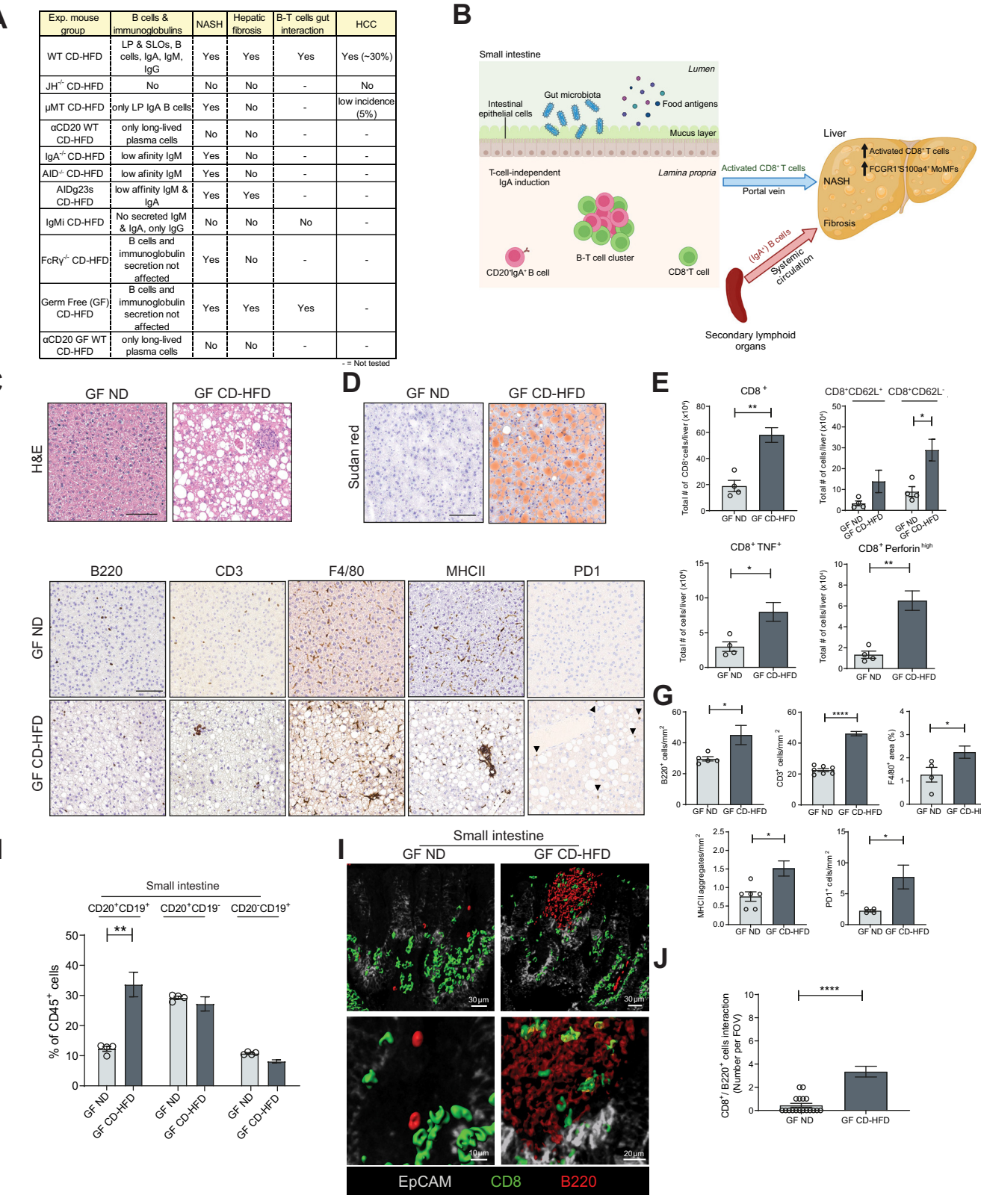

Fig. 6. Summary of models, including germ-free mice on NASH diet. (A) Table indicating NASH phenotypes, B cells/immunoglobulin types, fibrosis, B-T cell interactions and HCC in all mouse models applied in this study research. (B) Graphical summary displaying the role of lamina propria CD20$^+$IgA$^+$B cells in the context of NASH activated externally to lymphoid follicles and increased in number, forming clusters with CD8$^+$ T cells. The latter may migrate from the lamina propria to the liver via the portal vein. Secondary lymphoid organ (*e.g.*, spleen) derived IgA$^+$B cells contribute via IgA$^+$ to liver fibrosis through activation of FcRγ signalling in monocyte-derived macrophages (positive for FCGR1, S100a4, Ly6C, CD11b, F4/80). (C) Representative H&E staining of liver sections derived from GF WT ND and GF WT CD-HFD male mice fed for 6 months. (D) Representative Sudan red staining of liver sections from GF male mice (CD-HFD for 6 months). (E) Quantifications of liver flow

mouse groups compared to their untreated counterpart (Fig. S5R). Next, levels of general MoMF markers Ly6C and the profibrogenic macrophage marker S100A4 were assessed in several mouse models fed a NASH diet. Increased Ly6C$^+$ cells were found in those mice that displayed fibrosis – WT and *AIDg23s* CD-HFD mice – but not in other mouse models on CD-HFD (Fig. S5N).[47] Quantification of hepatic Ly6C$^+$/CD11b$^+$/FCER1G$^+$ cells of WT ND, and WT, *μMT*, WT αCD20, *IgMi* and *AIDg23s* mice – all on CD-HFD – showed that fibrotic livers such as WT and AIDg23s CD-HFD display a significantly higher amount of Ly6C$^+$/CD11b$^+$/FCER1G$^+$ cells (Fig. S6V,W).

A possible role for IgA and FcRγ-signalling in activating profibrogenic macrophages was investigated by measuring the expression of selected profibrogenic/activation genes such as IL-1β, IL-6 and TNF by BMDMs *ex vivo*. BMDMs from 12-week-old WT or *FcRγ*$^{-/-}$ mice were first treated *in vitro* with serum derived from healthy WT ND or fibrotic WT CD-HFD mice (both 6 months on diet) (Fig. S5O). Serum from fibrotic WT CD-HFD induced increased expression of the profibrogenic genes compared to ND serum (Fig. 5Q). WT-BMDMs treated with serum from μMT CD-HFD mice, which have NASH but are devoid of systemic IgA secretion and fibrosis, failed to induce profibrogenic/activation genes (Fig. 5Q). In contrast, the addition of purified IgA added to serum derived from WT ND or *μMT* CD-HFD mice strongly induced the expression of IL-6, IL-1β and TNF in BMDMs, which was abrogated by addition of an Fc-blocker (Fig. 5Q). Strikingly, the addition of Fc-blocker to serum derived from fibrotic WT CD-HFD mice prevented the induction of IL-6, IL-1β and TNF in BMDMs (Fig. 5Q). These data indicate that immunoglobulins (*e.g.*, IgA) circulating in serum from NASH mice may directly trigger BMDM-activation. As an additional control, *FcRγ*$^{-/-}$-BMDMs were treated with the serum of fibrotic CD-HFD mice, which failed to induce the expression of IL-6, IL-1β and TNF in BMBMs, again highlighting that FcRγ-signalling is involved in immunoglobulin-mediated transduction processes (Fig. 5Q).

Overall, these data indicate that FcRγ-signalling, mainly in MoMFs, plays an important role in the development of hepatic fibrosis in NASH and that secreted immunoglobulin is a critical factor in activating this signalling.

Fig. 6A summarizes the most important data presented so far. We propose that B cells can act via two mechanisms: (i) an extrafollicular, intestinal mechanism that can promote activation and transmigration of T cells in the liver and (ii) a mechanism involving the secretion of immunoglobulins, most likely IgA, that can drive the activation of MoMFs in the liver and promote the initiation of fibrosis (Fig. 6B).

The gut microbiota is not necessary for NASH development

The gut microbiota has an important role in the homeostasis of gut B cells.[48,49] So far, studies have suggested that germ-free (GF) mice were resistant to obesity[50] depending on the type of diet,[51,52] and NAFLD/NASH development.[53–55] However, GF mice fed a WD for 16 weeks developed obesity and demonstrated metabolic dysfunction,[56] indicating that the absence of microbiota might allow for the development of metabolic syndrome.

To investigate this concept in the context of NASH and the related B-cell functions, GF mice were fed a CD-HFD for 6 months. CD-HFD mice gained significant weight (Fig. S6A) and displayed full-blown NASH and impaired glucose response (Fig. 6C,D and Fig. S6A,B,G), more hepatic T cells, B cells and activated CD8$^+$ T cells expressing TNF and Perforin (Fig. 6E), and F4/80$^+$ cells and MHC-II$^+$ aggregates (Fig. 6F,G). In the small intestine, CD-HFD mice presented increased B-cell frequencies (Fig. 6H), and also showed B220$^+$/CD8$^+$ cells forming clusters (yellow), especially along intestinal villi (Fig. 6I,J).

The importance of B cells for NASH development under GF conditions was tested by administering an αCD20 antibody for 6 weeks, starting at month 4 on CD-HFD – a time-point by which mice on a CD-HFD have already developed NASH and liver damage (Fig. S6D,E). B-cell depletion efficacy was proven effective in different tissues (spleen, liver and small intestine) (Fig. S6K).

Anti-CD20 antibody-treated GF CD-HFD mice were obese and rescued for NASH but not for steatosis and showed unchanged serum ALT and cholesterol levels (Figs. S6G-J). Furthermore, αCD20 antibody-treated GF CD-HFD livers were not inflamed and showed significantly fewer activated CD8$^+$ T and F4/80$^+$ cells (Fig. S6K,L), whereas MHC-II$^+$ aggregates remained on the same levels compared to untreated controls (Fig. S6L).

These data suggest that the gut microbiota was not necessary to induce obesity and NASH, proposing a sterile metabolic activation of immune cells to be sufficient to drive NASH(3, 4, 29). Moreover, B cells could act independently of the gut microbiota to contribute to NASH development and interact with the T cells in the small intestine.

Increased gastrointestinal CD20$^+$ B cells, high IgA levels and FcRγ$^+$ myeloid cells in patients with NASH and cirrhosis

Next, we compared the data obtained from our mouse NASH models in patients with NASH. Similar to our mouse NASH models, an increase of CD20$^+$ B cells was found in gastrointestinal tissue (*e.g.*, jejunum) taken during bariatric surgery from patients with NASH when compared to patients with simple steatosis (Fig. 7A,B). Moreover, we found increased phosphorylated SYK$^+$ in jejunal immune cells (including CD20$^+$ B cells) of patients with NASH *vs*. simple steatosis (Fig. 7C, and Fig. S7A,J), indicative of B-cell activation.

We could corroborate previously published data demonstrating elevated serum IgA levels positively correlating with the degree of fibrosis in two distinct patient cohorts (Fig. 7D,E and Fig. S2B).[22] Moreover, increased levels of IgA significantly correlated with the presence of portal inflammation (Fig. 7F,G).

cytometric analyses comparing 6-month GF ND, and GF CD-HFD for total CD8$^+$ cells, CD8$^+$CD62L$^+$ and CD8$^+$CD62L$^-$ cells, CD8$^+$TNF$^+$ cells, and CD8$^+$perforin^{high} cells (n = 4). (F) Representative IHC images of liver sections and (G) quantifications per mm^2 for B220, CD3, F4/80 and MHC-II staining of GF ND and GF CD-HFD mice (n = 5). (H) Quantifications of small intestine flow cytometric analyses of CD20$^+$CD19$^+$, CD20$^+$CD19$^-$ and CD20$^-$CD19$^+$ cells in GF male mice (n = 4). (I) Representative high-resolution confocal microscopy and 3D reconstruction images of small intestine lamina propria staining for B220+ and CD8+ cells (yellow areas indicate a point of contact among B220+ and CD8+ cells), and (J) quantification of clusters of B220+/CD8+ interacting cells, of GF male mice (n = 3, with n ≥4 FOV each mouse). All data are presented as mean ± SEM. Statistical analyses were performed using unpaired *t* test. The scale bar represents 100 μm.

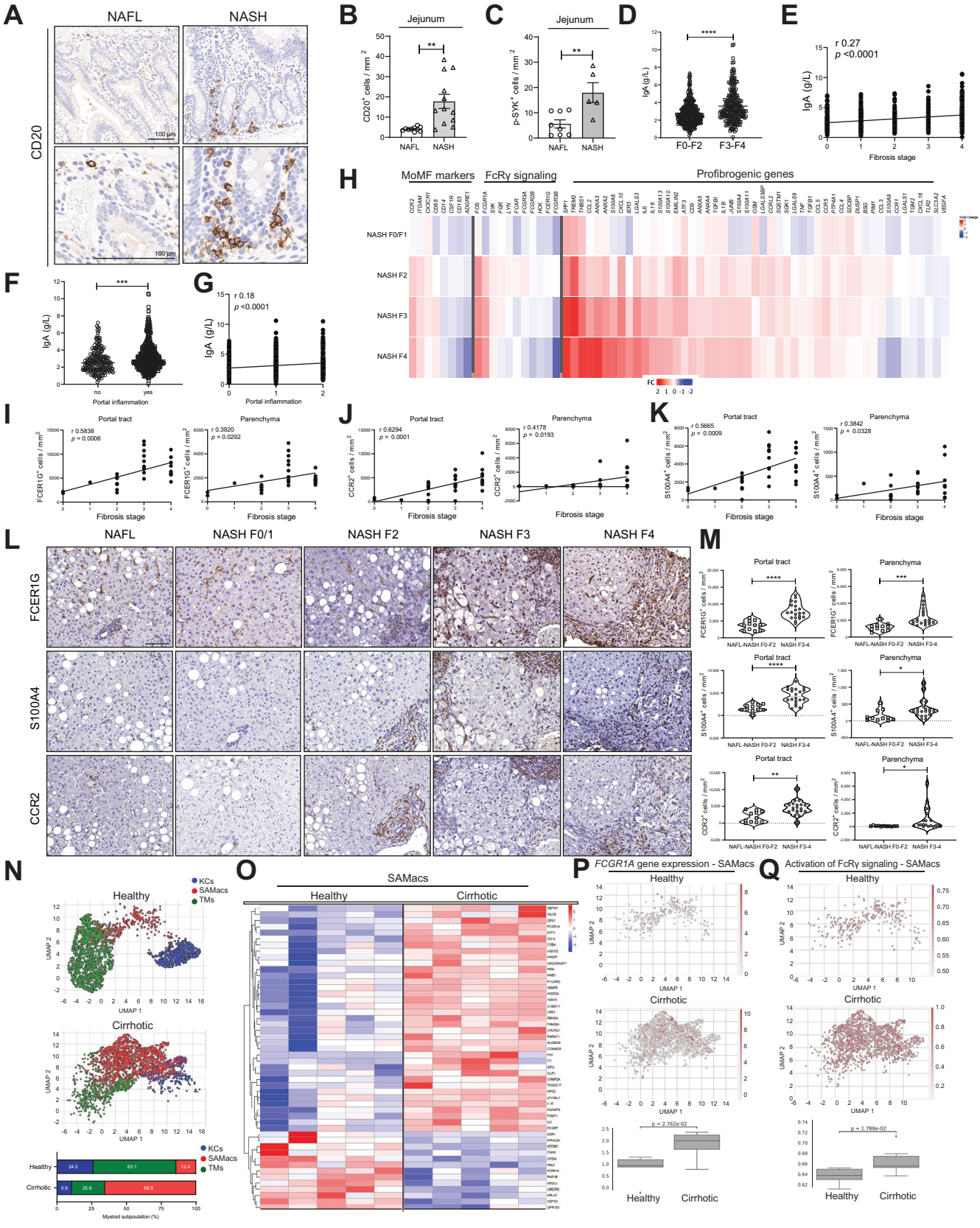

Fig. 7. Intestinal B cells and hepatic myeloid cells in NAFLD-affected patients. (A) Representative CD20 stained jejunum samples of NAFL and NASH-affected patients. (B) CD20^{+} cells quantification in jejuna of patients with NAFL, and NASH, per mm^{2} (n ≥4). (C) Phospho-SYK quantification on immune cells (B cells or myeloid cells) in jejuna on patients with NAFL or NASH (n ≥5). (D) Serum measurement of IgA levels in patients with NAFLD divided into two subgroups (F0–F2 and F3–F4) based on fibrosis score (Brunt/Kleiner scoring) (n ≥233 each group, total n = 639). (E) Correlation plot of IgA serological levels and fibrosis stage in NAFLD patient

Notably, IgG but not IgM levels were elevated in higher fibrosis stages (Fig. S7B). Interestingly, patients with NAFLD and rheumatoid arthritis – treated with a monoclonal αCD20 antibody – displayed reduced serum ALT levels (Fig. S7E), supporting the notion that B-cell depletion might ameliorate liver damage in patients with NASH. High levels of serum IgA were associated with parenchymal and portal tract $PD1^+$ cells but not with $CD8^+$ T cells in patients with NASH, indicating a possible link between IgA secretion, fibrosis, and $PD1^+$ cells (Fig. S7F,G).

Our mouse data presented above suggested that MoMFs correlated strongly with fibrogenesis.[57,58] In a large NAFLD cohort of patients with different degrees of fibrosis, we performed a total liver transcriptomic analysis of selected genes for MoMFs, FcRγ signalling and fibrogenesis. We found that many relevant genes of these categories, including *CCR2*, *ITGAM*, *CX_3CR1* (indicative of MoMFs phenotype), *FOS* and *FCGR1A* (FcRγ-signalling), *SPP1*, *TREM2*, *THBS1*, *CCL2*, and S100A4 among other profibrogenic genes were directly correlated with the degree of fibrosis (Fig. 7H), similar to our mouse analysis. We also found a strong correlation between the chemokine receptor *CCR2* and *S100A* with *FCER1G* at a transcriptomic level (Fig. S7H).

In human NAFLD livers, the number of $FCER1G^+$, $CCR2^+$ and $S100A4^+$ cells in the portal tract and parenchyma correlated with the degree of fibrosis (Fig. 7I-7K). Mainly, fibrotic areas were densely populated with infiltrating $S100A4^+FCER1G^+CCR2^+$ cells and stratification of patients with NAFLD based on the fibrosis stage showed a significant increase in advanced NAFLD (Fig. 7L,M, and S7H,I). In contrast, no difference was observed in the density of $CD163^+FCER1G^+$ cells among different fibrotic stages, indicating a marginal role of Kupffer cells in fibrosis (data not shown).

Further, we analysed whether myeloid-cell populations driving fibrosis and/or cirrhosis would be activated by similar pathways to those identified in our mouse NASH models. ScRNA-Seq analysis of $CD45^+$ cells derived from healthy liver tissue (transplantation donors) and NAFLD-cirrhotic livers showed that patients with cirrhosis displayed an increased compartment of a subpopulation of myeloid cells called scar-associated macrophages (SAMs) (Fig. 7N,O and S7K).[59] Notably, we found that *FCGR1A* gene expression was significantly increased in patients with cirrhosis compared with healthy donors (Fig. 7P) and that the FcRγ-signalling signature was significantly increased in patients with cirrhosis compared with healthy donors, being particularly enriched in the SAM compartment (Fig. 7Q). Transcriptional analyses and comparison of FcRγ-signalling pathways in mouse and human NASH livers revealed close similarities in the regulation of the FcRγ-signalling components as well as downstream targets (Fig. S7L).

In summary, data from patients with NASH suggest an important role for secreted IgA and FcRγ-signalling on MoMFs/SAMs in the development of fibrosis and/or cirrhosis, in agreement with the data derived from NASH mouse models.

Discussion

Herein, we describe two distinct B cell-dependent mechanisms that promote (i) metabolic T-cell activation in the gastrointestinal tract and (ii) aggravate liver fibrosis in NASH (Fig. 6A,B). We have previously shown that auto-aggressive T cells exacerbate progressive liver disease in NASH, leading to HCC development.[3,4] We report that T-cell activation, hepatic inflammation, NASH, fibrosis and liver tumorigenesis were abrogated *in vivo* by genetic depletion of B cells ($JH^{-/-}$ mice). Therapeutic depletion of B cells in mice with NASH/fibrosis led to a reduction/reversal of T-cell-driven inflammation and fibrosis. ^{1}H-NMR and mass-spectrometry analyses demonstrated that B cells contribute to hepatic metabolic alterations that characterise NASH pathophysiology.

As the gut-liver axis has been identified as a critical factor in NAFLD pathophysiology,[14] we assessed the role of gastrointestinal B cells (*μMT* mice). This assessment revealed that gastrointestinal IgA^+ B cells contribute to T cell–driven inflammation and metabolic alterations in the liver but cannot drive fibrosis owing to their inability to secrete immunoglobulins into the periphery. These gastrointestinal B cells developed in the lamina propria in a T cell-independent manner,[60] albeit at low numbers, were strongly activated in the context of NASH. NASH-driven HCC incidence was significantly lower in *μMT* mice despite exhibiting equivalent quality and levels of NASH compared to WT CD-HFD, potentially attributable to the absence of hepatic fibrosis in *μMT* CD-HFD mice. Therapeutic depletion of gastrointestinal B cells in *μMT* mice reduced T-cell inflammation *in vivo* and reverted NASH.

Further analysis in WT mice on a NASH diet showed that gastrointestinal B cells were elevated in number, metabolically activated and displayed activated BCR signalling. When we analysed human intestinal tissue from patients with NASH, we also observed an increase in B-cell number compared to unaffected patients or patients with simple steatosis.

In the lamina propria of the small intestine of NASH mice, B cells and $CD8^+$ T cells formed clusters with cell-cell interactions, suggesting that within these clusters, B cells could activate $CD8^+$ T cells. However, these clusters were not found

cohort of 639 individuals. (F) Serum measurement of IgA levels in patients with NAFLD divided into two subgroups based on the absence or presence of liver portal inflammation (n ≥233 each group, total n = 639). (G) Correlation plot of IgA serological levels and portal inflammation scores in the NAFLD patient cohort of 639 individuals. (H) Heatmaps showing transcriptomics analysis derived $\log_2$ fold-change values of selected genes involved in the monocyte-derived macrophage phenotype, in FcRγ signalling and in fibrogenesis, from patients with NAFLD and with different degrees of fibrosis *vs.* patients with NAFL (total n = 206). (I–K) Correlation plots of fibrosis stage and portal tract or parenchymal (I) $FCER1G^+$ cells/mm^2, (J) $CCR2^+$ cells/mm^2, or (K) $S10014^+$ cells/mm^2 (n = 31). (L) IHC representative images of FCER1G, CCR2 and S100A4 in patients with NAFLD, with absent/very low fibrosis (F0/F1) and high fibrosis (F3), and their quantifications (M) in two fibrosis subgroups for portal and parenchymal quantified stained cells (n ≥11). (N) UMAP plots indicating liver $CD45^+$ FACS-sorted cells and subsequently single-cell 10X RNA-sequenced, divided into TMs, KCs, and SAMs, from healthy donors and patients with NAFLD-related cirrhosis, and percentages of each myeloid subpopulation below (n ≥5). (O) Heatmaps indicating the top 100 most variable genes among healthy donors and patients with cirrhosis in SAMac population (n = 5). (P) UMAP plots indicating mRNA expression scores of *FCGR1A* gene in SAMs from healthy donors and patients with NAFLD and cirrhosis, with statistical analysis below (n ≥5). (Q) Expression scores of activated FcRγ signature (Reactome) in healthy donor livers and in NAFLD/ALD-cirrhotic SAM population, with statistical analysis below (n ≥5). All data are presented as mean ± SEM. Statistical analyses were performed using unpaired *t* test or Pearson correlation's test.. The scale bar for IHC represents 100 μm, for immunofluorescence 50 μm.

in ND-fed mice. Our data indicate that hyperactivation of $CD8^+$ T cells by the gastrointestinal B cells in NASH is achieved via a licensing step that requires direct cell-cell interaction.

Importantly, we could demonstrate that B cells derived from small intestines of NASH mice can directly activate $CD8^+$ T cells *ex vivo* in an antigen-specific independent manner, necessitating LFA-1 and ICAM-1 but not MHC-I. In contrast, intestinal B cells from ND-fed mice could not activate T cells *ex vivo*. Our data indicate that auto-aggression and hyperactivation of $CD8^+$ T cells via the gastrointestinal B cells in NASH is achieved by a licensing step that requires direct cell-cell interaction. Interference with the LFA1-ICAM axis abrogated T-cell hyperactivation *ex vivo*. Moreover, activation of $CD8^+$ T cells was TCR-independent – as gastrointestinal B cells also activated OT1-CD8+ T cells. Interaction of $CD8^+$ T cells with the gastrointestinal B cells acts as an amplifier of downstream TCR signalling without the involvement of antigen-specific presentation by B cells, as blockade of MHC-I did not prevent B cell-induced auto-aggression.

Besides metabolic re-programming, activated NASH gastrointestinal B cells or amplified BCR signalling are potentially represented by phosphorylation of SYK[61-64]. The latter was absent in the B cells of IgMi mice, which are protected from NASH and lack B-T cell clusters in the small intestine. Notably, in hyperactivated B cells, as in the case of lymphoma, SYK inhibitors are exploited therapeutically.[65]

Using Kaede mice and their capability to photoactivate cells locally, we enabled tracking of B and T cells from the gastrointestinal tract to the liver in the context of NASH. We suggest that metabolically activated gastrointestinal B and T cells migrate from the gut to the liver, indicating that metabolically activated T cells may originate in the small intestine, migrate to and potentially be maintained in the liver.

Given the central role of gastrointestinal B cells in NASH development, we proceeded to study the role of microbiota[15–17] in our disease models. We showed that NASH development occurred without the gut microbiota in a NASH diet model (CD-HFD). Therapeutic depletion of B cells in GF mice with NASH reversed liver inflammation and fibrosis, indicating that B cells lead to T-cell activation and NASH - independently of the gut microbiota.

It has been shown that serum IgA levels were elevated in patients with NAFLD(22). Our *in vivo* and *in vitro* NASH studies demonstrated that secretion of IgA contributed to fibrosis by activating FcRγ-signalling in $CD11b^+CCR2^+F4/80^+CD11c^-FCGR1^+$ MoMFs.[66] However, we cannot exclude that other cell types expressing Fc receptors (*e.g.*, hepatocytes) may also contribute to this phenotype. Notably, in molecular analysis of patients with NASH, serum IgA levels correlated with fibrosis severity and with FcRγ-activated SAMs in the liver.

Thus, besides other known immune cell mechanisms that drive NASH and fibrosis,[67] B cells and IgA secretion are clearly important players in the pathogenesis of NAFLD/fibrosis/cirrhosis. It will be interesting to decipher further the role of B cells in hepatic lipid accumulation and metabolic dysregulation. New therapeutic approaches in NASH suggest combination therapies with anti-steatosis, anti-inflammatory, and anti-fibrotic drugs may be effective.[68]

Our study shows that gastrointestinal B cells are a potential target for such a combinatorial therapeutic approach, as we have identified them as mediators of licensing metabolic T-cell activation and fibrosis. Future studies blocking the interaction between B and T cells, specifically in the gut, and targeting FcR signalling in the liver, might illuminate new therapeutic avenues against NASH and NASH-related fibrosis.

Affiliations

[1]Division of Chronic Inflammation and Cancer, German Cancer Research Center Heidelberg (DKFZ), Heidelberg, Germany; [2]Research Unit of Radiation Cytogenetics (ZYTO), Helmholtz Zentrum München, Neuherberg, Germany; [3]Institute of Molecular Oncology and Functional Genomics, Clinic and Polyclinic for Internal Medicine II, Klinikum rechts der Isar of the Technical University of Munich (TUM), Munich, Germany; [4]Translational and Clinical Research Institute, Faculty of Medical Sciences, Newcastle University, Newcastle, UK; [5]Maurice Müller Laboratories (DBMR), University Department of Visceral Surgery and Medicine Inselspital, University of Bern, Bern, Switzerland; [6]Institute of Molecular Medicine and Experimental Immunology, University Hospital, Bonn, Germany; [7]Nutrition and Immunology, Technical University of Munich, Freising-Weihenstephan, Germany; [8]ZIEL - Institute for Food and Health, Technical University of Munich, Freising-Weihenstephan, Germany; [9]Department of Hepatology and Gastroenterology, Charité Universitätsmedizin Berlin, Campus Virchow-Klinikum and Campus Charité Mitte, Berlin, Germany; [10]Division of Vascular Oncology and Metastasis, German Cancer Research Center Heidelberg (DKFZ-ZMBH Alliance), Heidelberg, Germany; [11]European Center of Angioscience (ECAS), Medical Faculty Mannheim, Heidelberg University, Mannheim, Germany; [12]Department of Preclinical Imaging and Radiopharmacy, Werner Siemens Imaging Center (WSIC), Tübingen University, Tübingen, Germany; [13]The Concern Foundation Laboratories at the Lautenberg Center for Immunology and Cancer Research, IMRIC, Faculty of Medicine, Hebrew University-Hadassah Medical School, Jerusalem, Israel; [14]Internal Medicine I, University Hospital Tübingen, Faculty of Medicine, University of Tübingen, Tübingen, Germany; [15]Department of Computer Science, University of Tübingen, Tübingen, Germany; [16]Section of Molecular Immunology und Gastroenterology, I. Department of Medicine, University Medical Center Hamburg-Eppendorf, Hamburg, Germany; [17]Department of Medicine II, University Hospital Freiburg - Faculty of Medicine, University of Freiburg, Freiburg, Germany; [18]Center for Translational Cancer Research (TranslaTUM), Technical University of Munich (TUM), Munich, Germany; [19]Department of General, Visceral and Transplantation Surgery, University of Heidelberg, Heidelberg, Germany; [20]Research Center for Immunotherapy (FZI), University Medical Center at the Johannes Gutenberg University, Mainz, Germany; [21]Institute for Molecular Medicine, University Medical Center of the Johannes Gutenberg University, Mainz, Germany; [22]Division of Hepatology, University-Hospital Würzburg, Würzburg, Germany; [23]Rheumatology/Clinical Immunology, Kreiskliniken Altötting-Burghausen, Burghausen, Germany; [24]Rheumatology, Medical Clinic II, Julius-Maximilians-University Würzburg, Germany; [25]Centre for Inflammation Research, The Queen's Medical Research Institute, University of Edinburgh, Edinburgh, UK; [26]MRC Human Genetics Unit, Institute of Genetics and Molecular Medicine, University of Edinburgh, Edinburgh, UK; [27]Department of Immunobiology, Yale University School of Medicine, New Haven, USA; [28]Institute of Pathology, Technical University of Munich (TUM), Munich, Germany; [29]Comparative Experimental Pathology, Technical University of Munich (TUM), Munich, Germany; [30]Division of Chromatin Networks, German Cancer Research Center (DKFZ) and Bioquant, Heidelberg, Germany; [31]Department of Pathology and Molecular Pathology, University and University Hospital Zurich, Zurich, Switzerland; [32]Department Internal Medicine I, Eberhard-Karls University, Tübingen, Germany; [33]Department of Gastroenterology, Hepatology and Infectious Diseases, University Hospital Duesseldorf, Medical Faculty, Heinrich Heine University, Duesseldorf, Germany; [34]Institute of Molecular Medicine, RWTH Aachen University, Aachen, Germany; [35]Institute of Molecular Immunology and Experimental Oncology, Klinikum rechts der Isar, Technical University of Munich, Munich, Germany; [36]Immunology Department, Weizmann Institute of Science, Rehovot, Israel; [37]Cancer-Microbiome Research Division, DKFZ, Heidelberg, Germany; [38]Newcastle NIHR Biomedical Research Center, Newcastle upon Tyne Hospitals NHS Trust, Newcastle upon Tyne, United Kingdom; [39]Emmy Noether Research Group Epigenetic Machineries and Cancer, Division

of Chronic Inflammation and Cancer, German Cancer Research Center (DKFZ), Heidelberg, Germany; [40]School of Biomedical, Nutrition and Sports Sciences, Faculty of Medical Sciences, Newcastle University, Newcastle upon Tyne, UK; [41]Faculty of Biosciences, Heidelberg University, Heidelberg, Germany; [42]North Park University, Chicago, IL, USA; [43]Translational Pancreatic Cancer Research Center, Clinic and Polyclinic for Internal Medicine II, Klinikum rechts der Isar of the Technical University of Munich (TUM), Munich, Germany; [44]M3 Research Institute, Eberhard Karls University Tübingen, Tübingen, Germany

Abbreviations

AID, activation-induced cytidine deaminase; ALT, alanine aminotransferase; BCR, B cell receptor; BMDMs, bone marrow-derived macrophages; CCL2, chemokine (C–C motif) ligand 2; CCl_4, carbon tetrachloride; CCR2, C–C motif chemokine receptor 2; CDA-HFD, choline-deficient amino acid-specific high-fat diet; CD-HFD, choline-deficient high-fat diet; CTLA4, cytotoxic T-lymphocyte associated protein 4; CXCR4/6, C-X-C motif chemokine receptor 4/6; FCER1G, Fc epsilon receptor Ig; FCGR1, Fc-gamma receptor 1; GF, germ-free; HCC, hepatocellular carcinoma; 1H-NMR, proton-nuclear magnetic resonance; ICAM-1, intercellular adhesion molecule 1; IHC, immunohistochemistry; IL-, interleukin-; LFA-1, Lymphocyte function-associated antigen 1; mAb, monoclonal antibody; MHC-I/II, major histocompatibility complex, class I/II; MoMFs, monocyte-derived macrophages; NAFLD, non-alcoholic fatty liver disease; NAS, NAFLD activity score; NASH, non-alcoholic steatohepatitis; ND, normal diet; PD1, programmed cell death protein 1; PDGFRβ, platelet-derived growth factor receptor beta; SAMs, scar-associated macrophages; ScRNA-Seq, single-cell RNA-sequencing; TCR, T-cell receptor; TNF, tumour necrosis factor; t-SNE, t-distributed stochastic neighbour embedding; WD, western diet; WT, wild-type.

Financial support

M.H. was supported by an European Research Council (ERC) Consolidator grant (HepatoMetaboPath), SFBTR179 project ID 272983813, SFB/TR 209 project ID 314905040, SFBTR1335 project ID 360372040, SFB 1479 (Project ID: 441891347), the Wilhelm Sander-Stiftung, the Rainer Hoenig Stiftung, a Horizon 2020 grant (Hep-Car), Research Foundation Flanders (FWO) under grant 30826052 (EOS Convention MODEL-IDI), Deutsche Krebshilfe projects 70113166 and 70113167, German-Israeli Cooperation in Cancer Research (DKFZ-MOST) and the Helmholtz-Gemeinschaft, Zukunftsthema 'Immunology and Inflammation' (ZT-0027). M.H. was also supported together with A.W. by seed funding from HI-TRON. E.K. was supported by the GRK 1482. V.L. was financed by Horizon 2020 grant (Hep-Car), and ERC-CoG (HepatoMetaboPath). D.P. & E.K. were supported by the Helmholtz Future topic Inflammation and Immunology. S.S. was supported by the German-Israeli Helmholtz International Research School: Cancer-TRAX (HIRS-0003), a grant from the Helmholtz Association's Initiative and Networking Fund. Q.M.A. and OG are supported by the LITMUS (Liver Investigation: Testing Marker Utility in Steatohepatitis) project which has received funding from the Innovative Medicines Initiative (IMI2) Program of the European Union under Grant Agreement 777377; this Joint Undertaking receives support from the European Union's Horizon 2020 research and innovation programme and EFPIA. QMA is also supported by the Newcastle NIHR Biomedical Research Centre. N.C.H. is supported by a Wellcome Trust Senior Research Fellowship in Clinical Science (ref. 219542/Z/19/Z). A.W. was funded by the DFG via CRC 1292. Z.A. was funded by the DFG under Germany's Excellence Strategy (EXC 2151) 390873048, SFB1454, SFBTR237 and the GRK 2168. A.D.G was supported by European Respiratory Society/short term fellowship (to A.D.G), Else Kröner Memorial Stipendium (to A.D.G), Werner Otto Stiftung (to A.D.G), Erich und Gertrud Roggenbuck Stiftung (to A.D.G), Hamburger Krebsgesellschaft Stiftung (to A.D.G). E.E. is a scientific cofounder of DayTwo and BiomX, and an advisor to Hello Inside, Igen, and Aposense in topics unrelated to this work.

Conflict of interest

E.K. is employed by Springer Nature; M.J.W. is employed by Roche Diagnostics GmbH;D.P. is employed by Novo Nordisk. The authors declare no conflicts of interest that pertain to this work.

Please refer to the accompanying ICMJE disclosure forms for further details.

Authors' contributions

E.K & V.L. wrote the manuscript, experimental conception & work; S.S. experimental work *in vivo*; O.G. experimental work, histological analysis of human tissue; H.L. experimental work mice & microbiome analysis; M.J.W. experimental work *in vivo*; H.H. experimental work; S.B. experimental work with germ-free mice; J.H. experimental work *in vivo* & analysis of immune cells; D.I. 3D imaging of histological slides; L.Z. metabolomic analysis; A.S–P. analysis of immune cells &; single-cell analysis; R.G. bioinformatic single-cell analysis of mouse data; T.OC. experimental work in mice & provided support with writing the manuscript; A.G. experimental work with Kaede mice & provision of samples; A.S. experimental work & provision of samples; Y.S. bioinformatic single-cell analysis of mouse data; M.G.B. experimental work *in vivo* & flow cytometry analysis; C.R. t-SNE immune cell analysis; D.P. experimental work *in vivo* & flow cytometry analysis; R.O. bioinformatic analysis & experimental work; P.R. experimental work *in vivo* & flow cytometry analysis; M.R. experimental work *in vivo* & flow cytometry analysis; N.R. surgical expertise & provision of human samples; M.E.H. experimental work *in vivo*; M.F. experimental work *in vivo*; N.Y. experimental work *in vivo*; J.J. experimental work *in vivo*; I.S. experimental work *in vivo*; C.F. experimental work *in vivo* & flow cytometry analysis; R.M. experimental work & provision of samples; M.F. experimental work & provision of samples; S.J.W. experimental work flow cytometry analysis; S.C. experimental work & transcriptomic analysis of human samples; J. W–K. transcriptomic analysis of human samples; P.R. transcriptomic analysis of human samples; C.K. histological analysis of mouse samples; T.K. experimental work *in vivo* & flow cytometry analysis; A.L.L. experimental work; S.K. experimental work *in vivo* & flow cytometry analysis; P.S.B. microbiome analysis; K.S. provided support in histological analysis; M.H. provided support with t-SNE immune cell analysis; K.R. bioinformatic analysis; H.Z. provided support with bioinformatic analysis; A.W. experimental work; N.M. experimental work *in vivo*; T.L. conceptual input & provision of samples; M.V. experimental work *in vivo* & provision of samples; H.A. experimental work; R.F. conceptual input, microbiome and IgA analysis; O.P. experimental work *in vivo*; R.R. experimental work *in vivo*; N.H. experimental work *in vivo* & flow cytometry; S.H. experimental work *in vivo*; A.M. provided support with experimental work *in vivo*; P.C. conceptual input & provided support with experimental work *in vivo*; M.C. bioinformatic analysis; A.G. provided human samples; C.T. metabolomic analysis; E.E. conceptual input & bioinformatic analysis; A.E. conceptual input, provision of mice, experimental work *in vivo* & in vitro; Z.A. conceptual input, provision of mice, experimental work *in vivo* & in vitro; D.H. conceptual input, provision of germ-free mice, experimental work *in vivo*; F.T. conceptual input, analysis of myeloid cells, support with experimental work *in vivo*; Q.A. experimental work with human tissues and serum samples & provision of human NASH cohort; M.H. conceptual support & input, wrote the manuscript with E.K. & V.L. and supervised this study.

Data availability statement

The accession number for the bulk RNA-sequencing of sorted intestinal murine CD20+ and CD19+ cells reported in this paper is GSE190691. Data of scRNA-Seq for murine liver and intestine analyses are submitted under GSE131834 and GSE190204, respectively. The accession numbers for human scRNA-Seq sequencing are GSE136103, GSE190487 and GSM5724573. Further information and requests for resources and reagents should be directed to and will be fulfilled by the Lead Contact, Prof. M. Heikenwälder.

Acknowledgements

We thank Danijela Heide, Florian Müller, Enrico Focaccia, Mohammad Ahmed, Sabrina Schumacher, Jenny Hetzer, Corinna Leuchtenberger, Tim Machauer for excellent technical help. Moreover, we are very thankful for the support executed by the Comparative Experimental Pathology laboratory of the Technical University of Munich (TUM). A.W. was funded by the Deutsche Forschungsgemeinschaft DFG via CRC 1292. Z.A. was funded by the DFG under Germany's Excellence Strategy (EXC 2151) 390873048, SFB1454, SFBTR237 and the GRK 2168.

Supplementary data

Supplementary data to this article can be found online at https://doi.org/10.1016/j.jhep.2023.04.037.

References

Author names in bold designate shared co-first authorship

[1] Huang DQ, El-Serag HB, Loomba R. Global epidemiology of NAFLD-related HCC: trends, predictions, risk factors and prevention. Nat Rev Gastroenterol Hepatol 2021;18(4):223–238.

[2] **Anstee QM**, **Reeves HL**, **Kotsiliti E**, Govaere O, Heikenwalder M. From NASH to HCC: current concepts and future challenges. Nat Rev Gastroenterol Hepatol 2019;16(7):411–428.

[3] Pfister D, Núñez NG, Pinyol R, Govaere O, Pinter M, Szydlowska M, et al. NASH limits anti-tumour surveillance in immunotherapy-treated HCC. Nature 2021;592(7854):450–456.
[4] Dudek M, Pfister D, Donakonda S, Filpe P, Schneider A, Laschinger M, et al. Auto-aggressive CXCR6. Nature 2021;592(7854):444–449.
[5] Ringelhan M, Pfister D, O'Connor T, Pikarsky E, Heikenwalder M. The immunology of hepatocellular carcinoma. Nat Immunol 2018;19(3):222–232.
[6] W.H.O. Cancer: key facts. 2020. https://www.who.int/news-room/fact-sheets/detail/cancer.
[7] Llovet JM, Kelley RK, Villanueva A, Singal AG, Pikarsky E, Roayaie S, et al. Hepatocellular carcinoma. Nat Rev Dis Primers 2021;7(1):6.
[8] Schulz M, Tacke F. Identifying high-risk NASH patients: what we know so far. Hepat Med 2020;12:125–138.
[9] Sanyal AJ, Van Natta ML, Clark J, Neuschwander-Tetri BA, Diehl A, Dasarathy S, et al. Prospective study of outcomes in adults with nonalcoholic fatty liver disease. N Engl J Med 2021;385(17):1559–1569.
[10] Piscaglia F, Svegliati-Baroni G, Barchetti A, Pecorelli A, Marinelli S, Tiribelli C, et al. Clinical patterns of hepatocellular carcinoma in nonalcoholic fatty liver disease: a multicenter prospective study. Hepatology 2016;63(3):827–838.
[11] Aby E, Phan J, Truong E, Grotts J, Saab S. Inadequate hepatocellular carcinoma screening in patients with nonalcoholic steatohepatitis cirrhosis. J Clin Gastroenterol 2019;53(2):142–146.
[12] O'Hara J, Finnegan A, Dhillon H, Ruiz-Casas L, Pedra G, Franks B, et al. Cost of non-alcoholic steatohepatitis in Europe and the USA: the GAIN study. JHEP Rep 2020;2(5):100142.
[13] Lazarus JV, Mark HE, Anstee QM, Arab JP, Batterham RL, Castera L, et al. Advancing the global public health agenda for NAFLD: a consensus statement. Nat Rev Gastroenterol Hepatol 2021;19(1):60–78.
[14] De Munck TJI, Xu P, Verwijs HJA, Masclee AAM, Jonkers D, Verbeek J, et al. Intestinal permeability in human nonalcoholic fatty liver disease: a systematic review and meta-analysis. Liver Int 2020;40(12):2906–2916.
[15] Le Roy T, Llopis M, Lepage P, Bruneau A, Rabot S, Bevilacqua C, et al. Intestinal microbiota determines development of non-alcoholic fatty liver disease in mice. Gut 2013;62(12):1787–1794.
[16] **Henao-Mejia J**, **Elinav E**, **Jin C**, Hao L, Mehal WZ, Strowig T, et al. Inflammasome-mediated dysbiosis regulates progression of NAFLD and obesity. Nature 2012;482(7384):179–185.
[17] De Minicis S, Rychlicki C, Agostinelli L, Saccomanno S, Candelaresi C, Trozzi L, et al. Dysbiosis contributes to fibrogenesis in the course of chronic liver injury in mice. Hepatology 2014;59(5):1738–1749.
[18] Yoshimoto S, Loo TM, Atarashi K, Kanda H, Sato S, Oyadomari S, et al. Obesity-induced gut microbial metabolite promotes liver cancer through senescence secretome. Nature 2013;499(7456):97–101.
[19] Kubes P, Mehal WZ. Sterile inflammation in the liver. Gastroenterology 2012;143(5):1158–1172.
[20] **Malehmir M**, **Pfister D**, **Gallage S**, **Szydlowska M**, **Inverso D**, Kotsiliti E, et al. Platelet GPIbα is a mediator and potential interventional target for NASH and subsequent liver cancer. Nat Med 2019;25(4):641–655.
[21] **Wen Y**, **Lambrecht J**, Ju C, Tacke F. Hepatic macrophages in liver homeostasis and diseases-diversity, plasticity and therapeutic opportunities. Cell Mol Immunol 2021;18(1):45–56.
[22] McPherson S, Henderson E, Burt AD, Day CP, Anstee QM. Serum immunoglobulin levels predict fibrosis in patients with non-alcoholic fatty liver disease. J Hepatol 2014;60(5):1055–1062.
[23] Mouzaki M, Bramlage K, Arce-Clachar AC, Xanthakos SA. Serum immunoglobulin A levels do not correlate with liver disease severity in pediatric nonalcoholic fatty liver disease. J Pediatr Gastroenterol Nutr 2018;67(5):631–634.
[24] Shalapour S, Lin XJ, Bastian IN, Brain J, Burt AD, Aksenov AA, et al. Inflammation-induced IgA+ cells dismantle anti-liver cancer immunity. Nature 2017;551(7680):340–345.
[25] Barrow F, Khan S, Fredrickson G, Wang H, Dietsche K, Parthiban P, et al. Microbiota-driven activation of intrahepatic B cells aggravates NASH through innate and adaptive signaling. Hepatology 2021;74(2):704–722.
[26] Karl M, Hasselwander S, Zhou Y, Reifenberg G, Kim YO, Park KS, et al. Dual roles of B lymphocytes in mouse models of diet-induced nonalcoholic fatty liver disease. Hepatology 2022;76(4):1135–1149.
[27] Inamine T, Schnabl B. Immunoglobulin A and liver diseases. J Gastroenterol 2018;53(6):691–700.
[28] Chen J, Trounstine M, Alt FW, Young F, Kurahara C, Loring JF, et al. Immunoglobulin gene rearrangement in B cell deficient mice generated by targeted deletion of the JH locus. Int Immunol 1993;5(6):647–656.
[29] Wolf MJ, Adili A, Piotrowitz K, Abdullah Z, Boege Y, Stemmer K, et al. Metabolic activation of intrahepatic CD8+ T cells and NKT cells causes nonalcoholic steatohepatitis and liver cancer via cross-talk with hepatocytes. Cancer Cell 2014;26(4):549–564.
[30] Komatsu M, Waguri S, Koike M, Sou YS, Ueno T, Hara T, et al. Homeostatic levels of p62 control cytoplasmic inclusion body formation in autophagy-deficient mice. Cell 2007;131(6):1149–1163.
[31] Macpherson AJ, Lamarre A, McCoy K, Harriman GR, Odermatt B, Dougan G, et al. IgA production without mu or delta chain expression in developing B cells. Nat Immunol 2001;2(7):625–631.
[32] **Khodadadi L**, **Cheng Q**, Radbruch A, Hiepe F. The maintenance of memory plasma cells. Front Immunol 2019;10:721.
[33] Szklarczyk D, Gable AL, Lyon D, Junge A, Wyder S, Huerta-Cepas J, et al. STRING v11: protein-protein association networks with increased coverage, supporting functional discovery in genome-wide experimental datasets. Nucleic Acids Res 2019;47(D1):D607–D613.
[34] Gorenshteyn D, Zaslavsky E, Fribourg M, Park CY, Wong AK, Tadych A, et al. Interactive big data resource to elucidate human immune pathways and diseases. Immunity 2015;43(3):605–614.
[35] Tomura M, Yoshida N, Tanaka J, Karasawa S, Miwa Y, Miyawaki A, et al. Monitoring cellular movement *in vivo* with photoconvertible fluorescence protein "Kaede" transgenic mice. Proc Natl Acad Sci U S A 2008;105(31):10871–10876.
[36] Clapper JR, Hendricks MD, Gu G, Wittmer C, Dolman CS, Herich J, et al. Diet-induced mouse model of fatty liver disease and nonalcoholic steatohepatitis reflecting clinical disease progression and methods of assessment. Am J Physiol Gastrointest Liver Physiol 2013;305(7):G483–G495.
[37] Waisman A, Kraus M, Seagal J, Ghosh S, Melamed D, Song J, et al. IgG1 B cell receptor signaling is inhibited by CD22 and promotes the development of B cells whose survival is less dependent on Ig alpha/beta. J Exp Med 2007;204(4):747–758.
[38] Waisman A, Croxford AL, Demircik F. New tools to study the role of B cells in cytomegalovirus infections. Med Microbiol Immunol 2008;197(2):145–149.
[39] Peschl P, Bradl M, Höftberger R, Berger T, Reindl M. Myelin oligodendrocyte glycoprotein: deciphering a target in inflammatory demyelinating diseases. Front Immunol 2017;8:529.
[40] Wei M, Shinkura R, Doi Y, Maruya M, Fagarasan S, Honjo T. Mice carrying a knock-in mutation of Aicda resulting in a defect in somatic hypermutation have impaired gut homeostasis and compromised mucosal defense. Nat Immunol 2011;12(3):264–270.
[41] Harriman G, Bogue M, Rogers P, Finegold M, Pacheco S, Bradley A, et al. Targeted deletion of the IgA constant region in mice leads to IgA deficiency with alterations in expression of other Ig isotypes. J Immunol 1999;162(5):2521–2529.
[42] Muramatsu M, Kinoshita K, Fagarasan S, Yamada S, Shinkai Y, Honjo T. Class switch recombination and hypermutation require activation-induced cytidine deaminase (AID), a potential RNA editing enzyme. Cell 2000;102(5):553–563.
[43] Matsumoto M, Hada N, Sakamaki Y, Uno A, Shiga T, Tanaka C, et al. An improved mouse model that rapidly develops fibrosis in non-alcoholic steatohepatitis. Int J Exp Pathol 2013;94(2):93–103.
[44] Nimmerjahn F, Ravetch JV. Fcgamma receptors as regulators of immune responses. Nat Rev Immunol 2008;8(1):34–47.
[45] Hansen IS, Hoepel W, Zaat SAJ, Baeten DLP, den Dunnen J. Serum IgA immune complexes promote proinflammatory cytokine production by human macrophages, monocytes, and kupffer cells through FcαRI-TLR cross-talk. J Immunol 2017;199(12):4124–4131.
[46] Hansen IS, Baeten DLP, den Dunnen J. The inflammatory function of human IgA. Cell Mol Life Sci 2019;76(6):1041–1055.
[47] Chen L, Li J, Zhang J, Dai C, Liu X, Wang J, et al. S100A4 promotes liver fibrosis via activation of hepatic stellate cells. J Hepatol 2015;62(1):156–164.
[48] **Zheng D**, **Liwinski T**, Elinav E. Interaction between microbiota and immunity in health and disease. Cell Res 2020;30(6):492–506.
[49] Macpherson AJ, Heikenwalder M, Ganal-Vonarburg SC. The liver at the nexus of host-microbial interactions. Cell Host Microbe 2016;20(5):561–571.
[50] Bouter KE, van Raalte DH, Groen AK, Nieuwdorp M. Role of the gut microbiome in the pathogenesis of obesity and obesity-related metabolic dysfunction. Gastroenterology 2017;152(7):1671–1678.
[51] Kübeck R, Bonet-Ripoll C, Hoffmann C, Walker A, Müller VM, Schüppel VL, et al. Dietary fat and gut microbiota interactions determine diet-induced obesity in mice. Mol Metab 2016;5(12):1162–1174.
[52] Fleissner CK, Huebel N, Abd El-Bary MM, Loh G, Klaus S, Blaut M. Absence of intestinal microbiota does not protect mice from diet-induced obesity. Br J Nutr 2010;104(6):919–929.

[53] Kolodziejczyk AA, Zheng D, Shibolet O, Elinav E. The role of the microbiome in NAFLD and NASH. EMBO Mol Med 2019;11(2).
[54] Bäckhed F, Manchester JK, Semenkovich CF, Gordon JI. Mechanisms underlying the resistance to diet-induced obesity in germ-free mice. Proc Natl Acad Sci U S A 2007;104(3):979–984.
[55] Rabot S, Membrez M, Bruneau A, Gérard P, Harach T, Moser M, et al. Germ-free C57BL/6J mice are resistant to high-fat-diet-induced insulin resistance and have altered cholesterol metabolism. FASEB J 2010;24(12):4948–4959.
[56] Moretti CH, Schiffer TA, Li X, Weitzberg E, Carlström M, Lundberg JO. Germ-free mice are not protected against diet-induced obesity and metabolic dysfunction. Acta Physiol (Oxf) 2021;231(3):e13581.
[57] Tacke F. Targeting hepatic macrophages to treat liver diseases. J Hepatol 2017;66(6):1300–1312.
[58] Tacke F, Zimmermann HW. Macrophage heterogeneity in liver injury and fibrosis. J Hepatol 2014;60(5):1090–1096.
[59] Ramachandran P, Dobie R, Wilson-Kanamori JR, Dora EF, Henderson BEP, Luu NT, et al. Resolving the fibrotic niche of human liver cirrhosis at single-cell level. Nature 2019;575(7783):512–518.
[60] **Spencer J**, **Sollid LM**. The human intestinal B-cell response. Mucosal Immunol 2016;9(5):1113–1124.
[61] Rolli V, Gallwitz M, Wossning T, Flemming A, Schamel WW, Zürn C, et al. Amplification of B cell antigen receptor signaling by a Syk/ITAM positive feedback loop. Mol Cel 2002;10(5):1057–1069.
[62] Stepanek O, Draber P, Drobek A, Horejsi V, Brdicka T. Nonredundant roles of Src-family kinases and Syk in the initiation of B-cell antigen receptor signaling. J Immunol 2013;190(4):1807–1818.
[63] Wang WH, Krisenko MO, Higgins RL, Morman RE, Geahlen RL. A mouse model for the study of SYK function through chemical genetics demonstrates SYK-dependent signaling through the B cell receptor, but not TLR4. Immunohorizons 2019;3(7):254–261.
[64] Heizmann B, Reth M, Infantino S. Syk is a dual-specificity kinase that self-regulates the signal output from the B-cell antigen receptor. Proc Natl Acad Sci U S A 2010;107(43):18563–18568.
[65] Gobessi S, Laurenti L, Longo PG, Carsetti L, Berno V, Sica S, et al. Inhibition of constitutive and BCR-induced Syk activation downregulates Mcl-1 and induces apoptosis in chronic lymphocytic leukemia B cells. Leukemia 2009;23(4):686–697.
[66] Friedman SL, Ratziu V, Harrison SA, Abdelmalek MF, Aithal GP, Caballeria J, et al. A randomized, placebo-controlled trial of cenicriviroc for treatment of nonalcoholic steatohepatitis with fibrosis. Hepatology 2018;67(5):1754–1767.
[67] Martínez-Chantar ML, Delgado TC, Beraza N. Revisiting the role of natural killer cells in non-alcoholic fatty liver disease. Front Immunol 2021;12:640869.
[68] Dufour JF, Caussy C, Loomba R. Combination therapy for non-alcoholic steatohepatitis: rationale, opportunities and challenges. Gut 2020;69(10):1877–1884.

Journal of Hepatology, Volume *79*

Supplemental information

Intestinal B cells license metabolic T-cell activation in NASH microbiota/antigen-independently and contribute to fibrosis by IgA-FcR signalling

Elena Kotsiliti, Valentina Leone, Svenja Schuehle, Olivier Govaere, Hai Li, Monika J. Wolf, Helena Horvatic, Sandra Bierwirth, Jana Hundertmark, Donato Inverso, Laimdota Zizmare, Avital Sarusi-Portuguez, Revant Gupta, Tracy O'Connor, Anastasios D. Giannou, Ahmad Mustafa Shiri, Yehuda Schlesinger, Maria Garcia Beccaria, Charlotte Rennert, Dominik Pfister, Rupert Öllinger, Iana Gadjalova, Pierluigi Ramadori, Mohammad Rahbari, Nuh Rahbari, Marc E. Healy, Mirian Fernández-Vaquero, Neda Yahoo, Jakob Janzen, Indrabahadur Singh, Chaofan Fan, Xinyuan Liu, Monika Rau, Martin Feuchtenberger, Eva Schwaneck, Sebastian J. Wallace, Simon Cockell, John Wilson-Kanamori, Prakash Ramachandran, Celia Kho, Timothy J. Kendall, Anne-Laure Leblond, Selina J. Keppler, Piotr Bielecki, Katja Steiger, Maike Hofmann, Karsten Rippe, Horst Zitzelsberger, Achim Weber, Nisar Malek, Tom Luedde, Mihael Vucur, Hellmut G. Augustin, Richard Flavell, Oren Parnas, Roland Rad, Olivier Pabst, Neil C. Henderson, Samuel Huber, Andrew Macpherson, Percy Knolle, Manfred Claassen, Andreas Geier, Christoph Trautwein, Kristian Unger, Eran Elinav, Ari Waisman, Zeinab Abdullah, Dirk Haller, Frank Tacke, Quentin M. Anstee, and Mathias Heikenwalder

Intestinal B cells license metabolic T-cell activation and contribute to fibrosis via IgA-FcR signalling in NASH

Elena Kotsiliti, Valentina Leone, Svenja Schuehle, Olivier Govaere, Hai Li, Monika J. Wolf, Helena Horvatic, Sandra Bierwirth, Jana Hundertmark, Donato Inverso, Laimdota Zizmare, Avital Sarusi-Portuguez, Revant Gupta, Tracy O'Connor, Anastasios D. Giannou, Ahmad Mustafa Shiri, Yehuda Schlesinger, Maria Garcia Beccaria, Charlotte Rennert, Dominik Pfister, Rupert Öllinger, Iana Gadjalova, Pierluigi Ramadori, Mohammad Rahbari, Nuh Rahbari, Marc Healy, Mirian Fernández-Vaquero, Neda Yahoo, Jakob Janzen, Indrabahadur Singh, Chaofan Fan, Xinyuan Liu, Monika Rau, Martin Feuchtenberger, Eva Schwaneck, Sebastian J Wallace, Simon Cockell , John Wilson-Kanamori, Prakash Ramachandran, Celia Kho, Timothy J Kendall, Anne-Laure Leblond, Selina J. Keppler, Piotr Bielecki, Katja Steiger, Maike Hofmann, Karsten Rippe, Horst Zitzlesberger, Achim Weber, Nisar Malek, Tom Lüdde, Mihael Vucur, Hellmut G. Augustin, Richard Flavell, Oren Parnas, Roland Rad, Olivier Pabst, Neil C. Henderson, Samuel Huber, Andrew Macpherson, Percy Knolle, Manfred Claasen, Andreas Geier, Christoph Trautwein, Kristian Unger, Eran Elinav, Ari Waisman, Zeinab Abdullah, Dirk Haller, Frank Tacke, Quentin M. Anstee, Mathias Heikenwalder

Table of contents

Supplementary materials and methods

Mice, diets and treatments

4-week-old male C57BL/6J mice were purchased from Charles River, and all strains of genetically-altered mice were on a C57BL/6J background. Control mice were matched by genetic background, age and sex. Mice were housed at the German Cancer Research Center (DKFZ) and at the University Hospital Zurich (Labortierkunde/LTK)). Animals were maintained under specific pathogen-free conditions, and experiments were performed in accordance with German and Switzerland Law and registered at the Landesamt für Natur, Umwelt und Verbraucherschutz Nordrhein-Westfalen (LANUV) (approval no. G11/16, G7/17, AZ 84-02.04.2017.A061). *JH*$^{-/-}$ and *μMT* mice were under the license numbers ZH136/2014 and ZH217/2012. *IgMi* mice were thankfully provided by Prof. Dr. A. Waisman (animal permission: 23 177-07/G12-1-057). 4-weeks old male C57Bl/6N germ-free mice were provided by Prof. Dr. Dirk Haller, and the diet experiments took place in his germ-free facility at the Technical University of Munich (TUM) (School of Life Sciences Weihenstephan) according to the German Law (Regierung von Oberbayern, approval no. 55.2-1-54-2532-72-2015). Kaede transgenic mice[1] were provided by Prof. Dr. Samuel Huber and the diet experiments took place at the University Medical Center Hamburg-Eppendorf in accordance with the institutional review board Behörde für Justiz und Verbraucherschutz, Lebensmittelsicherheit und Veterinärwesen (approval no. G13/17). 4-week-old male mice were fed ad libitum: normal diet (ND) (Provimi Kliba, Switzerland), choline-deficient high-fat diet (CD-HFD) (Research Diets; D05010402), western diet (Ssniff Spezialdiäten GmbH, E15723-34),

CDA-HFD (Ssniff Spezialdiäten GmbH, E15673-940), and western diet with trans-fats (WD-HTF) (Research Diets; D16022301). Animals used for *ex vivo* experiments were treated in accordance with the “German Animal Protection Law” and the guidelines of the animal care unit at our university (Haus für experimentelle Therapie, Bonn, Germany) and approved by the relevant North Rhine-Westphalian state agency for Nature, Environment and Consumer Protection (LANUV, Germany) under the file reference LANUV84-02.04.2014.A137. At the end of the experiments, animals were sacrificed, and the liver, spleen, small intestine and serum were harvested for analysis.

B cells depletion experiments

B cell depletion was carried out using the CD20 antibody against mouse from Genentech (clone 5D2). 4 weeks old mice were put on CD-HFD for 4 months, followed by anti-CD20 treatment with intraperitoneal (i.p.) injections of 200µg, once per week, with pause one week in between, for a total duration of treatment of 6 weeks.

Kaede mice

For photoconversion, the small intestine of anaesthetized Kaede transgenic mice, which constitutively express a photoconvertible fluorescent protein in all cells, was subjected to lighting using a Blue Wave LED Prime UVA (Dymax), essentially as described before[2]. At 6 months, upon different diet feeding (ND, WD-HTF or CD-HFD), the small intestine of Kaede mice was photo-converted to label cells from green to red, enabling direct tracing of cells from the small intestine to other tissues. The mice were sacrificed 48h after photoconversion and Flow cytometry of livers was performed.

Confocal microscopy for Kaede mice

Liver samples derived from Kaede transgenic mice were observed with a confocal microscope (Leica, SP5) and illuminated with a laser with 488 nm for green Kaede and 561 nm for photoconverted Kaede, respectively; these emission signals were obtained by setting the wavelength range at 500–550 nm and 570–620 nm, respectively.

Measurement of liver triglycerides

Liver triglycerides were measured by crushing 20 - 50 mg of tissue in liquid with a pestle and adding 250µl 0.9% NaCl. After incubation on heat block for 10min, RT, 450rpm, 250µl ethanolic 0.5M KOH was added, samples were vortexed and incubated for 30min, 71°C, 450rpm. 500µl 0.15M $MgSO_4$ was added, and samples were vortexed. After centrifugation for 10min, RT, 13,000g supernatants were collected and analyzed by using optical densitometry O.D. 505 with 1:4 diluted liver samples by GPO-PAP from Roche Diagnostics[3].

Intraperitoneal glucose tolerance test

After overnight fasting, mice were i.p injected with 5µl/gr body weight of a 20% glucose solution, blood glucose was measured using Accu-chek Performa Glucometer at the indicated time intervals (15, 30, 60 and 120 minutes post glucose administration), by puncturing the lateral tail vein[3].

Measurement of serum parameters

Serum was isolated from the heart blood after sacrifice, and parameters were measured by using either a Fuji DRI-CHEM NX500i machine with a commercially available test application from FUJIFILM for ALT, cholesterol and triglycerides or analyzing parameters on a Cobas Reader in collaboration with the Institute for Clinical Chemistry and Pathobiochemistry, Technical University of Munich[3].

CCl4 injection

For the acute liver injury experiment, liver mice received one intraperitoneal application of Carbon tetrachloride (CCl_4) (Merck, Darmstadt, Germany) dissolved in corn oil at a concentration of 0.6 mL/kg body weight. Mice were sacrificed after 36 hours from the injection. For long-term injections, CCl_4 was intraperitoneally injected at 0.6 mL/kg body weight (BW) twice per week for 8 weeks.

RNA isolation from murine livers and quantitative real-time PCR

Total RNA was isolated from snap-frozen liver tissues according to the manufacturer's protocol using RNeasy Mini Kit (Qiagen). The quantity and quality of the RNA were determined spectroscopically using a Nanodrop analyzer (Thermo Scientific). 1 µg of purified RNA was subsequently transcribed into cDNA using Quantitect Reverse Transcription Kit (Qiagen) according to the manufacturer's protocol. Quantitative RT-PCR was performed using Fast Start SYBR Green Master Rox (Roche). Primers were designed using Primer-Blast. For mRNA expression analysis, quantitative real-time PCR was performed in duplicates in 384-well plates using Fast Start SYBR Green Master Rox (Roche) on a 7900 HT qRT-PCR system (Applied Biosystems, Life

Technologies Darmstadt, Germany). Relative mRNA levels were calculated according to the ΔΔCt relative quantification method and were normalized to levels of a housekeeping gene (GAPDH). The data were normalized to the expression of the housekeeping gene and analyzed using GraphPad Prism software version 9.3 (GraphPad Software)[3].

For a list of all used primers for RT-qPCRs, refer to **Table S1**.

Library preparation for bulk murine liver tissue RNA sequencing (RNA-Seq)

The libraries were prepared with 30 ng of total RNA using QuantSeq 3′ mRNA-Seq Library Prep Kit FWD for Illumina (Cat.No. 015.96, Lexogen GmbH, Austria) with single-indexing, according to the manufacturer's instruction for low-quality RNA. To determine the optimal cycle number for the library amplification the PCR Add-on Kit from Illumina (Cat.No. 020.96, Lexogen GmbH, Austria) was used. The individual libraries were eventually amplified with 24 PCR cycles.

Flow cytometry and FACS: Isolation and staining of lymphocytes

Mice were sacrificed with CO_2, and livers, spleens, blood and small intestines were dissected. Livers were incubated for up to 35min at 37°C with digestion buffer (Collagen IV 1:10 (60 U f.c.) and DNase I 1:100 (25µg/ml f.c.)) and subsequently passed through a 100µm filter. Livers were washed with RPMI1640 (Cat.No.11875093) medium and subsequently centrifuged for 7min/300g/4°C. Lymphocyte enrichment was achieved by a 2-step Percoll gradient (20ml 25% Percoll/HBSS underlay with 20ml 50% Percoll/HBSS) and centrifugation for 15min/1800g/4°C (Acc:1 Dcc:0). Leukocytes were collected, washed with HBSS, centrifuged for 10min/700g/4°C, counted and transferred to a 15ml Falcon for a final washing step with FACS buffer (PBS

supplemented with v/v 0.4% 0.5M EDTA pH= 8 and w/v 0.5% albumin fraction V (Cat.No.90604-29-8)). Isolation of splenic lymphocytes was done by passing spleens through a 100µm mesh and subsequent washing. Isolation of blood-derived lymphocytes was done by collection of blood in FACS buffer and performing erythrocyte lysis two times using ACK-buffer 1x 2ml for 5 min RT and then washing. Afterwards, an erythrocyte lysis using ACK-buffer 1x 2ml for 5 min RT and then a wash was performed. Small intestines were harvested and cleaned of fat residue and Peyer's patches. To obtain lamina propria cells (LPC), the small intestine was cut longitudinally and scraped in PBS 1X to clean the mucus and faeces. The clean tissue was fragmented into pieces in 20ml HBSS 2% FCS. The pieces were filtered through a 100µm mesh and were incubated in 10ml HBSS 2mM EDTA in a shaker at 37°C for 20 min. The pieces were rinsed with HBSS through a 100µm mesh and incubated in 10ml HBSS 2mM EDTA in a shaker at 37°C for 20 min. The pieces were rinsed with HBSS, filtered through a 100µm mesh and incubated in 15 ml IMDM +10% FCS containing 1mg/ml collagenase VIII (Sigma) in a shaker at 37°C for 15 min in order to disaggregate the tissue. Single-cell suspensions were then washed and filtered (100 and 40 µm cell strainer). For T-cell re-stimulation, cells were incubated for 2h, 37°C, 5% CO_2 in RPMI 1640 supplemented with v/v 2% fetal calf serum using 1:500 Biolegend´s Cell Activation Cocktail (with Brefeldin A) (Cat.No.423304) and 1:1000 Monensin Solution (1,000X) (Cat.No.420701). Staining was performed using Live/Dead discrimination by using DAPI or ZombieDyeNIR according to the manufacturer´s instructions. After washing (~400g, 5min, 4°C), cells were stained in 25µl of titrated antibody master mix for 20min at 4°C and washed again (antibodies shown in **tables 2** and **3**). Samples for flow cytometric activated cell sorting (FACS) were then sorted. Samples for flow cytometry were fixed using eBioscience IC fixation

(Cat.No.00-8222-49) according to the manufacturer´s instructions. Cells were analyzed using BD FACSFortessa, and data were analyzed using FlowJo. For sorting, a FACS Aria II and a FACSAria FUSION in collaboration with the DKFZ FACS core facility were used[3].

Immunoglobulin A (IgA) ELISA

96-well flat-bottom plates (Nunc) were coated by using goat anti-mouse IgA (1040-01, SouthernBiotech) as coating antibody at 4°C overnight. Plates were washed by washing buffer (0.05% Tween 20 in PBS) and blocked with 2% (w/v) BSA/PBS. Serum or homogenised tissue was loaded onto plates for 1hr room temperature incubation. Peroxidase-conjugated anti-mouse IgA α chain specific antibody (A4789, Sigma) and ABTS (Boehringer) were sequentially added as secondary antibody and substrate. IgA purified from mouse myeloma (Cat.No.553476, BD Pharmingen™) was included as a quantification standard.

Faecal IgA flow cytometry and sorting of IgA^+ and IgA^- bacteria

Faecal homogenates were stained with PE-conjugated Anti-Mouse IgA (eBioscience, clone mA-6E1) prior to flow cytometric analysis and FACS sorting[4]. In detail, faecal pellets collected directly from two co-housed mice or ~100 mg of frozen murine faecal material were placed in Fast Prep Lysing Matrix D tubes containing ceramic beads (MP Biomedicals) and incubated in 1 mL Phosphate Buffered Saline (PBS) per 100 mg faecal material on ice for 1 hour. Faecal pellets were homogenized by bead beating for 5 seconds (Minibeadbeater; Biospec) and then centrifuged (50 x g, 15 min, 4°C) to remove large particles. Faecal bacteria in the supernatants were removed (100

µl/sample), washed with 1 mL PBS containing 1% (w/v) Bovine Serum Albumin (BSA, American Bioanalytical; staining buffer) and centrifuged for 5 min (8,000 x g, 4°C) before resuspension in 1 mL staining buffer. A sample of this bacterial suspension (20 µl) was saved as the Pre-sort sample for 16S sequencing analysis. After an additional wash, bacterial pellets were resuspended in 100 µl blocking buffer (staining buffer containing 20% Normal Rat Serum for mouse samples or 20% Normal Mouse Serum for human samples, both from Jackson ImmunoResearch), incubated for 20 min on ice, and then stained with 100 µl staining buffer containing PE-conjugated Anti-Mouse IgA (1:12.5; eBioscience, clone mA-6E1) for 30 minutes on ice. Samples were then washed 3 times with 1 mL staining buffer before flow cytometric analysis or cell separation. Anti-IgA-stained faecal bacteria were incubated in 1 ml staining buffer containing 50 µl Anti-PE Magnetic Activated Cell Sorting (MACS) beads (Miltenyi Biotec) (15 min at 4°C), washed twice with 1 ml Staining Buffer (10,000 x g, 5 min, 4°C), and then sorted by MACS (Possel_s program on an AutoMACS pro; Miltenyi). After MACS separation, 50 µl of the negative fraction was collected for 16S sequencing analysis (IgA negative fraction). The positive fraction was then further purified via Fluorescence Activated Cell Sorting (FACSAria; BD Biosciences). For each sample, 2 million IgA-positive bacteria were collected, pelleted (10,000 x g, 5 min, 4°C), and frozen along with the Pre-sort and IgA-negative samples at -80°C for future use[4].

Opt-SNE analysis

Visualization of the global single-cell landscape was performed in OMIQ using Opt-SNE based on channels IgA, CD20, and B220 for the B cells (random seed 3719, max iterations 1000, opt-SNE end 5000, perplexity 30, theta 0.5 and verbosity 25) for the B

cells pre-gated on $CD45^{+}livedump^{-}$. Visualization of T-cells of the global single-cell landscape was performed in OMIQ using Opt-SNE based on channels CD8α, PD-1, and CD4 (random seed 7996, max iterations 1000, opt-SNE end 5000, perplexity 30, theta 0.5 and verbosity 25) on cells pre-gated to $CD45^{+}liveCD19^{-}$.

Histology, immunohistochemistry, scanning and automated analysis

Tissues were fixed in 4% paraformaldehyde and paraffin-embedded. For immunofluorescence staining, organs were fixed in 4% PFA for 12 hours, then transferred to 30% sucrose solution until the organs sank. Afterwards, organs were transferred into 70% EtOH before dehydration and paraffin embedding. Briefly, 2µm sections from formalin-fixed paraffin-embedded (FFPE) and cryo-preserved tissues were prepared and stained with Hematoxylin/Eosin or IHC antibodies (**Table S4**) on a Bond MAX (Leica). Slides were scanned with SCN400 slide scanner (Leica) and analyzed either using for area-based staining Tissue IA image analysis software by Leica Biosystems Version 4.0.6, or macro-based analysis by ImageJ, Aperio System. For Sudan red^{+} liver areas, data are presented as a percentage of total tissue area. Five random liver tissue areas of 10X zoom were selected in Aperio. NAFLD activity scoring (NAS) was performed on mouse livers[3]. For immunofluorescence staining, IHC-established antibodies were used, coupled by the AKOYA Biosciences Opal fluorophore kit (Opal 520 Cat.No. FP1487001KT, Opal 540 Cat.No. FP1494001KT, Opal 620 Cat.No. FP1495001KT). Confocal microscopy was performed on 30 µm thick FFPE small intestine (ileum) sections, stained with IHC-established antibodies (**Table S4**), like previously described[5]. Briefly, antigen retrieval was performed in 1mM EDTA

ph9 0.05% tween-20 at 100°C for 20 minutes. Sections were then permeabilized and blocked in PBS containing 0.3% Triton X-100 (Sigma-Aldrich) and 10% FBS followed by staining in the same blocking buffer. Stained slides were mounted with Fluorsave (Merck Millipore) and images were acquired on an inverted Leica microscope (TCS STED CW SP8, Leica Microsystems) with a motorized stage for tiled imaging. 3D reconstruction using Imaris (Bitplane) was described previously[5].

Murine intestine and liver single-cell RNA-Seq analysis

Sequencing output reads were converted to FASTQ files using bcl2fastq (v1.8.3) and aligned to the mm10 reference genome (2020-A version, downloaded from 10X website), using the Cell Ranger pipeline (v6.0.1, 10X Genomics). Filtered raw counts data was imported into Seurat R package (v4.0.4) (PMID: 29608179) for further processing and analysis. Raw transcript counts of gene–cell matrices were filtered to remove cells with fewer than 500 transcripts and 250 features and cells with more than 10% mitochondrial genes. In addition, genes expressed in less than 10 cells were removed from the analysis. The UMI counts matrices were then log normalized and scaled with Seurat's NormalizeData and ScaleData functions. The Seurat package was applied to identify major cell types using dimension reduction followed by clustering of cell groups. Genes with the highest variance were used to perform linear dimensional reduction (principal component analysis), and the number of principal components used in downstream analyses was chosen considering Seurat's PCHeatmap and Elbowplot. Seurat's unsupervised graph-based clustering was performed on the projected PC space. We used Seurat to perform graph-based unsupervised clustering, uniform manifold approximation and (UMAP) (McInnes, L.,

Healy, J., Saul, N. & Großberger, L. UMAP: uniform manifold approximation and projection. J. Open Source Softw. 3, 861 (2018)) and t-stochastic neighbour embedding (t-SNE), for data visualization in two-dimensional space. P values were calculated using one-vs.-rest Seurat's *FindAllMarkers* function configured with Wilcoxon signed-rank statistical test (two-sided test), min.pct = 0.5 and logfc.threshold=0.5. Differentially expressed genes of the clusters were used to identify cell types with help from "ImmGen – My Gene Set web tool" (http://rstats.immgen.org/MyGeneSet_New/index.html). Differentially expressed genes between the conditions within each cluster were calculated using Seurat FindMarkers function configured with Wilcoxon signed-rank statistical test (two-sided test), min.pct = 0.1, logfc.threshold = 0.25. Dot plots were created by modifying the output of Seurat DotPlot function. Violin plots and double violin plots were scattered using Seurat VlnPlot function.

Expression of subset of cells identified as MoMF cells (louvain clusters 1, 3, 6, 9, 17) was projected in 2D using UMAP via SCANPY[6]. Fifteen PC components were used to estimate a five-neighbour knn graph to estimate the UMAP projection. FcRγ signalling per cell was estimated with the ssgsea method implemented in the R package GSVA[7]. Distribution of mean of FCGR1 gene expression and FcRγ signalling for each sample (mouse) was plotted per diet group. Mann-Whitney U test was used to assess the significance of differential expression between control and non-control diet groups (western diet and CDA-HFD diet). SciPy 1.0 implementation of the test was used[8]. Mean expression of 496 orthologous genes that were found to be expressed in both the pre-processed human and pre-processed mouse scRNA-Seq datasets were computed for the following cell groups: SAMac, non-SAMac, MoMF and non-MoMF

cells. For each cell group the rank of the mean expression value across all genes was plotted as a clustermap using *Seaborn*.

Isolation of RNA and library preparation for bulk RNA sequencing (sorted intestinal B220+ and CD20+ cells)

300-1000 cells were sorted for each sample directly in a well (low binding Eppendorf) containing 5µl lysis buffer (500µl lysis buffer: 250 µl of 2X TCL buffer (Qiagen, Cat.No.1070498) plus 245 µl of RNase-free water and 5 µl (1% of total volume) of b-mercaptoethanol). Nucleic acids of the lysates were purified with AMPure XP beads (Beckman Coulter). 1.8 volume of reagent and lysate were mixed thoroughly by pipette, followed and kept for 5 min at room temperature (RT). The mix was then placed onto Magnet Plate for 3 min to separate beads from the solution. The resulting cleared solution was aspirated from the reaction plate and discarded. Then were dispensed 150 µl of 80% ethanol to each well; 30 sec RT, aspirated out and discarded, followed by one repetition, and let it dry for 5 min at RT. Off the magnet plate, were added 6 µl of elution buffer (RNase-free water), pipette and mixed 10 times. On the magnet plate 1 min to separate beads from the solution. The eluate was then transferred to the retro-transcription mix for RNA-Seq processing. For the RNA-Seq, library preparation for bulk-sequencing of poly(A)-RNA was done as described previously (Parekh et al., 2016). Briefly, barcoded cDNA of each sample was generated with a Maxima RT polymerase (Thermo Fisher) using oligo-dT primer containing barcodes, unique molecular identifiers (UMIs) and an adaptor. Ends of the cDNAs were extended by a template switch oligo (TSO) and full-length cDNA was amplified with primers binding to the TSO-site and the adaptor. NEB UltraII FS kit was used to fragment cDNA. After end repair and A-tailing a TruSeq adapter was ligated

and 3'-end-fragments were finally amplified using primers with Illumina P5 and P7 overhangs. In comparison to Parekh et al. (2016)[9], the P5 and P7 sites were exchanged to allow sequencing of the cDNA in read1 and barcodes and UMIs in read2 to achieve better cluster recognition. The library was sequenced on a NextSeq 500 (Illumina) with 63 cycles for the cDNA in read1 and 16 cycles for the barcodes and UMIs in read2. Data were processed using the published Drop-seq pipeline (v1.0) to generate sample- and gene-wise UMI tables[10]. Reference genome (GRCm38) was used for alignment. Transcript and gene definitions were used according to the GENCODE Version M25.

Differential gene expression bulk transcriptomes of liver tissues and of FACS-sorted B-cells

Gene-level raw RNA-seq read counts were imported into R using the DESeq2 DESeqDataSetFromMatrix function[11]. Genes with less than 10 reads across all samples were excluded from the analysis. Differential expressions between tested conditions were determined using the linear modelling approach as implemented in DESeq2, while statistical significance was accepted for absolute log2-fold changes greater than 0.5, p-values smaller than 0.05 and false-discovery rates of smaller than 25%.

Liver CD45$^+$ sorting and 10X scRNA-Seq

All experiments were performed with male C57BL6/J wildtype mice that were housed under pathogen-free conditions at the Animal Facility of the University Hospital Aachen. Livers were first perfused with 5 ml of PBS. Afterwards, livers were put in a digestion medium containing collagen-IV solution and placed in a waterbath (37°C) for 30 min. Liver cells were sorted for CD45$^+$ cells (APC-Cy7), excluded B and T Cells and

Neutrophils (Table S5) in a BD FACSAria II Cell Sorter. Staining for sorting liver $CD45^+$ cells (for scRNA-Seq) is reported in Table S5, and it was used Hoechst to exclude dead cells. After the isolation, the cells were washed once with cold PBS + 0.1% BSA and subjected to single-cell RNA sequencing analysis using the Chromium System (10x Genomics, California, USA). The used kits were based on v2 chemistry, using Chromium Single Cell 3' Library & Gel Bead Kit v2, and Chromium Single Cell A Chip Kit. Sequencing was performed on Illumina NextSeq 550 platform (paired-ends, 2×75 bp).

Primary cell cultures

Bone-marrow-derived macrophages (BMDMs) were derived using bone marrow from the femurs and tibias of male mice and seeded at 1.0×10^4 cells per cm^2 in Roswell Park Memorial Institute Medium (RPMI, GIBCO) containing 10% FCS (heat inactivated: 56 ºC, 30min) + 1% Pen/Strep + MCSF in a final concentration of 50ng/ml. BMDMs were washed and treated in the same conditions for seven consecutive days. After eight days, in which cells had fully differentiated into macrophages, they were pre-treated with Fc block (1:100), treated with IgA (165ug/ml), and/or 3% of serum from mice fed a CD-HFD or ND, 3% of serum from mice treated with CCl_4. RNA was extracted from the cells for q-RT PCR analysis.

Chemokine dependent migration of bone-marrow derived cells

$1x10^6$ total bone-marrow-derived cells (isolated as described above) were cultured on 200 µl RPMI-1640 + 1% Pen/Strep + 1:200 BSA 3% together with 100 ng/ml of CCL2

chemokine (Cat.No. 250-10, PeproTech) on culture inserts into a 24-well plate. After an incubation of 37°C for 90 min, migrated cells were gently scratched from the lower side of the membrane collected. Also, migrated cells into the lower compartment of the plate were collected, washed and analysed by FACS.

Multiplex cytokine assay

Liver and serum samples from mice fed a CD-HFD, or a ND were analyzed for cytokines (IL-1β, TNF and IL-6) using the MSD U-PLEX Biomarker Group 1 (mouse) assay according to the manufacturer's instructions.

Hydroxyproline Assay

Hepatic collagen was measured as described[12]. Briefly, liver samples were hydrolyzed with 6 N HCl at 110°C for 16 hours, then filtered and mixed with methanol and evaporated by a vacuum concentrator (Eppendorf). The crystallized samples were dissolved in 50% isopropanol and incubated with 0.6% chloramine-T for 10 minutes. One hundred microliters of freshly prepared Ehrlich's reagent were added, and samples were incubated at 50°C for 45 minutes under constant shaking. Samples were measured at 570 nm, and concentrations of total liver hydroxyproline were calculated against a standard curve.

EAE (Experimental Autoimmune Encephalomyelitis) induction and scoring

Mice were injected with 50 µg $MOG_{35–55}$ emulsified in complete Freund's adjuvant (CFA) supplemented with 10mg/mL heat-inactivated *Mycobacterium*

tuberculosis H37RA into the tail base. In addition, mice were intraperitoneally injected with 100 ng of pertussis toxin (PTx) on days 0 and 2. Mice were observed daily to monitor EAE clinical symptoms on a scale from 0 to 4. Daily scoring was performed using the following criteria:0, no disease; 0.5: limb tail; 1: paralyzed tail; 1.5: weakened righting reflex; 2: no righting reflex; 3: partial paralysis of hind legs; 3.5: paralysis of one hind leg; 4: paralysis of both hind legs.

IL-2 ELISA

Splenocytes from EAE-immunized mice were collected and restimulated with 5 ug/ml MOG $_{35–55}$ peptide for 2 days. The culture supernatants were collected and IL-2 were measured by ELISA accordingly the manufacturer´s description (BD, Cat.No. 555148).

In vitro co-culture

Single-cell suspension of small intestine (SI) lamina propria was generated as described[13]. Briefly, SI were harvested and cleaned of fat residue and Peyer's patches. To obtain lamina propria cells the small intestine was cut longitudinally and scraped in PBS 1X to clean the mucus and feces. The clean tissue was fragmented into pieces in small intestine Predigestion Medium (RPMI 1640 + GlutaMAX 1X (Gibco) supplemented with 10 mM HEPES, 5 mM EDTA, 1 mM DTT (Sigma), and 5% FBS) and incubated in a shaker at 37°C for 20 min. The supernatant was discarded and the samples were washed 4 times with PBS 1X to remove EDTA; they were subsequently incubated in SI Digestion Medium (RPMI 1640 + GlutaMAX 1X supplemented with 10 mM HEPES, 50 µg/ml DNase I (Roche), and 20 µg/ml Liberase DH (Roche)) for 27

min in a shaker at 37°C in order to disaggregate the tissue. Single-cell suspensions were then washed, and filtered (40 μm cell strainer) and the B cells were enriched with a EasySep murine B cell isolation kit (Cat.No. 19844, StemCell Technologies) according to the manufacturer's protocol. For the isolation of splenic $CD8^+$ T cells, spleens were smashed (70 μm cell strainer), erythrocytes lysed with red blood cell lysis buffer and $CD8^+$ T cells were enriched with Miltenyi Biotec murine $CD8\alpha^+$ T cell isolation kit (Cat.No.130-104-075) according to the manufacturer's protocol. Small intestine B cells and splenic T cells were co-cultured 1:1 in X-VIVO 15 media (Cat.No..BE02-060F, Lonza) supplemented with L-glutamine and 10% FBS in the presence of Dynabeads Mouse T-Activator CD3/CD28 (Cat.No.11456D, Thermo Fisher). OT-1 T cells were also processed using Miltenyi Biotec murine $CD8\alpha^+$ T cell isolation kit, and were co-cultured with isolated intestinal B cells (concentration 1:1) in the presence of Dynabeads.

Flow cytometry stainings of surface-expressed molecules were performed in FACS buffer containing PBS with 2mM EDTA and 2% FBS. Cell viability was assessed by staining with LIVE/DEAD Fixable Near-IR dye (Cat.No. L10119, Invitrogen). Antibodies used are listed in Table S6.For experiments with blocking antibodies, were used 10 μg/ml of anti-LFA-1α (Cat.No.BE0006-1MG, clone M17/4, BioXCell); anti-ICAM1 (Cat.No. BE0020-1, clone YN1/1.7.4, BioXCell); anti-MHCI (Cat.No. BE0077, clone M1/42.3.9.8, BioXCell). All flow cytometry analyses were performed on a BD LSRFortessa (BD Biosciences) and analyzed with FlowJo software (Treestar).

Immunohistochemistry and Immunofluorescence of human liver tissues

Human FFPE liver samples from 31 NAFLD liver biopsies were immunostained with antibodies directed against FcεRIγ (sc390222, Santa Cruz Biotechnology), S100A4 (PRB-497P, Biolegend) and CCR2 (ab176390, Abcam). Envision Flex+ reagent (Dako) was used as secondary antibody at room temperature and 3',3'-diaminobenzidine for the visualization step. Immunopositive cells in the liver biopsies were quantified in the parenchyma and the portal tracts using the Positive Cell Detection tool from QuPath vs2.3.[17] In addition, portal infiltrate was assessed using a semi-quantitative score: 0=absent, 1= few cells in >=1PT, 2= +/- one aggregate in >=1PT, 3=aggregates in every PT.

Fluorescent double staining was performed on a selection of 6 human NAFLD FFPE biopsy samples using antibodies against FcεRIγ (sc390222, Santa Cruz Biotechnology), S100A4 (PRB-497P, Biolegend) and CD163 (ab182422, Abcam). Goat anti-mouse Alexa Fluor 488 and Goat anti-rabbit Alexa Fluor 594 were used as secondary antibodies (Invitrogen™/Thermo Fisher Scientific). Nuclear counterstaining was performed using 4',6-diamidino-2-phenylindole (Invitrogen™). Slides were analyzed using the Leica TCS SP8 confocal microscope platform (Leica Microsystems).

Human bulk liver transcriptome analysis

For bulk liver transcriptome heatmap visualization (NASH F0-F4 versus NAFL) Fastqc (v0.11.5) and MultiQC (v1.2dev) were used for raw sequencing quality assessment and alignment to the reference genome (GRCh38, Ensembl release 76). Gene-level count tables were produced using HT-Seq. Trimmed mean of M values method was

used to normalize counts and limma's voom methodology for transformation. A correction for sex, batch and centre effect was implemented.

Single-cell RNA-Seq analysis of CD45$^+$ cells from human livers

The scRNA-Seq data of the immune cells from healthy donors (n=5) and from cirrhotic patients (n=5) which were part of the study of Ramachandran et al. (2019)[18], and from unpublished data (1 cirrhotic patient), of which were provided as an R-Seurat v2 object. The object which contained detailed annotation of immune cell types was converted to an h5ad Annotated Dataframe object before importing into a Python environment. The newly generated data from another healthy donor was also imported. The two datasets were independently preprocessed using SCANPY (1.8.2)[6] which included count normalization per cell, filtering out cells with less than 200 genes expressed and excluding genes which were detected in less than 3 cells. The two data sets (z-scaled) were integrated using the SCANPY ingest method in which immune cell annotations of cells of the new dataset were learnt from the ground-truth annotation ("annotation_indepth") of the Ramachandran et al. (2019) data set. Two-dimensional UMAP (Uniform Manifold Approximation and Projection) plots based on neighbourhood graphs were generated for topological representation of cell transcriptomes in relation to immune cell annotations. FC-gamma-receptor pathway activity was inferred from scRNA-Seq counts using R GSVA[7] executed using Python rmagic (rpy). The Mann-Withey U test was applied to the per-sample averaged values for gene expression or pathway activity to statistically test for differences between groups.

Patient selection

845 cases were derived from the European NAFLD Registry (NCT04442334)[14]. These included 639 cases with histologically characterized NAFLD for whom serum IgA levels measured during routine clinical management were available, recruited from the Freeman Hospital, Newcastle Hospitals NHS Foundation Trust, Newcastle-upon-Tyne, UK. Liver tissue samples were scored according to the semi-quantitative NASH-CRN Scoring System[15]. Patient samples were grouped according to disease activity and stage: non-alcoholic fatty liver and non-alcoholic steatohepatitis (NASH) with different stages of fibrosis (F0 to F4). Alternate diagnoses and etiologies, such as excessive alcohol intake, viral hepatitis, and autoimmune liver diseases, were excluded. A subset of 54 cases was used for immunohistochemistry and/or immunofluorescence as described above, of which clinical features are listed in **Table S7**. In addition, RNA sequencing analysis was performed using the data from 206 snap-frozen biopsy samples from 206 patients diagnosed with NAFLD from France, Germany, Italy and the UK (GSE135251)[16]. This study was approved by the relevant Ethical Committees in the participating countries. Jejunum human samples were collected from the hospital of Mannheim (ethical number 2012-293N-MA), and of Würzburg (ethical permits 96/12 and 188/17).

Statistical analyses

Mouse data are presented as the mean ± SEM. Pilot experiments and previously published results were used to estimate the sample size, such that appropriate statistical tests could yield significant results[19]. Statistical analysis was performed using

GraphPad Prism software version 9.3 (GraphPad Software). Exact p-values lower than p< 0.1 are reported and specific tests are indicated in the legends.

Supplementary tables

Table S1. Murine primer sequences for qRT-PCR

Gene	Primer sequence
mAbca1 fwd	GTT TTG GAG ATG GTT ATA CAA TAG TTG T
mAbca1 rev	TTC CCG GAA ACG CAA GTC
mAcad10 fwd	TGG CTG TGG GCT GGG AG
mAcad10 rev	AAA TAG GAG CTG ACG GGC AC
mAcat2 fwd	GAC CCC GTG GTC ATC GTC
mAcat2 rev	CCA CAA CCT GCC GTC AAG A
mAcat3 fwd	TGG CCA CTT TGA CAA GGA GAT
mAcat3 rev	CTGTTGCATTAGCAGTTGTGA
mAcot2 fwd	CTC GTC TTT CGC TGT CCT GA
mAcot2 rev	CTC AGC GTC GCA TTT GTC CG
mAcox3 fwd	GGG TGA TGG TCG GTG ACA TT
mAcox3 rev	CGG ACA TCC TTA AAG GGG CT
mAcsbg1 fwd	ACT CGC AAA CCA GCT CC
mAcsbg1 rev	AGT ACA GAA AGG TTC CAG GCG
mAcsl1 fwd	ATC TGG TGG AAC GAG GCA AG
mAcsl1 rev	TCC TTT GGG GTT GCC TGT AG
mAcsm2 fwd	GCC AGA CAG AAA CGG GAC TT
mAcsm2 rev	ACA TGC CGA TAG GCC AGA TG
mCcl5 fwd	TTA GCC TAG ATC TCC CTC G
mCcl5 rev	CGA CTG CAA GAT TGG AGC ACT
mCol1a1 fwd	ACG CAT GAG CCG AAG CTA AC
mCol1a1 rev	TTG GGG ACC CTT AGG CCA TT
mCol6a1 fwd	CCC CTG GAG AGA GGG GTG GC
mCol6a1 rev	CCG GGG AAA CCT TCC GTG CC
mCxcl1 rev	AGT GTG GCT ATG ACT TCG GTT
mCxcl1 fwd	GCC TCT AAC CAG TTC CAG CA
mEl fwd	CTA TCC CAA TGG CGG TGA CTT C
mEl rev	CGT GCT CGC ATT TCA CCA TC
mFmod fwd	TCC AAC CCA AGG AGA CCA GA
mFmod rev	GGT CGT AGT AGG TGG ACT GC
mGpat fwd	GCT GCA ACT GAG ACG AAC CT
mGpat rev	AAG CCC CCA AGC TTG TGA AT
mHl fwd	CTA TGG CTG GAG GAA TCT G
mHl rev	TGG CAT CAT CAG GAG AAA G

Gene	Primer sequence
mIL-1b fwd	TCC CGT GGA CCT TCC AGG ATG A
mIL-1b rev	GGG AAC GTC ACA CAC CAG CAG G
mIL-6 fwd	CTC TGG AGC CCA CCA AGA AC
mIL-6 rev	GTC ACC AGC ATC AGT CCC AA
mLgals1 fwd	CTC AAA GTT CGG GGA GAG GTG
mLgals1 rev	AGC GAG GAT TGA AGT GTA GGC
mLgals3 fwd	TAA TCA GGT GAG CGG CAC AG
mLgals3 rev	CCA GAG CCA GCT AAG GCA TC
mLipe fwd	CTT CCA GTT ACC TGC CA
mLipe rev	AAT CGG CCA CCG GTA AAG AG
mLum fwd	TGA ACT GGC TGA TAG TGG GG
mLum rev	GAG TAA GAC AGT GGT CCC AGG
mMvd fwd	GAG GGA GAC CTC TCC GAA GT
mMvd rev	GTC TGC ARG CCC ACT GTA CT
mPdgfr1a fwd	TGG CAT GAT GGT CGA TTC TA
mPdgfr1a rev	CGC TGA GGT GGT AGA AGG AG
mPpard fwd	GAA CAG CCA CAG GAG GAG AC
mPpard rev	GAG GAA GGG GAG GAA TTC TG
mS100a4 fwd	CAC TTC CTC TCT CTT GGT CTG
mS100a4 rev	AAC TTG TCA CCC TCT TTG CC
mSpp1 fwd	ATG AGG CTG CAG TTC TCC TGG
mSpp1 rev	GCC AAA CAG GCA AAA GCA AAT C
mSqle fwd	GCA ATC TAC GCC ACG TAT TTC T
mSqle rev	GGG CCC GTG GTT TTG T
mTgfb1 fwd	GGA GCA ACA TGT GGA ACT C
mTgfb1 rev	CAG CAG CCG GTT ACC AAG
mTnfa fwd	CGA TGG GTT GTA CCT TGT C
mTnfa rev	CGG ACT CCG CAA AGT CTA AG
mTrem2 rev	GAA AGA GGA GGA AGG TGG TAG GC
mTrem2 fwd	AGG TCC TGC AGA AAG TAC TGG T
Pdgfbr fwd	GCT CCG TCT ACG CGT CC
Pdgfbr rev	GAA TGG GAT CCC CCT CGG
Tgfb1 fwd	GGA GCA ACA TGT GGA ACT C
Tgfb1 rev	CAG CAG CCG GTT ACC AAG

Table S2. Flow cytometry antibodies used for murine intestine experiments

Small Intestine - flow cytometry antibodies				
Marker	**Fluorochrome**	**Clone**	**Ordering #**	**Company**
CD44	Brilliant Violet 421™	IM7	103039	Biolegend
CXCR4	Brilliant Violet 421™	L276F12	146511	
LIVE/DEAD	Brilliant Violet 510™		423102	
PD-1(CD279)	Brilliant Violet 605™	29f.1a12	135220	
CD4	Brilliant Violet 650™	GK1.5	100469	
B220	Brilliant Violet 650™	RA3-6B2	103241	
IgA	FITC	C10-3	559354	BD Pharmingen™
CD20	PE	SA271G2	152105	Biolegend
CD69	PE	H1.2F3	104508	
IgM	PE	RMM-1	406507	
CD45	PE/Cyanine5	30-F11	103110	
CD19	PE/Cyanine7	6D5	115520	
CD20	PE/Cyanine7	SA275A11	150419	
CD62L	PE/Dazzle™	MEL-14	104448	
IgD	PE/Dazzle™	11-26c.2a	405741	
CD8α	PerCP/Cyanine5.5	53-6.7	100734	
MHC-II	PerCP/Cyanine5.6	M5/114.15.2	107625	

Table S3. Flow cytometry antibodies used for murine liver experiments

Liver - flow cytometry antibodies				
Marker	**Fluorochrome**	**Clone**	**Ordering #**	**Company**
CD4	Alexa Fluor® 700	RM4-5	100536	Biolegend
CD45		30-F11	103128	
MHC-II		M5/114.15.2	107622	
CD11b	APC	M1/70	101212	
CD3		17A2	100236	
CD44		IM7	103012	
IFN-γ		XMG1.2	505810	
CD19	APC/Cyanine7	6D5	115530	
LIVE/DEAD			423106	
CD3	Brilliant Violet 421™	17A2	100228	
CD45R/B220	Brilliant Violet 650™	RA3-6B2	103241	
CD45	Brilliant Violet 785™	30-F11	103149	
CD19	FITC	6D5	115505	
CD45		I3/2.3	147710	
CD69	PE	H1.2F3	104508	
F4/80		BM8	123110	
Perforin		s16009a	154306	
CD3	PE/Cyanine7	17A2	100220	
Ly6G		1A8	127618	
CSF-1R(CD115)	PE/Dazzle™	AFS98	135527	
CD11c		N418	117348	
CD62L		MEL-14	104448	
TNF		MP6-XT22	506346	
CD8a	PerCP/Cy5.5	53-6.7	100734	
Ly6C		HK1.4	128011	
CD16/32	-	93	101302	
LIVE/DEAD	AmCyan		L34966	Thermo Fischer Scientific

Table S4. IHC primary antibodies anti-mouse

Antibody	Clone	Ordering #	Company
B220	RA3-6B2	553084	BD Biosciences
B220-Alexa Fluor®647	RA3-6B2	103226	Biolegend
CD11b	EPR1344	ab133357	Abcam
CD3	SP7	ab16669	Abcam
CD8	4SM15	14-0808-82	Invitrogen
CD8α-Alexa Fluor®488	EPR21769	ab237364	Abcam
Cleaved Caspase 3 (Asp175)	polyclonal	9661	Cell Signaling
Collagen type IV	CL50451AP-1	CL50451AP-1	Cedarlane
EpCAM-Brilliant Violet 421™	G8.8	118225	Biolegend
F4/80	BM8	123105	BioLegend
FCER1G	polyclonal	PA5-109716	Invitrogen (Thermo Fisher Scientific)
FCGR1	1	50086-R001	Sino Biological
Gp73	F-2	sc-365817	Santa Cruz Biotechnology
IgA	M18-254	553476	BD Pharmingen™
IgM	polyclonal	A 0425	DAKO
Ki67	SP6	RM-9106-S1	Thermo Fisher Scientific
Ly6C	ER-MP20	ab15627	Abcam
MHCII	M5/114.15.2	NBP1-43312	Novus Biologicals
P62	polyclonal	MBL-PM045	Biozol diagnostica
PDGFRβ	28E1	3169s	Cell Signaling Technology
Phospho-HCK(Tyr411)	polyclonal	orb184018	Biorbyt
Phospho-SYK(Tyr525)	polyclonal	PA5104904	Invitrogen (Thermo Fisher Scientific)
S100A4	polyclonal	810101	BioLegend

Table S5. Flow cytometry antibodies used for murine liver CD45^{+} sorted cells for subsequent scRNA-Seq

Liver CD45^{+} sorted cells for scRNA-Seq - flow cytometry antibodies				
Marker	**Fluorochrome**	**Clone**	**Ordering #**	**Company**
CD3e	Alexa Fluor® 488	145-2C11	557666	BD Pharmingen™
CD45	APC/Cyanine7	30-F11	557659	
CD19	FITC	1D3	553785	
NK1.1	PE	PK1136	553165	
Ly6G		1A8	551461	
TCRγδ		GL-3	12-5711-82	eBioscience™
CD4		RM4-5	12-0042-83	
TCRβ	PE/Cyanine7	H57-597	25-5961-82	
Hoechst 33258	eFluor™ 450	-	94403	Sigma-Aldrich

Table S6. Flow cytometry antibodies used for co-culture experiments with intestinal B cells and T cells

Co-culture small intestine anti-mouse flow cytometry antibodies				
Marker	**Fluorochrome**	**Clone**	**Ordering #**	**Company**
CD8α	APC	53-6.7	100712	Biolegend
CD25	PE	PC61.5	12-0251-81	eBioscience™
CD152 (CTLA-4)	PE/Cyanine7	UC10-4B9	25-1522-82	eBioscience™
CD279 (PD-1)	BUV737	RMP1-30	749306	BD Bioscience
CD69	FITC	H1.2F3	104506	Biolegend
CD186 (CXCR6)	Brilliant Violet 421™	SA051D1	151109	Biolegend
CD19	PerCP/Cyanine5.5	1D3	45-0193-82	eBioscience™
CD45R/B220	Brilliant Violet 711™	RA3-6B2	103255	Biolegend

Table S7. Patient clinical features of analysed histological samples (liver and jejunum)

Clinical features	N total (n= 54)	Count/mean ± SD
Age (mean ± SD)	54	50.6 ± 10.9
Sex	54	
Male		28
Female		26
BMI (mean ± SD)	51	40.3 ± 7.7
ALT (mean ± SD)	35	49.1 ± 28.7
NAS (mean ± SD)	53	3.5 ± 1.8
NAS score ≤ 2		16
NAS score ≥ 3		37
Fibrosis (mean ± SD)	51	1.8 ± 1.5
Fibrosis score (Kleiner) ≤ F2		30
Fibrosis score (Kleiner) F3/F4		21

Supplementary references

Author names in bold designate shared co-first authorship.

1. Tomura M, Yoshida N, Tanaka J, et al. Monitoring cellular movement in vivo with photoconvertible fluorescence protein "Kaede" transgenic mice. *Proc Natl Acad Sci U S A*. Aug 05 2008;105(31):10871-6. doi:10.1073/pnas.0802278105

2. Krebs CF, Paust HJ, Krohn S, et al. Autoimmune Renal Disease Is Exacerbated by S1P-Receptor-1-Dependent Intestinal Th17 Cell Migration to the Kidney. *Immunity*. 11 15 2016;45(5):1078-1092. doi:10.1016/j.immuni.2016.10.020

3. Pfister D, Núñez NG, Pinyol R, et al. NASH limits anti-tumour surveillance in immunotherapy-treated HCC. *Nature*. Apr 2021;592(7854):450-456. doi:10.1038/s41586-021-03362-0

4. Palm NW, de Zoete MR, Cullen TW, et al. Immunoglobulin A coating identifies colitogenic bacteria in inflammatory bowel disease. *Cell*. Aug 28 2014;158(5):1000-1010. doi:10.1016/j.cell.2014.08.006

5. Malehmir M, Pfister D, Gallage S, et al. Platelet GPIbα is a mediator and potential interventional target for NASH and subsequent liver cancer. *Nat Med*. 04 2019;25(4):641-655. doi:10.1038/s41591-019-0379-5

6. Wolf FA, Angerer P, Theis FJ. SCANPY: large-scale single-cell gene expression data analysis. *Genome Biol*. 02 06 2018;19(1):15. doi:10.1186/s13059-017-1382-0

7. Hänzelmann S, Castelo R, Guinney J. GSVA: gene set variation analysis for microarray and RNA-seq data. *BMC Bioinformatics*. Jan 16 2013;14:7. doi:10.1186/1471-2105-14-7

8. Virtanen P, Gommers R, Oliphant TE, et al. SciPy 1.0: fundamental algorithms for scientific computing in Python. *Nat Methods*. 03 2020;17(3):261-272. doi:10.1038/s41592-019-0686-2

9. Parekh S, Ziegenhain C, Vieth B, Enard W, Hellmann I. The impact of amplification on differential expression analyses by RNA-seq. *Sci Rep*. 05 09 2016;6:25533. doi:10.1038/srep25533

10. Macosko EZ, Basu A, Satija R, et al. Highly Parallel Genome-wide Expression Profiling of Individual Cells Using Nanoliter Droplets. *Cell*. May 21 2015;161(5):1202-1214. doi:10.1016/j.cell.2015.05.002

11. Love MI, Huber W, Anders S. Moderated estimation of fold change and dispersion for RNA-seq data with DESeq2. *Genome Biol*. 2014;15(12):550. doi:10.1186/s13059-014-0550-8

12. Heymann F, Hammerich L, Storch D, et al. Hepatic macrophage migration and differentiation critical for liver fibrosis is mediated by the chemokine receptor C-C motif chemokine receptor 8 in mice. *Hepatology*. Mar 2012;55(3):898-909. doi:10.1002/hep.24764

13. Valle-Noguera A, Gómez-Sánchez MJ, Girard-Madoux MJH, Cruz-Adalia A. Optimized Protocol for Characterization of Mouse Gut Innate Lymphoid Cells. *Front Immunol*. 2020;11:563414. doi:10.3389/fimmu.2020.563414

14. Hardy T, Wonders K, Younes R, et al. The European NAFLD Registry: A real-world longitudinal cohort study of nonalcoholic fatty liver disease. *Contemp Clin Trials*. Oct 9 2020;98:106175. doi:10.1016/j.cct.2020.106175

15. Kleiner DE, Brunt EM, Van Natta M, et al. Design and validation of a histological scoring system for nonalcoholic fatty liver disease. *Hepatology*. Jun 2005;41(6):1313-21. doi:10.1002/hep.20701

16. Govaere O, Cockell S, Tiniakos D, et al. Transcriptomic profiling across the nonalcoholic fatty liver disease spectrum reveals gene signatures for steatohepatitis and fibrosis. *Sci Transl Med*. Dec 2 2020;12(572)doi:10.1126/scitranslmed.aba4448

17. Bankhead P, Loughrey MB, Fernandez JA, et al. QuPath: Open source software for digital pathology image analysis. *Sci Rep*. Dec 4 2017;7(1):16878. doi:10.1038/s41598-017-17204-5

18. Ramachandran P, Dobie R, Wilson-Kanamori JR, et al. Resolving the fibrotic niche of human liver cirrhosis at single-cell level. *Nature*. 11 2019;575(7783):512-518. doi:10.1038/s41586-019-1631-3

19. Valle JW, Borbath I, Khan SA, et al. Biliary cancer: ESMO Clinical Practice Guidelines for diagnosis, treatment and follow-up. *Ann Oncol*. Sep 2016;27(suppl 5):v28-v37. doi:10.1093/annonc/mdw324

Supplementary figure legends

Fig. S1: B-cells deficiency and therapeutic B-cells depletion avoid hepatic immune cells activation and metabolic deregulation

(A) Summary Table Sindicating clinical data as follows: serological ALT values, cholesterol, hepatic triglycerides, NAS and phenotypic outcome for WT ND, CD-HFD and $JH^{-/-}$ CD-HFD mice. Unpaired T-test statistical analysis for: a) WT CD-HFD *vs* WT ND; b) $JH^{-/-}$ CD-HFD *vs* WT CD-HFD; and $JH^{-/-}$ CD-HFD *vs* WT ND (n≥4). **(B)** Weight development in male WT ND, CD-HFD and $JH^{-/-}$ CD-HFD mice (n=20). **(C)** Glucose tolerance test performed in WT ND, CD-HFD and $JH^{-/-}$ CD-HFD 9-month-old male mice (n=6). **(D)** Representative IHC for B220, CD3, F4/80, MHCII, P62, cleaved caspase 3, and PD1 quantification of the respective cells per mm^2 on liver sections of 6-month-old WT ND, CD-HFD and $JH^{-/-}$ CD-HFD (n=6). **(E)** Absolute quantification of flow cytometric analyses comparing 6-month-old WT ND, CD-HFD and $JH^{-/-}$ CD-HFD male mice (n=5) for hepatic $CD3^+$ cells and $CD8^+$ cells; and of **(F)** $CD19^+$ cells. **(G)** Clinical data summary Table Sfor 12-month WT ND, CD-HFD and $JH^{-/-}$ CD-HFD fed mice (n≥4). **(H)** Representative H&E liver sections of 12-month fed mice. **(I)** Clinical data summary Table Sfor controls and anti-CD20 treatment in WT CDHFD mice. Unpaired T-test statistical analysis for: a) WT CD-HFD *vs* WT ND; b) αCD20 CD-HFD *vs* WT CD-HFD; and αCD20 CD-HFD *vs* WT ND (n≥4). **(J)** Representative H&E staining of liver sections of 4-month (start of the depletion treatment) WT CD-HFD mice. **(K)** NAS evaluation on liver sections of 4-month WT CD-HFD mice (n=3). **(L)** Body weight of 6-month WT ND, control and αCD20-treated WT CD-HFD male mice (n=5). **(M)** Glucose tolerance test performed in 6-month male mice (n=5). **(N-P)** Absolute quantifications of flow cytometric analyses comparing control and αCD20-treated WT CD-HFD male mice (n≥3) of **(N)** spleen $CD19^+$ and $CD20^+$ cells, **(O)** blood $CD19^+$ and $CD20^+$ cells, **(P)** liver $CD3^+$ cells and liver $CD8^+$ cells. **(Q)** Representative liver IHC staining for B220, CD3, F4/80, MHCII and P62 quantification of the respective cells per mm^2 on liver sections of 6-month-old WT ND, WT CD-

HFD and αCD20-treated WT CD-HFD mice (n=6). **(R)** Real-time PCR analysis for lipid metabolism genes on mRNA isolated from WT ND and CD-HFD and $JH^{-/-}$ CD-HFD livers (n=6). **(S)** Heatmap representing hierarchical clustering analysis of lipid metabolites significantly altered (autoscaled abundance), as evaluated in male mice (n≥3). All data are presented as mean ± SEM. Statistical analyses were performed using unpaired T-test or ANOVA. Displayed scale bar represents 100 µm.

Fig. S2: Intestinal B-cells suffice to induce hepatic inflammation and metabolic dysregulation.

(A) Summary Table Sindicating clinical data as follows: serological ALT values, cholesterol, hepatic triglycerides, NAS and phenotypic outcome for WT ND, CD-HFD and µMT CD-HFD mice. Unpaired T-test statistical analysis for: a) WT CD-HFD *vs* WT ND; b) µMT CD-HFD *vs* WT CD-HFD; and µMT CD-HFD *vs* WT ND (n≥4). **(B)** Weight development in male WT ND, CD-HFD and µMT CD-HFD mice (n=20). **(C)** Glucose tolerance test performed in WT ND, CD-HFD and µMT CD-HFD 6-month-old male mice (n=6). **(D)** Representative Ki67 staining on spleen sections of WT and µMT CD-HFD male mice. **(E)** Quantifications of flow cytometric analyses showing percentages of small intestine lamina propria $CD20^+$ and IgA^+ cells, comparing µMT and $JH^{-/-}$ CD-HFD mice (n=4). **(F)** Representative B220 staining on spleen sections of WT and µMT CD-HFD male mice. **(G)** Representative IgA staining of small intestine sections of 6-month µMT CD-HFD male mouse (upper row: scale bar 200 µm, bottom row scale bar: 100 µm). **(H)** IgM and IgG2b levels of small intestinal tissues measured by E.L.I.S.A. in WT ND, and in WT, $JH^{-/-}$ and µMT CD-HFD male mice. **(I, J)** Percentages of $CD19^+$, $B220^+$ and IgA^+ cells, of **(I)** caecum and **(J)** colon (n=3). **(K)** Percentages of IgA^+ coated bacteria from faecal homogenates of WT ND and WT, $JH^{-/-}$ and µMT mice on CD-HFD for 6 months. **(L)** Representative IHC images for B220, CD3, F4/80 and MHCII on liver sections of 6-month-old

WT ND, WT CD-HFD and μMT CD-HFD and quantification of the respective cells per mm^2 (n=6). **(M)** Quantifications of liver flow cytometric analyses comparing 6-month WT ND, CD-HFD and μMT CD-HFD male mice for $CD3^+$ and $CD8^+$ cells (n=4). **(N)** Real-time PCR analysis for lipid metabolism genes on mRNA isolated from WT ND and CD-HFD and μMT CD-HFD livers (n=4). **(O)** Clinical data summary Table Sfor 12-month WT ND and WT CD-HFD mice and for μMT CDHFD mice. Unpaired T-test statistical analysis for: a) WT CD-HFD *vs* WT ND; b) μMT CD-HFD *vs* WT CD-HFD; and μMT CD-HFD *vs* WT ND (n≥4). **(P)** Representative H&E staining of liver sections derived from 12-month-old WT and μMT male mice. **(Q)** Treatment scheme for the B-cell depleted μMT CD-HFD male mice (n=5). **(R)** Representative H&E staining of liver sections and NAS evaluation of 4-month WT and μMT CD-HFD male mice (n=3). **(S)** Clinical data summary Table Sfor controls and for anti-CD20 treatment in μMT CDHFD mice. Unpaired T-test statistical analysis for: a) WT CD-HFD *vs* WT ND; b) αCD20 μMT CD-HFD *vs* WT CD-HFD; and αCD20 μMT CD-HFD *vs* WT ND (n≥4). **(T)** Body weight values at 6-month time point of μMT CD-HFD and of αCD20-treated μMT CD-HFD mice. **(U)** Normalized to Mode histogram showing $CD20^+IgA^+$ cells in small intestine lamina propria of μMT CD-HFD and μMT CD-HFD αCD20-treated mice. **(V)** Upper panel, representative IHC images and quantifications per mm^2 on liver sections of μMT CD-HFD and μMT CD-HFD αCD20-treated livers; lower panel quantification of the respective cells per mm^2 for CD3, F4/80, MHCII, P62 and cleaved caspase 3 (n≥4). **(W)** Absolute quantifications of liver flow cytometric analyses comparing μMT CD-HFD and μMT CD-HFD αCD20-treated, for $CD3^+$ and for $CD8^+$ cells (n≥4). All data are presented as mean ± SEM. Statistical analyses were performed using unpaired T-test or ANOVA. Displayed scale bar represents 100 μm.

Fig. S3: Intestinal B-cells are hyperactivated in NASH and require antigen presentation receptors to drive the disease.

All data represent small intestine. **(A-H)** Percentages of liver flow cytometric analysis of WT ND, WT CD-HFD and in μMT CD-HFD mice(n≥4): **(A)** $CD20^{+}CXCXR4^{+}$ cells, **(B)** IgA^{+} cells, **(C)** $IgA^{+}B220^{-}CD20^{-}$ $CXCR4^{-}$ cells, **(D)** $CD8^{+}CD44^{+}$ cells, **(E)** $CD8^{+}PD1^{+}$ cells, all of $CD45^{+}$ cells. **(G, H)** Percentages of $CD44^{+}$ cells or $PD1^{+}$ cells of $CD8^{+}$ T cells. **(I)** Representative high-resolution confocal microscopy and 3D reconstruction images of small intestine lamina propria staining for $B220^{+}$ and $CD8^{+}$ cells, and **(J)** quantification of clusters found in villi of $B220^{+}/CD8^{+}$ interacting cells, of WT ND and WT CD-HFD mice (n=3, with n=8 FOV each mouse). **(K)** Heatmaps showing Z-scores of common genes significantly deregulated in WT ND, WT CD-HFD and μMT CD-HFD male mice RNA-Seq analysis of small intestine lamina propria $CD20^{+}$ sorted cells (on the right), involved in immune network for IgA production, B-cell activation and differentiation, metabolic process (n≥4). **(L)** Heatmaps displaying common genes from intestinal $B220^{+}$ sorted cells RNA-Seq involved in the immune system and metabolic process (n=3). **(M)** Flow cytometry analysis of activated $CD8^{+}$ cells after in vitro co-culture of isolated intestinal B cells from WT ND or WT CD-HFD with OT-1 T cells (n=4).

All data are presented as mean ± SEM. Statistical analyses were performed using unpaired T-test or ANOVA. Displayed scale bar represents 100 μm.

Fig. S4: Mouse model for absent secretion of immunoglobulin displays normal B-cells response but does not form clusters with T-cells in small intestine.

(A) Disease score measure for 16-days of Experimental Autoimmune Encephalomyelitis (EAE) in WT control and IgMi mice. **(B)** Splenic interleukin-2 levels (pg/ml) after EAE-immunization with MOG_{35-55} or with medium as control, of WT and IgMi mice (n=3). **(C)** Summary Table Sindicating clinical data as follows: serological ALT values, cholesterol, hepatic triglycerides, NAS and phenotypic outcome for WT ND, CD-HFD and IgMi CD-HFD mice. Unpaired T-test statistical analysis for: a) WT CD-HFD *vs* WT ND; b) IgMi CD-HFD *vs* WT CD-HFD; and IgMi CD-HFD *vs* WT ND (n≥4). **(D)** On the left, representative IHC images for B220, CD3, F4/80,

MHCII, P62 and cleaved caspase 3 staining; on the right, their quantification for WT ND, WT CD-HFD and IgMi CD-HFD groups (n≥5). **(E)** Liver flow cytometric analyses displaying quantifications of liver total $CD3^+$ cells or total $CD8^+$ cells of WT ND, WT CD-HFD and IgMi CD-HFD groups (n=5). **(F)** High-resolution confocal microscopy images of small intestine lamina propria staining for $B220^+$ cells and $CD8^+$ cells and quantification of $B220^+/CD8^+$ interacting cells forming clusters in villi of WT controls and IgMi CD-HFD mice small intestines. **(G)** Representative IHC images and quantification of small intestine pospho-SYK positive immune cells (per mm^2) (n≥3). All data are presented as mean ± SEM. Statistical analyses were performed using unpaired T-test. Displayed scale bar represents 100 µm.

Fig. S5: Increase of profibrogenic MoMFs is CD-HFD specific and requires FcR signalling

(A) Sirius red staining quantification from livers of 6-months WT ND and $JH^{-/-}$, WT αCD20-treated, µMT, IgMi, AIDg23s mice under CD-HFD (n≥4). **(B)** Representative collagen-IV stained liver sections of the groups mentioned above. **(C)** PDGFRβ staining on liver sections of the aforementioned mouse groups, with the corresponding quantification per mm^2 (n≥4). **(D)** Representative Sirius red (upper row) staining and quantification, and collagen-IV (bottom row) staining on liver sections for 6-months WT, µMT αCD20-treated, $IgA^{-/-}$ and $AID^{-/-}$ mice under CD-HFD (n≥4). **(E)** IgA serological levels (µg/ml) measured via E.L.I.S.A in 6-months WT ND and $JH^{-/-}$, WT αCD20-treated, µMT, IgMi, AIDg23s under CD-HFD (n≥4). **(F)** On the left, IgA serological levels (µg/ml) were measured via E.L.I.S.A in 6-months WT, µMT αCD20-treated, $IgA^{-/-}$ and $AID^{-/-}$ mice under CD-HFD (n≥4). On the right, correlation plot indicating serological IgA and Sirius red positivity in WT, $IgA^{-/-}$ and $AID^{-/-}$ mice under CD-HFD. **(G)** Real-time PCR analysis for fibrosis-related genes on mRNA isolated from 6-month WT ND and $JH^{-/-}$, µMT, WT αCD20-treated, AIDg23s, IgMi, and $FcR\gamma^{-/-}$ mice under CD-HFD (n≥2). Statistical analysis of qRT-PCR heatmap, indicating in black asterisks the significance of groups under CD-HD

versus WT ND, and in green asterisks, the significance of groups under CD-HD versus WT CD-HFD. **(H)** Hydroxyproline levels (µg/g) of livers from 6-month WT ND and µMT, WT αCD20-treated, AIDg23s, IgMi, and FcRγ$^{-/-}$ mice under CD-HFD (n≥3). **(I)** Summary Table Sindicating clinical data as follows: serological ALT values, cholesterol, hepatic triglycerides, NAS and phenotypic outcome for WT CD-HFD and FcRγ$^{-/-}$ CD-HFD mice. Unpaired T-test statistical analysis for: a) FcRγ$^{-/-}$ CD-HFD *vs.* WT CD-HFD (n≥4). **(J)** Representative Sudan red staining of liver sections and hepatic triglycerides quantification of WT and FcRγ$^{-/-}$ on CD-HFD mice (n=5). **(K)** Liver flow cytometry analysis quantifications of total CD3^{+} and CD19^{+} cell populations, CD8^{+} cells, CD8^{+}CD62L^{+} and CD8^{+}CD62L^{-} cells, CD8^{+}TNF^{+} cells, CD8^{+}IFNγ^{+} cells. **(L)** Representative IHC images of liver sections per mm^2 and quantifications for CD3, B220, F4/80 and MHCII staining of WT and FcRγ$^{-/-}$ on CD-HFD mice (n=4). **(M)** Representative IHC images of Ly6C staining or **(N)** S100A4 staining of liver sections and quantification of positive cells per mm^2 for WT ND and WT, WT αCD20- treated, µMT, AIDg23s and FcRγ$^{-/-}$ mice under CD-HFD (n≥3). **(O)** Treatment scheme for the *in vitro* experiments using 12-weeks WT male mice-isolated BMDMs treated with serum of 6-month WT ND/ fibrotic WT CD-HFD/ µMT CD-HFD mice; in addition is displayed the treatment with fibrotic WT CD-HFD serum on 12-weeks FcRγ$^{-/-}$ male mice-isolated BMDMs. **(P)** Treatment scheme for the CCl_4 experiments with one-dose injection and sacrificing mice after 36 hours. The harvested livers were analyzed by flow cytometry, and the isolated BMDMs were used for transmigration *in vitro* assay using CCL2 cytokine and subsequent flow cytometry experiments. **(Q)** Flow cytometric analysis quantification for absolute number and percentages of CD45^{+}Ly6G^{-}Cd11c^{-} F4/80^{+}CD11b^{+}Ly6C^{+}, of transmigrated cells treated or not with CCL2, from BMDMs isolated from WT or FcRγ$^{-/-}$ mice (n=4), with or without CCl_4 treatment. **(R)** Absolute quantification of hepatic CD45^{+}Ly6G^{-}Cd11c^{-}F4/80^{+}CD11b^{+}Ly6C^{+} of WT or FcRγ$^{-/-}$ mice treated or not with CCl_4. **(S)** Measured CCL2 levels (pg/ml) livers and sera of 6-months WT ND, WT CD-HFD, µMT CD-

HFD, AIDg23s CD-HFD and FcRγ$^{-/-}$ CD-HFD mice. **(S)** Representative H&E, Sirius red staining, and NAS evaluation of liver section from 5-month-old male mice under ND, WD or CDA-HFD (n=4). Serological IgA values (µg/ml) (n≥4). **(T)** Values of mRNA expression levels of MoMFs markers in scRNA-Seq 10X analysis. **(U)** On the left, values of mRNA expression levels of genes involved in FcRγ signalling; on the right, MoMFs clusters visualization UMAP plots (in ND, WD and CDA-HFD) and plot indicating FcRγ signalling expression score per condition (in MoMFs clusters). Below are shown major FcRγ signalling genes; MoMFs clusters 9 and 17 percentages, and double-violin plots of *Fos* gene (n≥2), all from scRNA-Seq 10X analysis. **(V)** Representative images of immunofluorescence triple staining for FCER1G/CD11b/Ly6C on liver sections of WT ND, WT CD-HFD and FcRγ$^{-/-}$ mice. **(W)** Quantification of triple and double staining (CD11b/Ly6C) in WT ND, WT CD-HFD and FcRγ$^{-/-}$ mice (n=4), and quantification of triple staining in WT ND and WT, WT αCD20-treated, µMT, IgMi, AIDg23s mice under CD-HFD (n≥3). **(X)** Representative images of IHC staining for FCGR1, p-HCK on liver sections of WT ND and WT, JH$^{-/-}$, WT αCD20-treated, µMT, IgMi, AIDg23s mice under CD-HFD. All data are presented as mean ± SEM. Statistical analyses were performed using unpaired T-test. The scale bar represents 100 µm.

Fig. S6: Germ-free mice develop NASH under CD-HFD, acerbated by B-cells.

(A) Body weight development (n=6). **(B)** Glucose tolerance test assessed on 6-months GF WT ND and GF WT CD-HFD (n=4). **(C)** Quantifications of liver flow cytometric analyses comparing 6-month GF ND, and GF CD-HFD for total CD19^{+} cells and total CD3^{+} cells (n=4). **(D)** Treatment scheme for the B-cell depleted GF WT CD-HFD male mice. **(E)** Serological ALT and cholesterol levels in 4-month (start of the depletion treatment) GF ND and GF CD-HFD male mice (n≥6). **(F)** Representative B220 staining of spleen sections of WT control and αCD20-treated CD-HFD mice. **(G)** Summary Table Sindicating clinical data as follows:

serological ALT values, cholesterol, hepatic triglycerides, NAS and phenotypic outcome for germ-free (GF) WT ND and GF CD-HFD. Unpaired T-test statistical analysis for: a) GF CD-HFD *vs* GF ND; b) αCD20 GF CD-HFD *vs* GF CD-HFD (n≥4). **(H)** Representative H&E staining of liver sections derived from GF WT CD-HFD untreated or treated with αCD20. **(I)** Representative Sudan red staining, and **(J)** quantification (n=5). **(K)** Flow cytometry quantification of hepatic total CD8+ cells, total $CD8^+CD62L^+$ and $CD8^+CD62L^-$ cells, total and $CD8^+perforin^{high}$ and $CD8^+TNF^+$ cells, comparing GF CD-HFD and GF CD-HFD αCD20-treated groups (n=4). Displayed below, absolute quantification of liver flow cytometric analyses of $CD19^+$ cells or $CD3^+$ cells; normalized to Mode histogram of $CD20^+$ cells of $CD45^+$ cells in pancreatic WT control and αCD20-treated CD-HFD groups; and percentages of $CD45^+$ cells of $CD20^+CD19^+$ cells comparing GF CD-HFD and αCD20 GF CD-HFD (n=4). **(L)** Representative IHC images of liver sections and quantifications per mm^2 for B220, CD3, F4/80 and MHCII staining of GF ND and GF αCD20-treated CD-HFD mice (n=5). All data are presented as mean ± SEM. Statistical analyses were performed using unpaired T-test or ANOVA. The scale bar represents 100 μm.

Fig. S7: Fibrosis does not associate with increased Kupffer cells but rather with SAMacs, which display upregulated FcRγ signalling

(A) Representative IHC images showing jejuna p-SYK positive immune cells (per mm^2) (n≥5). **(B)** Serological measurement of IgA, IgG and IgM levels in NAFLD patients divided in two subgroups (F0-F2 and F3-F4) based on fibrosis score (Brunt/Kleiner scoring) (n≥14 each group, total n=33). **(C)** Correlation of IgA levels (g/L) with NAS in NAFLD patients (n=639). **(D)** Gene expression correlation of *FCER1G* against *CCR2,* or against *S100A4*, in the overall NAFLD patient cohort (n=206). Correlations are performed using normalized reads, corrected for sex and batch effect. **(E)** Serological ALT measurement of obese patients (body mass index, BMI≥30) treated with rituximab for rheumatoid arthritis (n=15), and on the right are

displayed only the responders (n=11 out of 15). **(F)** Correlation plot of IgA serological levels with portal tract or parenchymal $CD8^+$ cells, or **(G)** correlation of IgA with portal tract or parenchymal $PD1^+$ cells (n=54). **(H)** IHC representative images of FCER1G, CCR2 and S100A4 in NAFLD patients with absent/very low fibrosis (F0/F1) and high fibrosis (F3) at low magnification. **(I)** Representative IF images for profibrogenic macrophages with FCER1G/S100A4/DAPI markers of liver sections from patients with NAFL, NASH-F2, and NASH-F4. **(J)** Representative IF for phospho-SYK/CD20/CD8 on jejunum sections of NAFL and NASH patients**. (K)** Clustermap of 496 common genes between the human and mouse scRNA-Seq datasets, showing ranked mean expression per liver $CD45^+$ cell group (SAMacs, Not SAMacs, MoMFs and Not MoMFs). **(L)** Heatmap showing gene expression values (log values) of significantly different FcRγ signalling-related genes in healthy and cirrhotic livers from scRNA-Seq analysis (n≥5). All data are presented as mean ± SEM. Statistical analyses were performed using unpaired T-test. The scale bar for IHC represents 100 μm, and for immunofluorescence 50 μm.

A

Group	Statistics	Serum ALT (U/L)	Serum Cholesterol (mg/dL)	Hepatic triglycerides (µg/mg tissue)	NAS	Outcome
WT ND 6M	Mean value	34.22	101.6	26.46	0.25	healthy liver, normal body weight
	SEM	±3.378	±7.195	± 4.122	± 0.164	
	N	9	8	5	8	
WT CD-HFD 6M	Mean value	178.9	271.6	121.8	5.125	NASH, obesity
	SEM	±17.394	±7.187	± 21.63	± 0.350	
	N	9	10	5	8	
	P-value[a]	<0.0001	<0.0001	0.0025	< 0.0001	
JH$^{-/-}$ CD-HFD 6M	Mean value	42.33	121.5	45.16	1	healthy liver, ↑body weight
	SEM	±5.183	±3.033	± 8.635	± 0.327	
	N	9	10	5	8	
	P-value[b]	<0.0001	<0.0001	0.011	< 0.0001	
	P-value[c]	0.2083	0.0141	0.0865	0.0596	

B

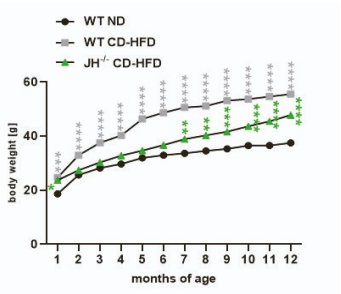

C

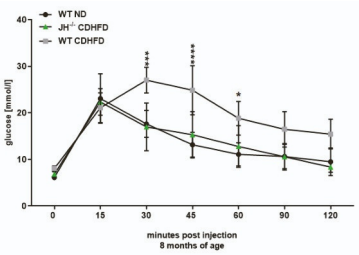

D

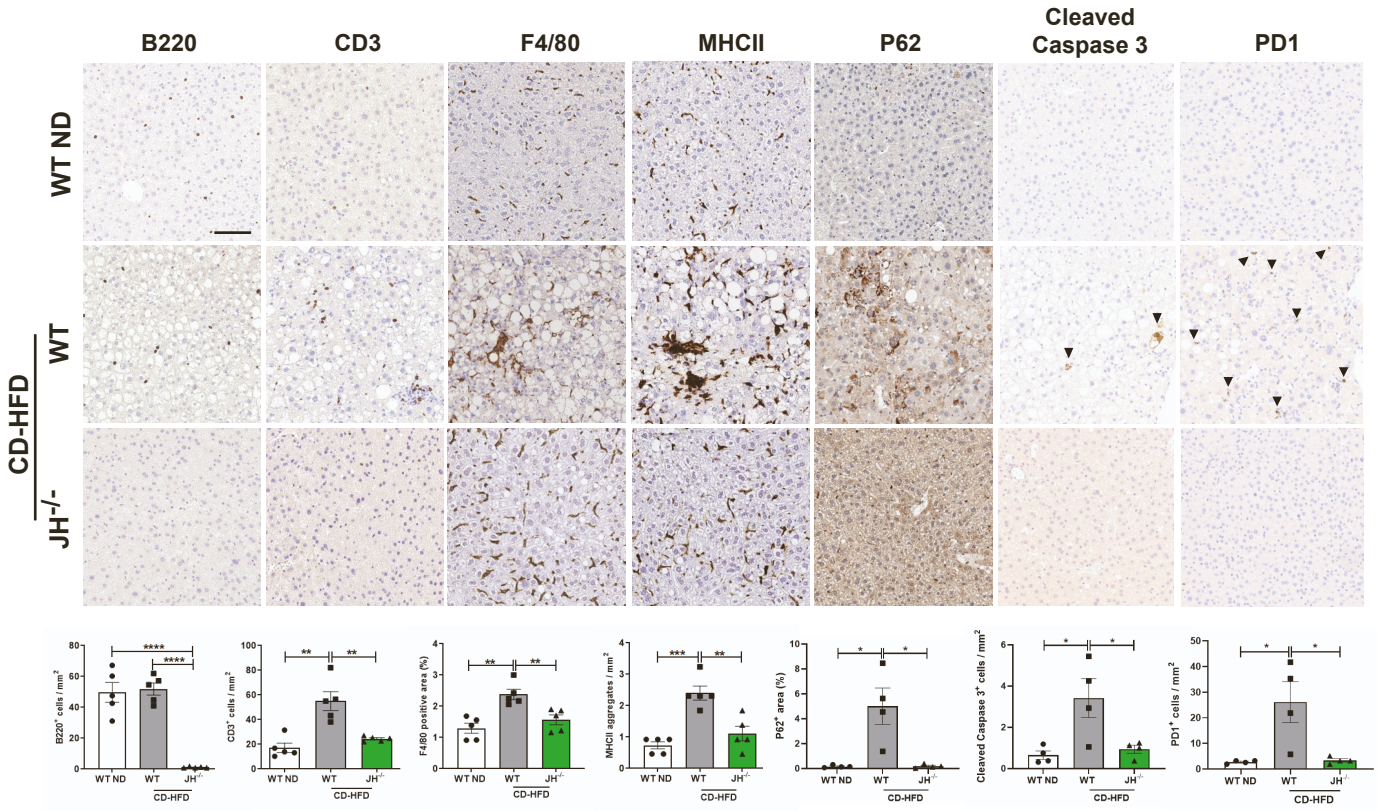

E

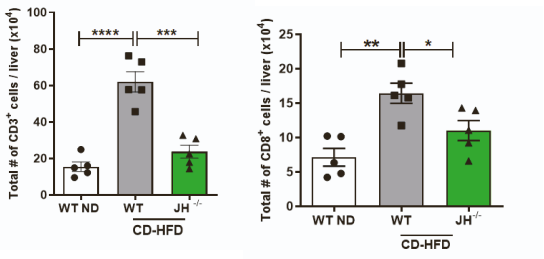

F

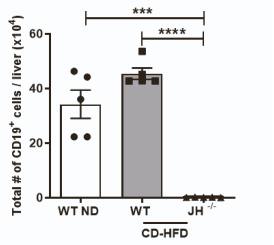

G

Group	Statistics	Serum ALT (U/L)	Serum Cholesterol (mg/dL)	Hepatic triglycerides (µg/mg tissue)	NAS	Outcome
WT ND 12M	Mean value	45	135.2	59.8	0.5	healthy liver, normal body weight
	SEM	±2.366	±5.802	± 2.864	±0.288	
	N	10	9	5	4	
WT CD-HFD 12M	Mean value	183.5	254.7	181.4	6.5	NASH, obesity
	SEM	±17.869	±12.776	± 20.30	±0.288	
	N	10	10	5	< 0.0001	
	P-value[a]	<0.0001	<0.0001	0.0003	4	
JH$^{-/-}$ CD-HFD 12M	Mean value	44.71	186.7	55.68	2.5	healthy liver, obesity
	SEM	±4.258	±20.745	± 9.990	±0.645	
	N	10	10	5	4	
	P-value[b]	<0.0001	0.012	0.0005	0.0013	
	P-value[c]	0.9532	0.036	0.7018	0.03	

H

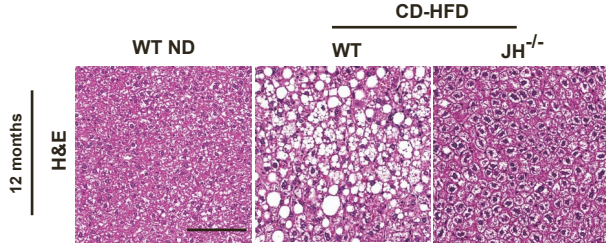

Figure S1

I

Group	Statistics	Serum ALT (U/L)	Serum Cholesterol (mg/dL)	Hepatic triglycerides (µg/mg tissue)	NAS	Outcome
WT ND 6M	Mean value	41.76	N/A	33.86	0.4	healthy liver, normal body weight
	SEM	±4.064		± 2.004	± 0.245	
	N	5		3	5	
WT CD-HFD 6M (control)	Mean value	176	267.2	145.5	5.8	NASH, HCC, obesity
	SEM	±7.162	±18.340	± 13.13	± 0.200	
	N	5	5	5	5	
	P-value[a]	<0.0001	N/A	0.0007	< 0.0001	
αCD20 WT CD-HFD 6M	Mean value	40.1	101.7	43.57	2	healthy liver, ↓steatosis, obesity
	SEM	±7.372	±10.032	± 7.051	± 0.547	
	N	5	5	5	5	
	P-value[b]	<0.0001	0.0007	< 0.0001	0.0002	
	P-value[c]	0.8405	N/A	0.3818	0.0285	

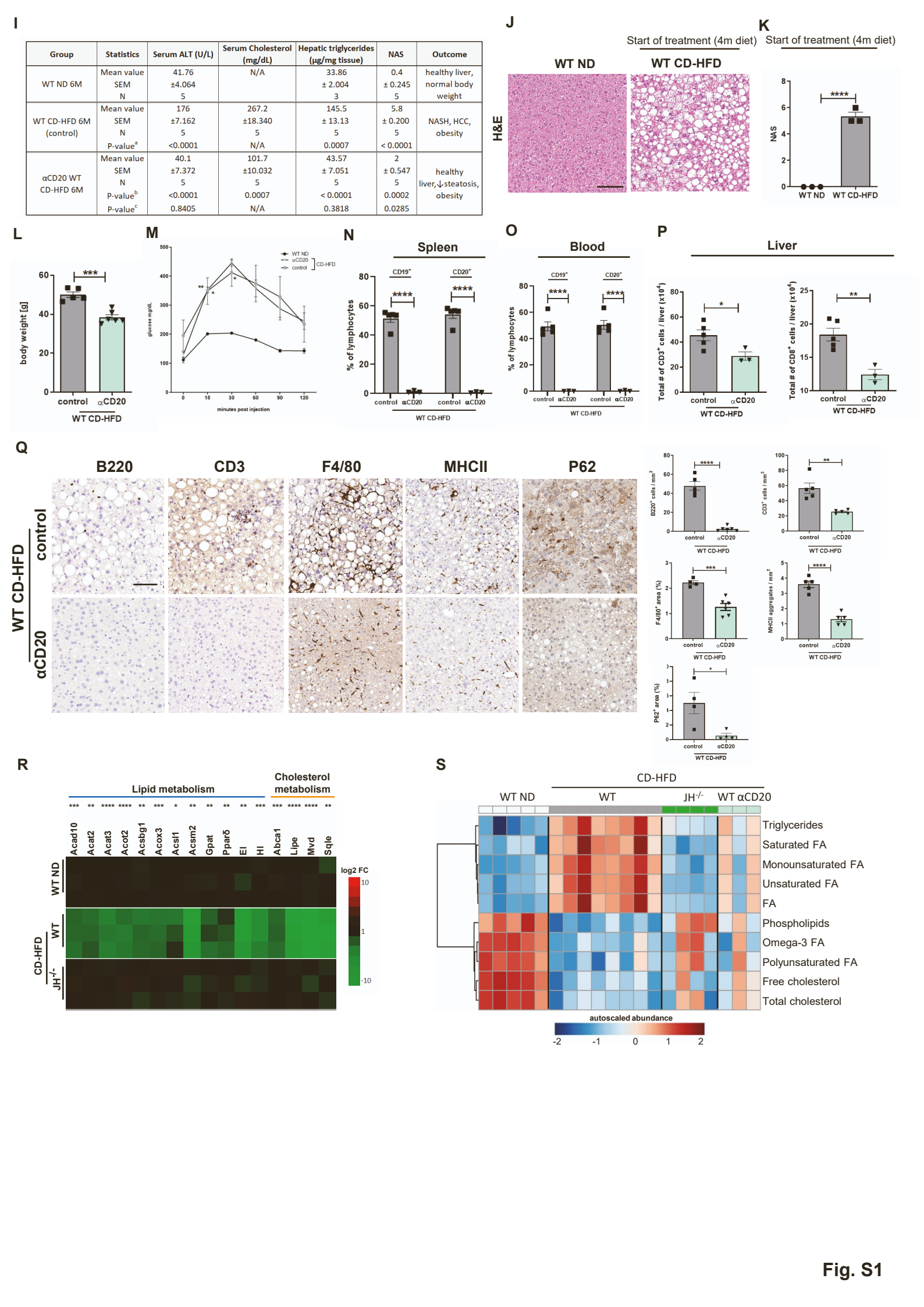

Fig. S1

A

Group	Statistics	Serum ALT (U/L)	Serum Cholesterol (mg/dL)	Hepatic triglycerides (µg/mg tissue)	NAS	Outcome
WT ND 6M	Mean value	35.45	101.6	16.83	0.3333	healthy liver, normal body weight
	SEM	±3.116	±7.195	± 0.718	± 0.211	
	N	8	8	5	6	
WT CD-HFD 6M	Mean value	122.5	205.5	137.9	5.833	NASH, obesity
	SEM	±11.165	±24.642	± 16.56	± 0.164	
	N	8	8	5	6	
	P-value[a]	<0.0001	0.0012	< 0.0001	< 0.0001	
µMT CD-HFD 6M	Mean value	136.1	242	156.6	4.833	NASH, obesity
	SEM	±30.712	±9.945	± 22.22	± 0.307	
	N	7	6	5	6	
	P-value[b]	0.6658	0.2468	0.5196	0.0169	
	P-value[c]	0.0039	<0.0001	0.0002	< 0.0001	

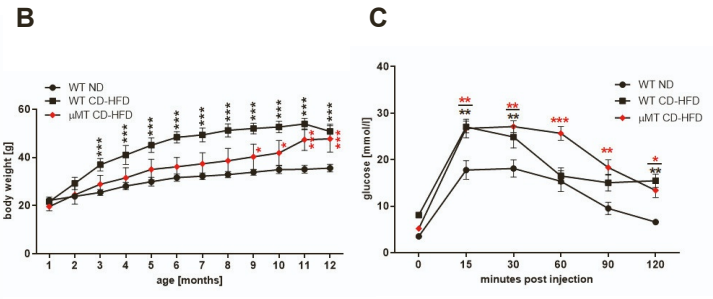

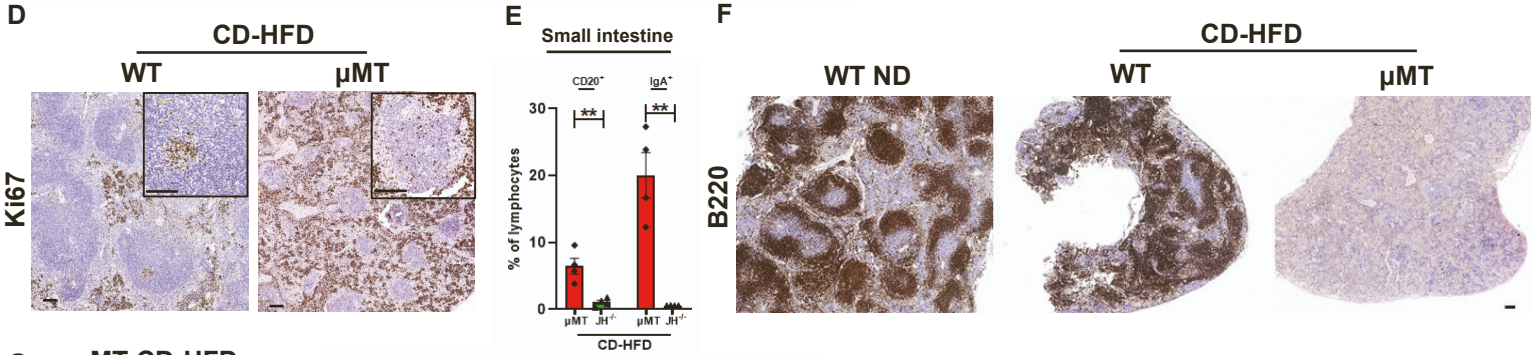

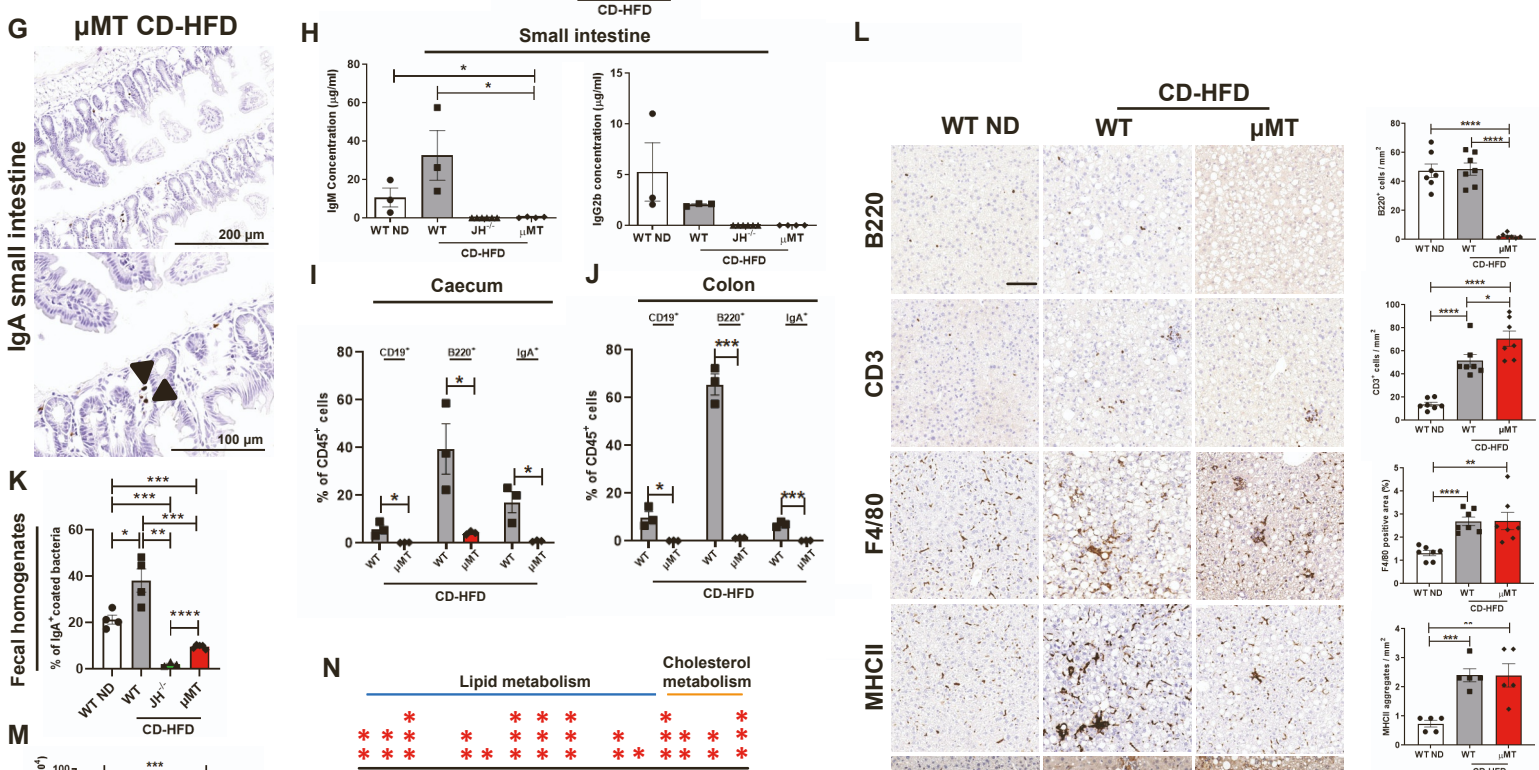

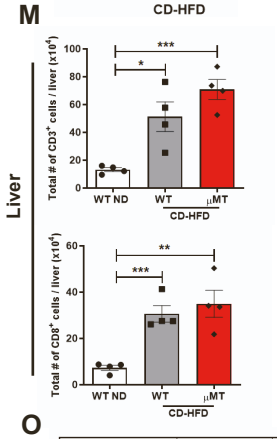

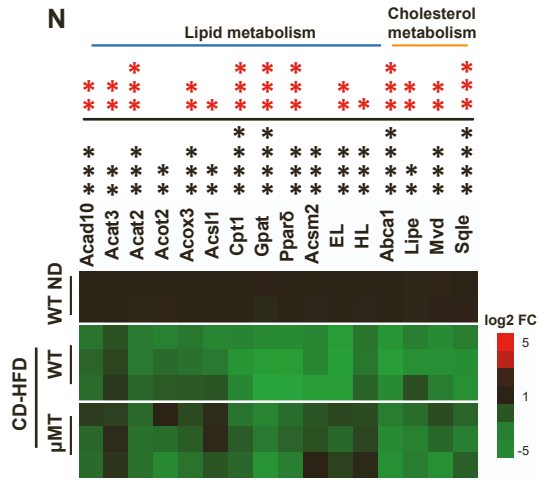

O

Group	Statistics	Serum ALT (U/L)	Serum Cholesterol (mg/dL)	Hepatic triglycerides (µg/mg tissue)	NAS	Outcome
WT ND 12M	Mean value	46	135.2	57.38	0.6	healthy liver, normal body weight
	SEM	±3.688	±5.802	± 3.01	± 0.245	
	N	6	9	5	5	
WT CD-HFD 12M	Mean value	204.7	213.1	189.3	6.2	NASH, HCC, obesity
	SEM	±21.600	±20.571	± 20.4	± 0.2	
	N	6	9	5	5	
	P-value[a]	<0.0001	0.0022	0.0002	< 0.0001	
µMT CD-HFD 12M	Mean value	201.2	189.8	181.5	5.571	NASH, ↓HCC obesity
	SEM	±26.190	±9.1678	± 9.843	± 0.202	
	N	6	9	5	7	
	P-value[b]	0.9214	0.3157	0.7413	0.0579	
	P-value[c]	0.0002	0.0001	< 0.0001	< 0.0001	

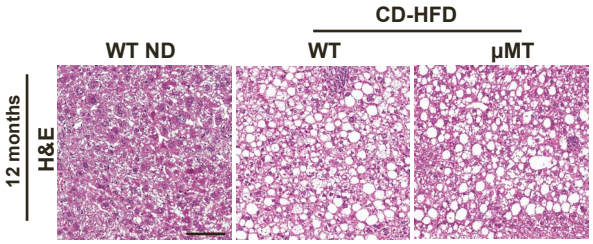

Fig. S2

Q

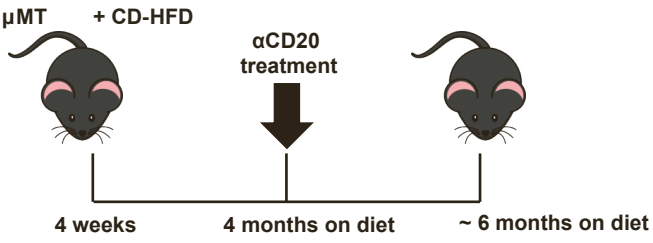

R

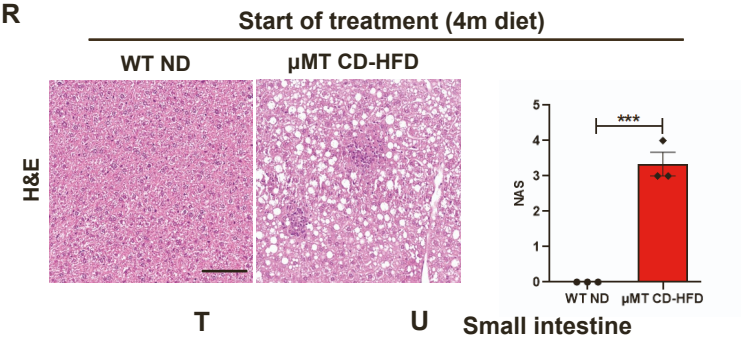

S

Group	Statistics	Serum ALT (U/L)	Serum Cholesterol (mg/dL)	Hepatic triglycerides (µg/mg tissue)	NAS	Outcome
WT ND 6M	Mean value	37.3	N/A	20.67	0.75	healthy liver, normal body weight
	SEM	±2.557		± 2.693	± 0.25	
	N	4		4	4	
µMT CD-HFD 6M (control)	Mean value	158.9	201.7	175.6	5.25	NASH, obesity
	SEM	±14.178	±2.333	± 14.84	± 0.25	
	N	4	4	4	4	
	P-value[a]	0.0002	N/A	< 0.0001		
αCD20 µMT CD-HFD 6M	Mean value	44.45	189	43.3	1.75	healthy liver, obesity
	SEM	±1.613	±1.915	± 16.64	± 0.25	
	N	4	4	4	4	
	P-value[b]	0.0002	0.0031	0.001	< 0.0001	
	P-value[c]	0.0559	N/A	0.2279	0.03	

T

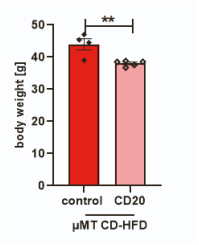

U

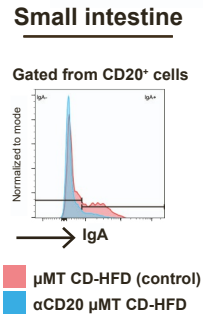

V

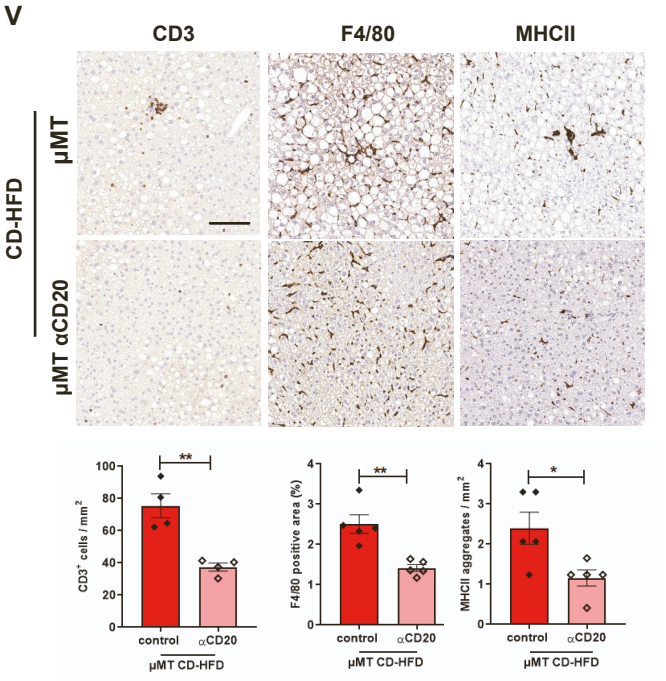

W

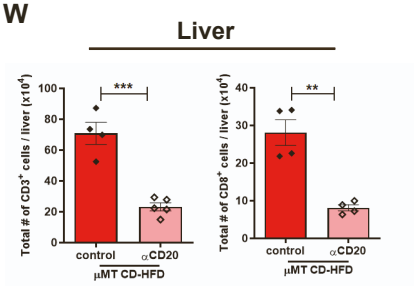

Fig. S2

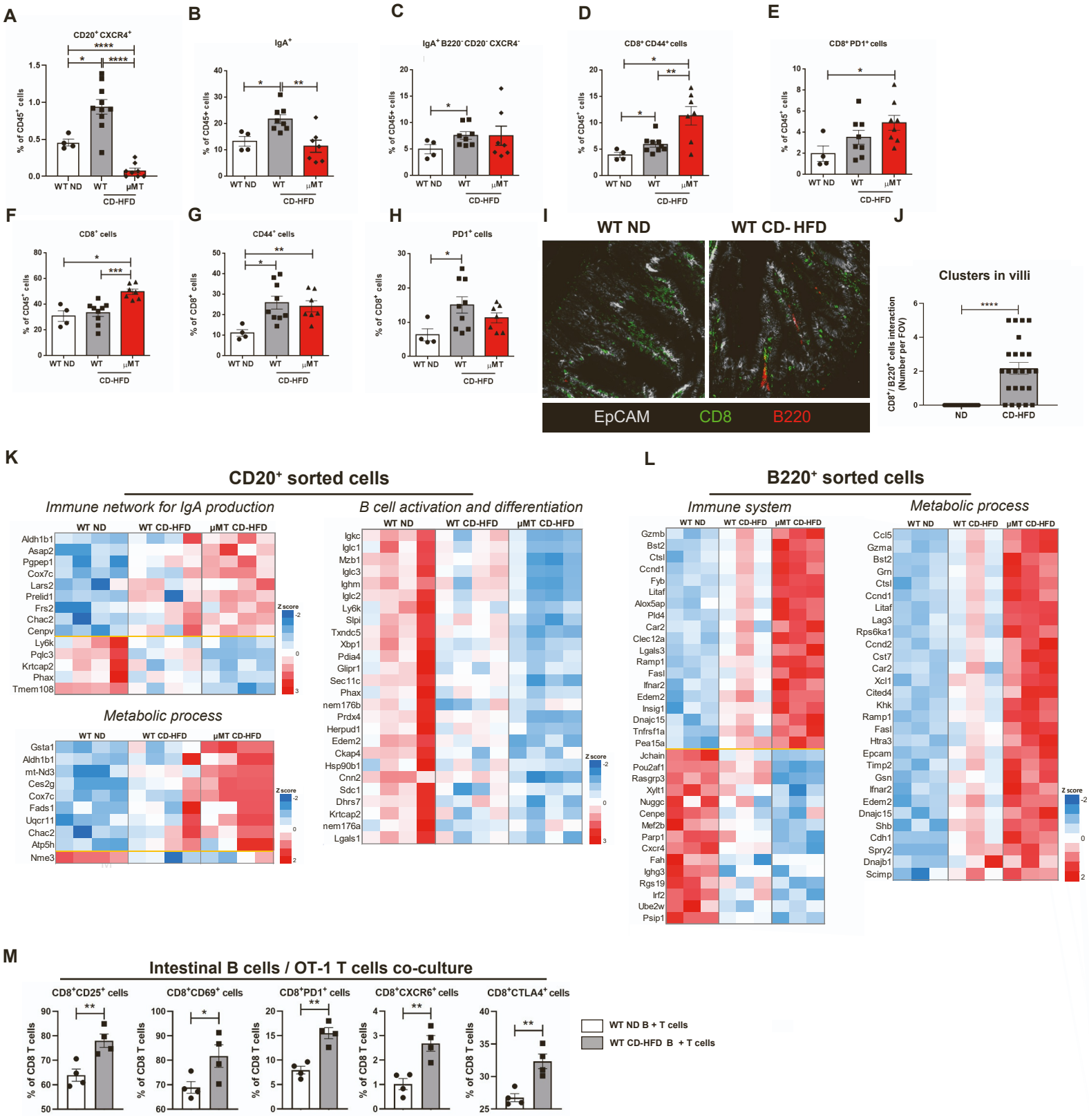
A
CD20+ CXCR4+
% of CD45+ cells
WT ND
WT
µMT
CD-HFD
B
IgA+
C
IgA+ B220- CD20- CXCR4-
D
CD8+ CD44+ cells
E
CD8+ PD1+ cells
F
CD8+ cells
% of CD45+ cells
G
CD44+ cells
% of CD8+ cells
H
PD1+ cells
I
WT ND
WT CD- HFD
EpCAM
CD8
B220
J
Clusters in villi
CD8+/B220+ cells interaction (Number per FOV)
ND
CD-HFD
K
CD20+ sorted cells
Immune network for IgA production
WT ND
WT CD-HFD
µMT CD-HFD
Aldh1b1
Asap2
Pgpep1
Cox7c
Lars2
Prelid1
Frs2
Chac2
Cenpv
Ly6k
Pqlc3
Krtcap2
Phax
Tmem108
Z score
B cell activation and differentiation
Igkc
Iglc1
Mzb1
Iglc3
Ighm
Iglc2
Ly6k
Slpi
Txndc5
Xbp1
Pdia4
Glipr1
Sec11c
Phax
nem176b
Prdx4
Herpud1
Edem2
Ckap4
Hsp90b1
Cnn2
Sdc1
Dhrs7
Krtcap2
nem176a
Lgals1
Metabolic process
Gsta1
Aldh1b1
mt-Nd3
Ces2g
Cox7c
Fads1
Uqcr11
Chac2
Atp5h
Nme3
L
B220+ sorted cells
Immune system
Gzmb
Bst2
Ctsl
Ccnd1
Fyb
Litaf
Alox5ap
Pld4
Car2
Clec12a
Lgals3
Ramp1
Fasl
Ifnar2
Edem2
Insig1
Dnajc15
Tnfrsf1a
Pea15a
Jchain
Pou2af1
Rasgrp3
Xylt1
Nuggc
Cenpe
Mef2b
Parp1
Cxcr4
Fah
Ighg3
Rgs19
Irf2
Ube2w
Psip1
Metabolic process
Ccl5
Gzma
Bst2
Grn
Ctsl
Ccnd1
Litaf
Lag3
Rps6ka1
Ccnd2
Cst7
Car2
Xcl1
Cited4
Khk
Ramp1
Fasl
Htra3
Epcam
Timp2
Gsn
Ifnar2
Edem2
Dnajc15
Shb
Cdh1
Spry2
Dnajb1
Scimp
M
Intestinal B cells / OT-1 T cells co-culture
CD8+CD25+ cells
CD8+CD69+ cells
CD8+PD1+ cells
CD8+CXCR6+ cells
CD8+CTLA4+ cells
% of CD8 T cells
WT ND B + T cells
WT CD-HFD B + T cells

Fig. S3

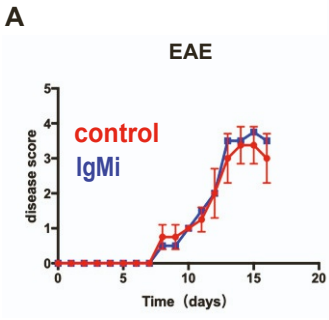

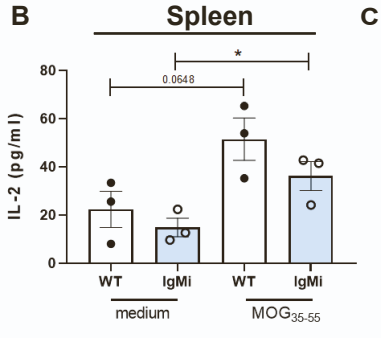

C

Group	Statistics	Serum ALT (U/L)	Serum Cholesterol (mg/dL)	Hepatic triglycerides (µg/mg tissue)	NAS	Outcome
WT ND 6M	Mean value	39.13	110.8	33.12	0.4	healthy liver, normal body weight
	SEM	±4.357	±9.027	± 4.784	± 0.245	
	N	5	5	5	5	
WT CD-HFD 6M	Mean value	200.9	284.3	211.6	5.8	NASH, obesity
	SEM	±21.231	±18.845	± 40.23	± 0.2	
	N	5	5	5	5	
	P-value[a]	<0.0001	<0.0001	0.0023	< 0.0001	
IgMi CD-HFD 6M	Mean value	54.28	157.1	59.9	1.636	healthy liver, ↓steatosis, obesity
	SEM	±6.798	±9.684	± 7.91	± 0.338	
	N	10	10	6	11	
	P-value[b]	<0.0001	<0.0001	0.0028	< 0.0001	
	P-value[c]	0.1625	0.0095	0.0226	0.0364	

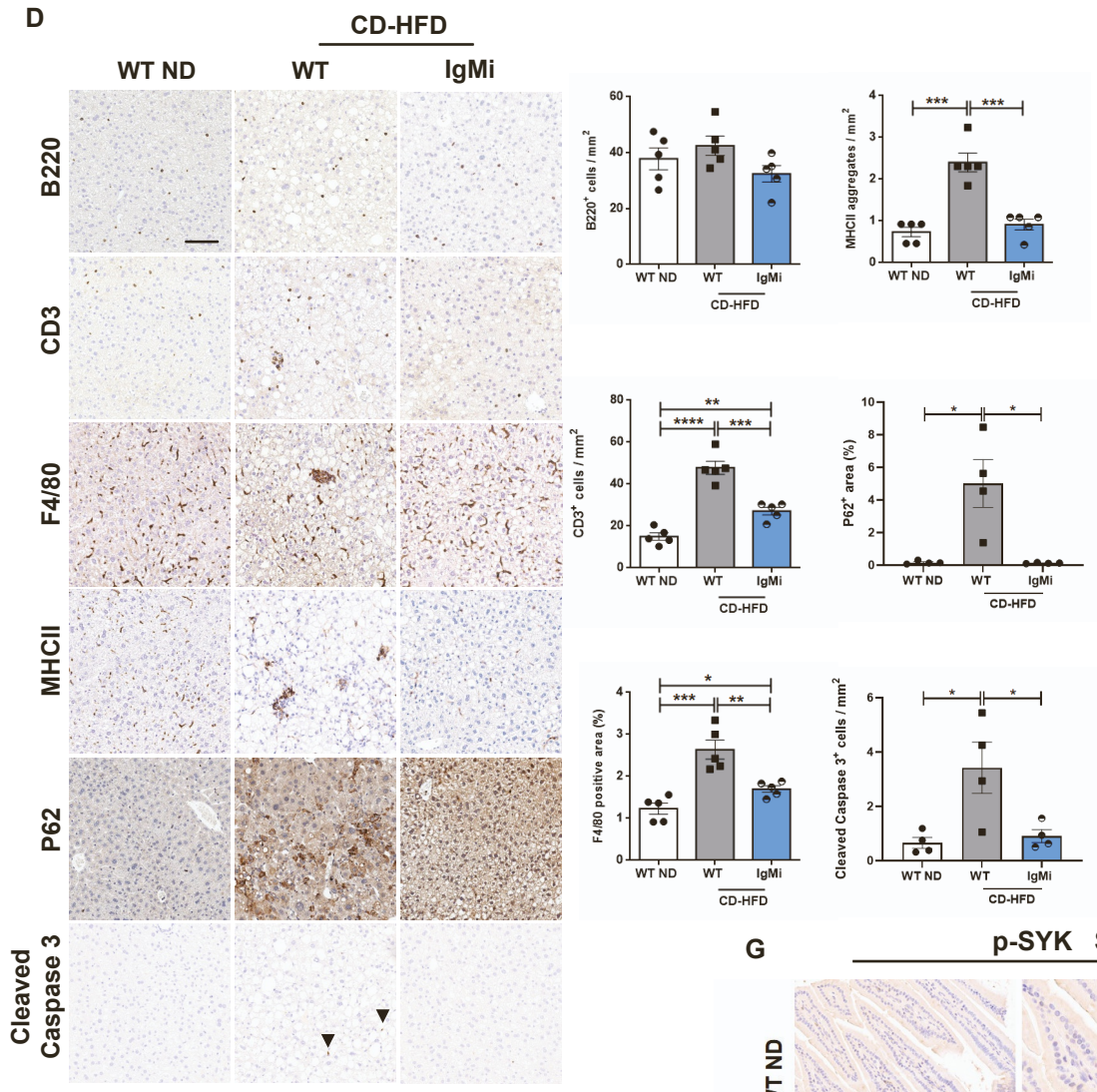

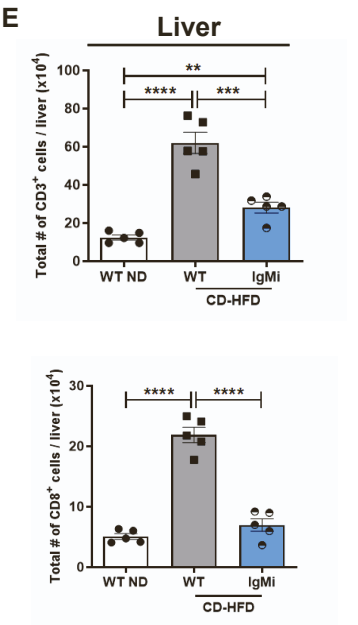

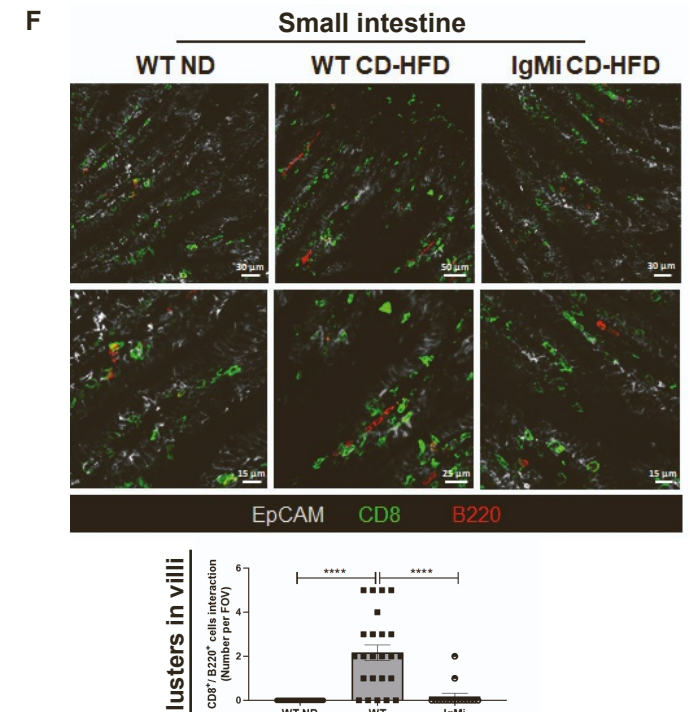

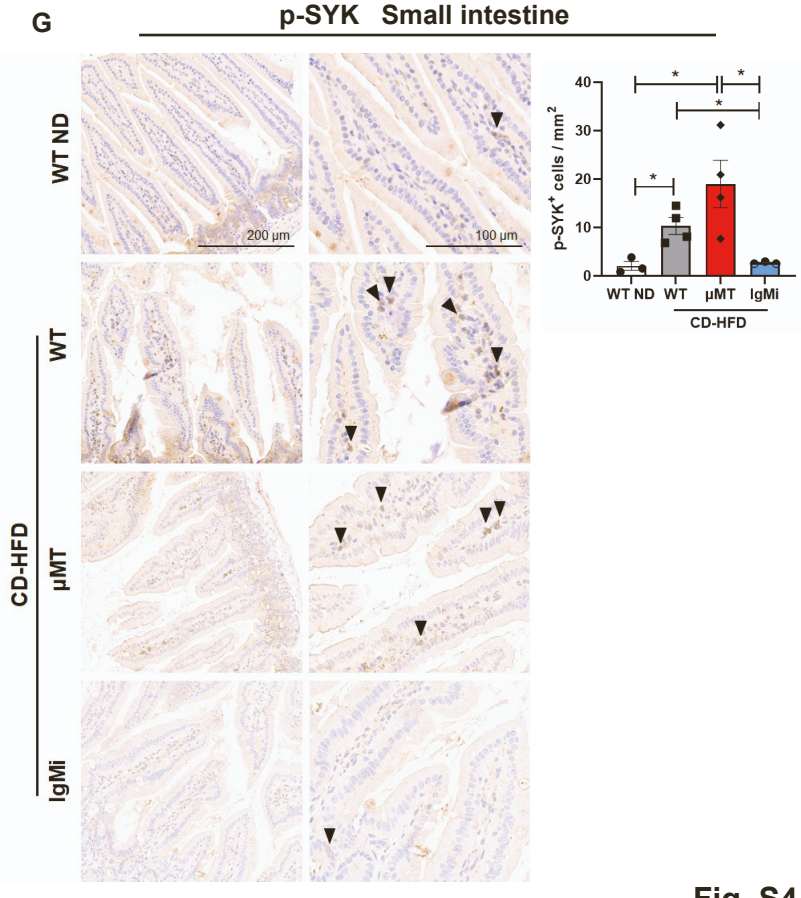

Fig. S4

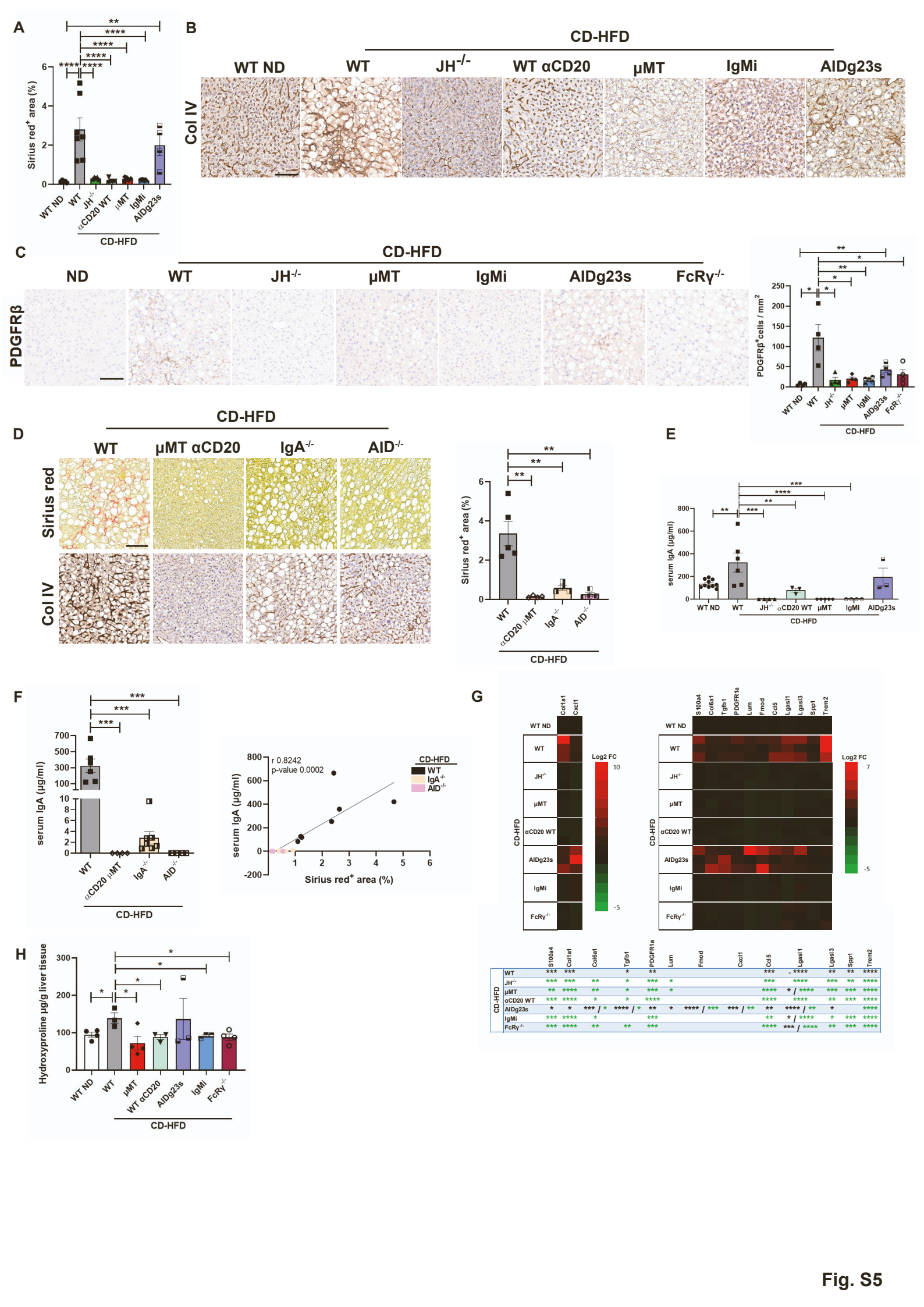
A
Sirius red+ area (%)
WT ND
WT
JH-/-
αCD20 WT
μMT
IgMi
AIDg23s
CD-HFD
B
CD-HFD
WT ND
WT
JH-/-
WT αCD20
μMT
IgMi
AIDg23s
Col IV
C
CD-HFD
ND
WT
JH-/-
μMT
IgMi
AIDg23s
FcRγ-/-
PDGFRβ
PDGFRβ+cells / mm2
D
CD-HFD
WT
μMT αCD20
IgA-/-
AID-/-
Sirius red
Col IV
Sirius red+ area (%)
E
serum IgA (μg/ml)
F
serum IgA (μg/ml)
r 0.8242
p-value 0.0002
CD-HFD
WT
IgA-/-
AID-/-
Sirius red+ area (%)
G
Log2 FC
S100a4
Col1a1
Col6a1
Tgfb1
PDGFR1a
Lum
Fmod
Cxcl1
Ccl5
Lgals1
Lgals3
Spp1
Trem2
H
Hydroxyproline μg/g liver tissue

Fig. S5

I

Group	Statistics	Serum ALT (U/L)	Serum Cholesterol (mg/dL)	Hepatic triglycerides (µg/mg tissue)	NAS	Outcome
WT CD-HFD 6M	Mean value	243.8	273.2	121.5	5.25	NASH, obesity
	SEM	± 46.71	± 12.74	± 9.607	± 0.479	
	N	5	5	5	4	
FcRγ$^{-/-}$ CD-HFD 6M	Mean value	296.9	251.3	5.25	4.25	NASH, obesity
	SEM	± 64.39	± 16.81	± 0.479	± 0.25	
	N	5	5	4	4	
	P-value[a]	0.5236	0.3285	0.8038	0.1135	

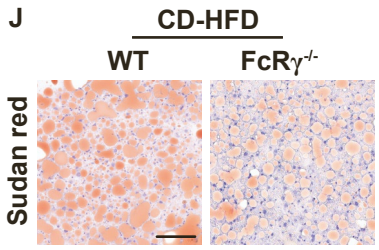

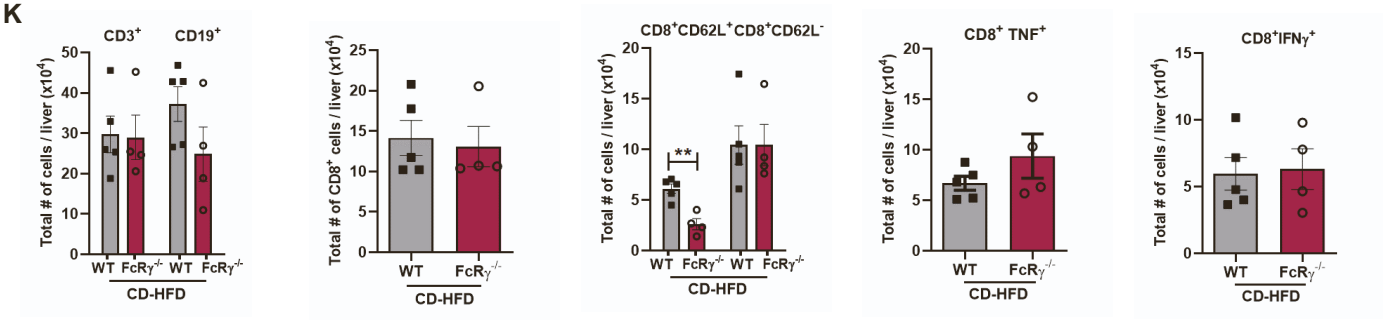

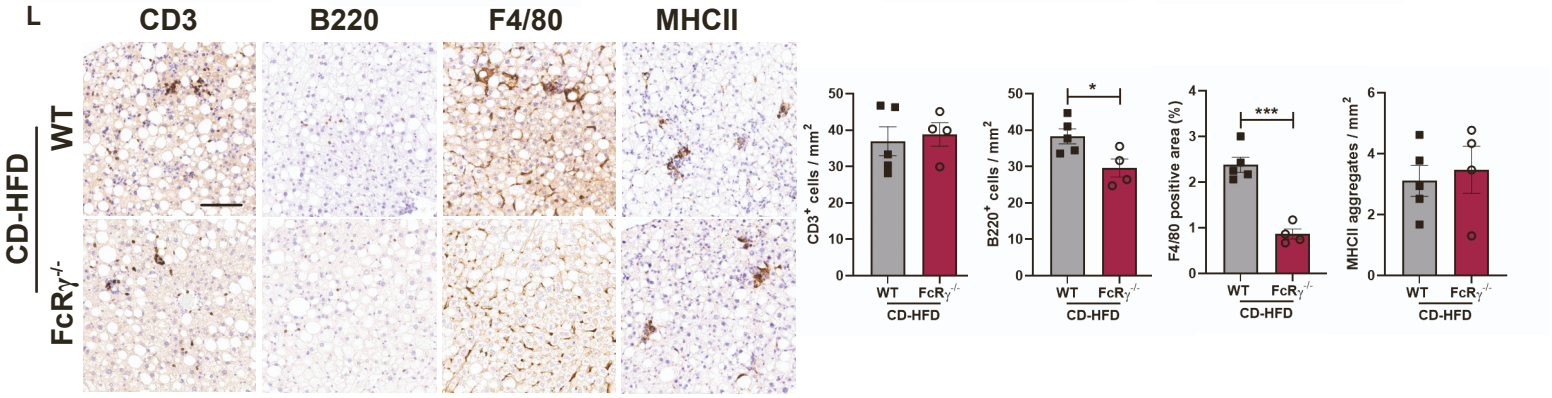

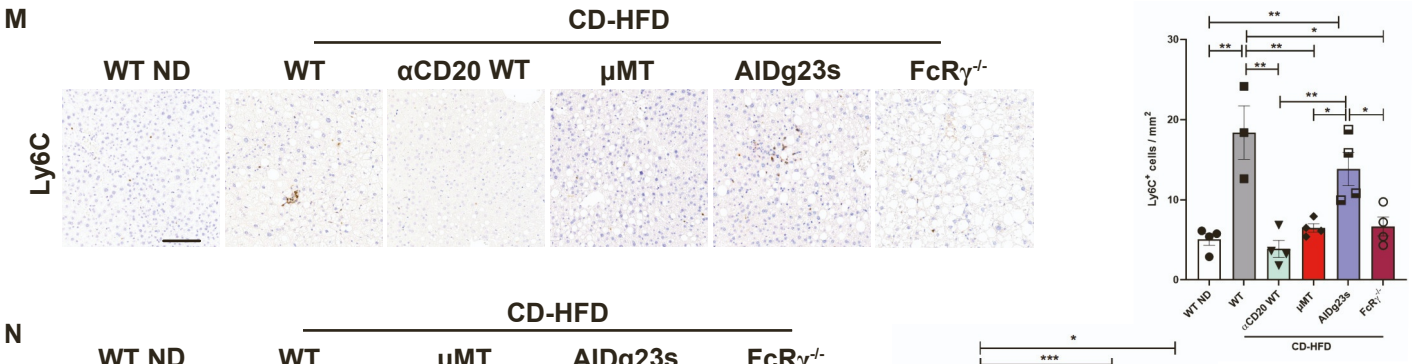

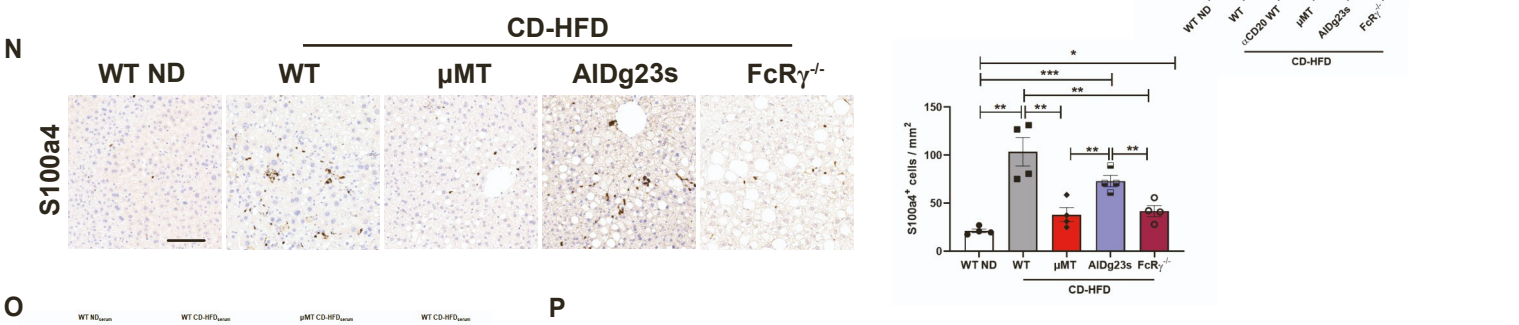

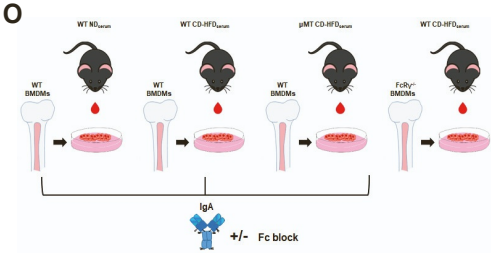

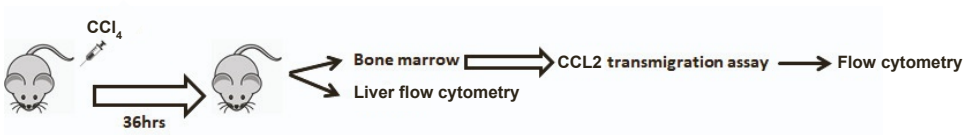

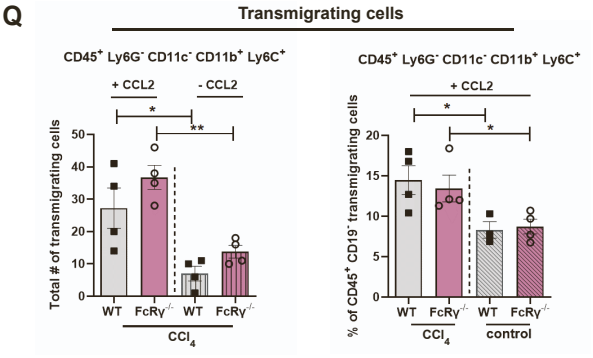

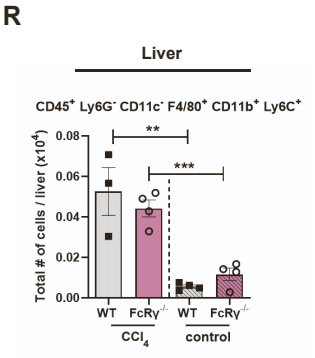

Fig. S5

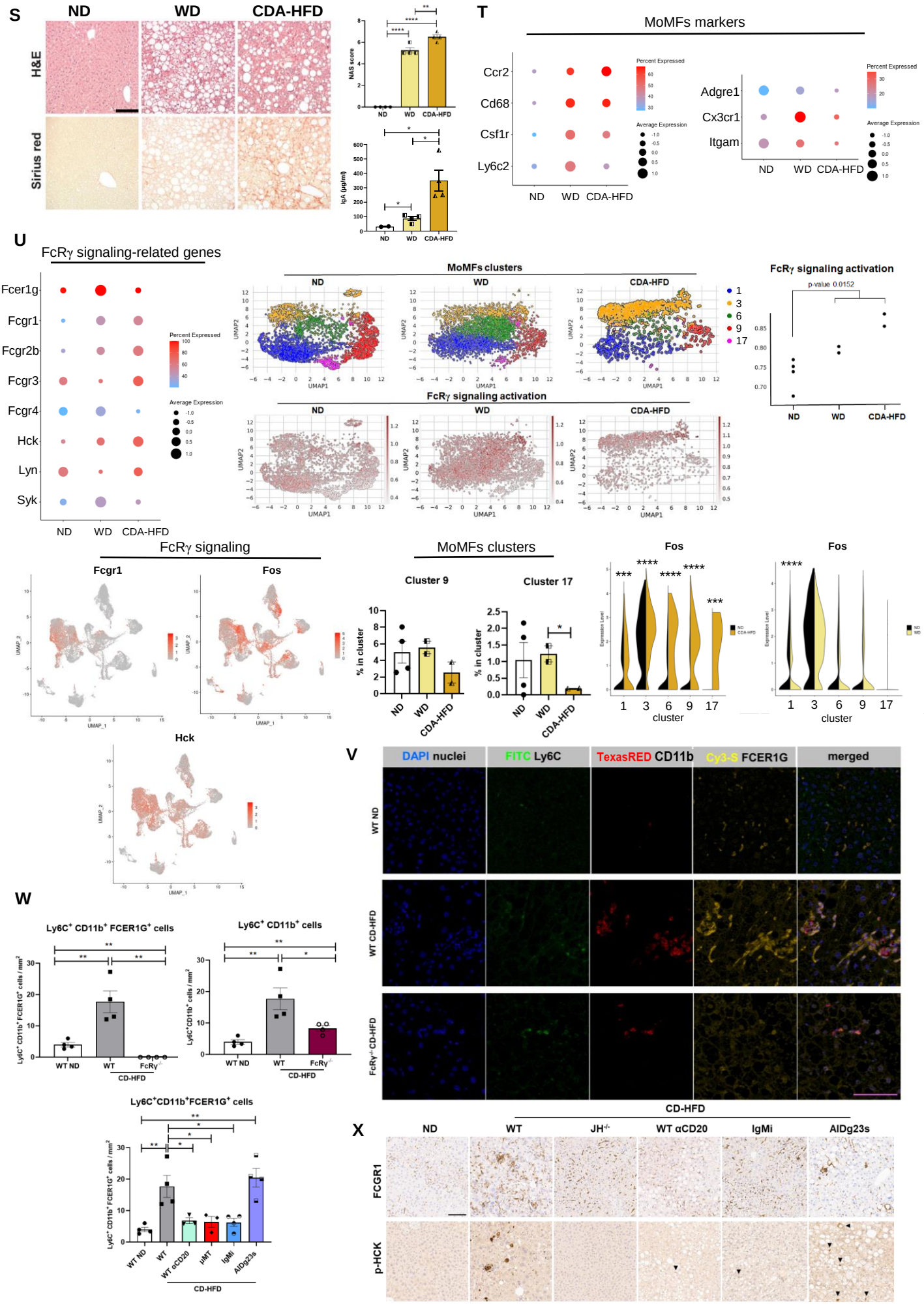
S
ND
WD
CDA-HFD
H&E
Sirius red
NAS score
IgA (μg/ml)
T
MoMFs markers
Ccr2
Cd68
Csf1r
Ly6c2
Adgre1
Cx3cr1
Itgam
Percent Expressed
Average Expression
U
FcRγ signaling-related genes
Fcer1g
Fcgr1
Fcgr2b
Fcgr3
Fcgr4
Hck
Lyn
Syk
MoMFs clusters
FcRγ signaling activation
p-value 0.0152
FcRγ signaling
Fcgr1
Fos
Hck
Cluster 9
Cluster 17
% in cluster
cluster
V
DAPI nuclei
FITC Ly6C
TexasRED CD11b
Cy3-S FCER1G
merged
WT ND
WT CD-HFD
FcRγ-/- CD-HFD
W
Ly6C+ CD11b+ FCER1G+ cells
Ly6C+ CD11b+ cells
Ly6C+ CD11b+ FCER1G+ cells / mm2
WT ND
WT
FcRγ-/-
CD-HFD
WT αCD20
μMT
IgMi
AIDg23s
X
CD-HFD
ND
WT
JH-/-
WT αCD20
IgMi
AIDg23s
FCGR1
p-HCK

Fig. S5

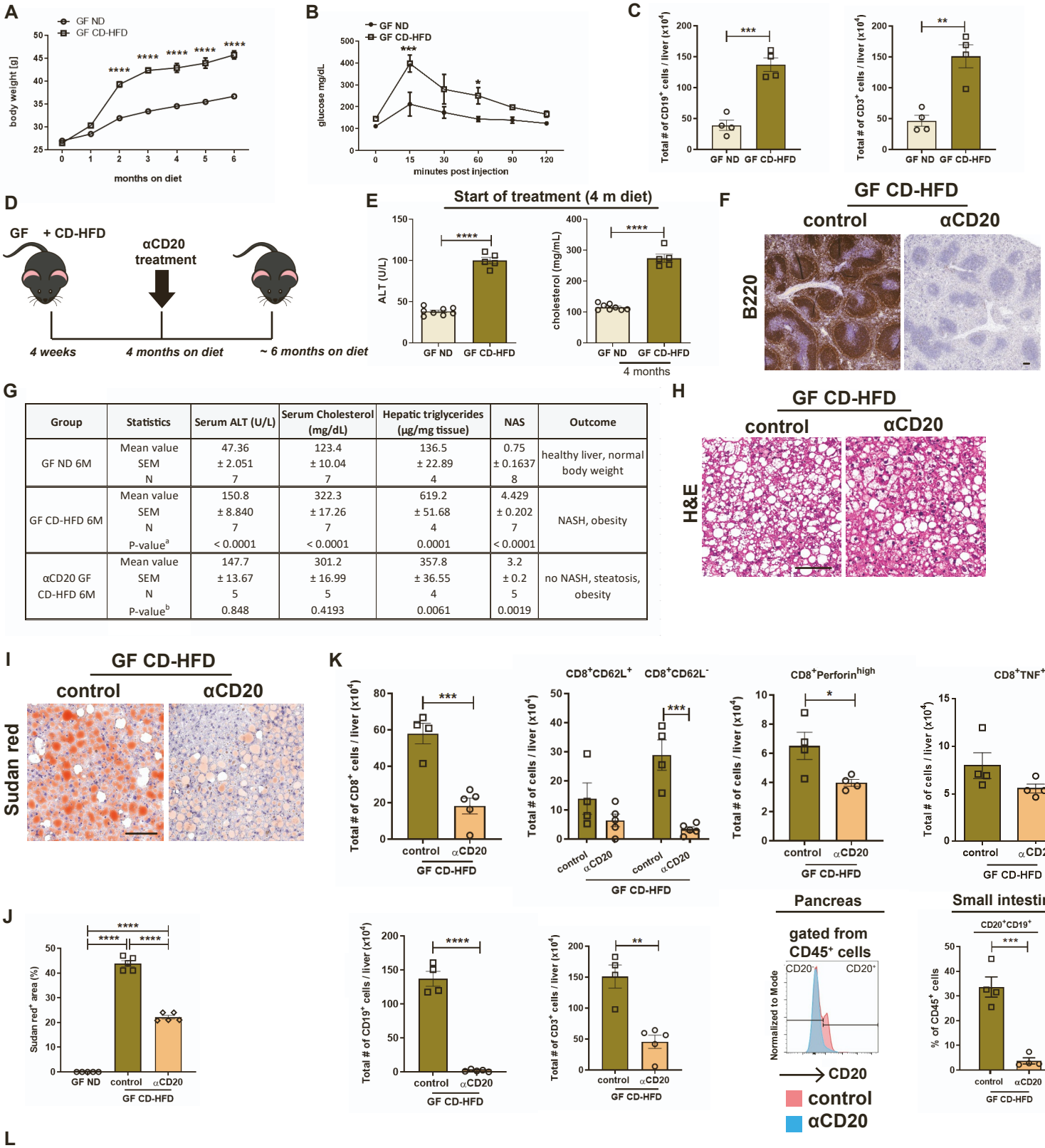

Group	Statistics	Serum ALT (U/L)	Serum Cholesterol (mg/dL)	Hepatic triglycerides (µg/mg tissue)	NAS	Outcome
GF ND 6M	Mean value	47.36	123.4	136.5	0.75	healthy liver, normal body weight
	SEM	± 2.051	± 10.04	± 22.89	± 0.1637	
	N	7	7	4	8	
GF CD-HFD 6M	Mean value	150.8	322.3	619.2	4.429	NASH, obesity
	SEM	± 8.840	± 17.26	± 51.68	± 0.202	
	N	7	7	4	7	
	P-value[a]	< 0.0001	< 0.0001	0.0001	< 0.0001	
αCD20 GF CD-HFD 6M	Mean value	147.7	301.2	357.8	3.2	no NASH, steatosis, obesity
	SEM	± 13.67	± 16.99	± 36.55	± 0.2	
	N	5	5	4	5	
	P-value[b]	0.848	0.4193	0.0061	0.0019	

Fig. S6

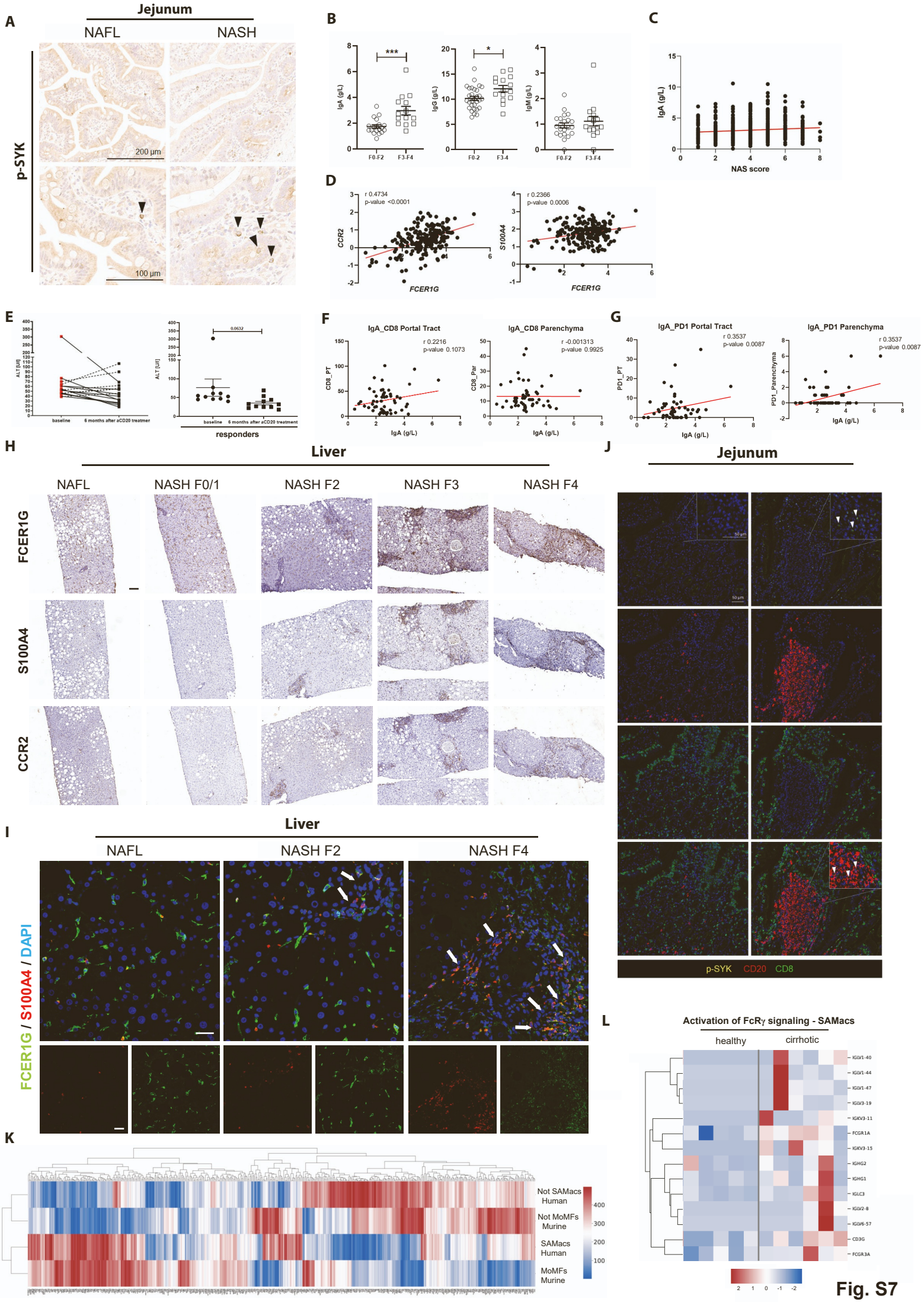
A
Jejunum
NAFL
NASH
p-SYK
200 µm
100 µm
B
IgA (g/L)
IgG (g/L)
IgM (g/L)
***
*
F0-F2
F3-F4
C
IgA (g/L)
NAS score
D
r 0.4734
p-value <0.0001
CCR2
FCER1G
r 0.2366
p-value 0.0006
S100A4
FCER1G
E
ALT [UI]
baseline
6 months after aCD20 treatmer
0.0632
6 months after aCD20 treatment
responders
F
IgA_CD8 Portal Tract
r 0.2216
p-value 0.1073
CD8_PT
IgA (g/L)
IgA_CD8 Parenchyma
r -0.001313
p-value 0.9925
CD8_Par
IgA (g/L)
G
IgA_PD1 Portal Tract
r 0.3537
p-value 0.0087
PD1_PT
IgA (g/L)
IgA_PD1 Parenchyma
r 0.3537
p-value 0.0087
PD1_Parenchyma
IgA (g/L)
H
Liver
NAFL
NASH F0/1
NASH F2
NASH F3
NASH F4
FCER1G
S100A4
CCR2
J
Jejunum
p-SYK CD20 CD8
I
Liver
NAFL
NASH F2
NASH F4
FCER1G / S100A4 / DAPI
K
Not SAMacs Human
Not MoMFs Murine
SAMacs Human
MoMFs Murine
L
Activation of FcRγ signaling - SAMacs
healthy
cirrhotic
IGLV1-40
IGLV1-44
IGLV1-47
IGLV3-19
IGKV3-11
FCGR1A
IGKV3-15
IGHG2
IGHG1
IGLC3
IGLV2-8
IGLV6-57
CD3G
FCGR3A

Fig. S7